AERODYNAMIC, INFRARED EXTINCTION, AND TRIBOCHARING PROPERTIES OF NANOSTRUCTURED AND CONVENTIONAL PARTICLES

by

SUSANA CASTRO PJESKY

B.Sc., University of the Philippines at Los Baños, 1996
M.Sc., University of the Philippines at Los Baños, 2002

AN ABSTRACT OF A DISSERTATION

submitted in partial fulfillment of the requirements for the degree

DOCTOR OF PHILOSOPHY

Department of Biological and Agricultural Engineering
College of Engineering

KANSAS STATE UNIVERSITY
Manhattan, Kansas

2008

Abstract

Nanostructured particles possess unique chemical and physical properties, making them excellent candidates for air purification, smoke clearing, and obscuration. This research was conducted to investigate the aerodynamic, charging, and infrared (IR) extinction properties of nanostructured particles. Specific objectives were to: (1) measure the size distribution and concentration of aerosolized nanostructured particles; (2) evaluate their IR extinction properties; (3) determine their relative chargeability; and (4) numerically model their transport in enclosed rooms.

The size distribution and concentration of two nanostructured particles (NanoActive® MgO and MgO plus) were measured in an enclosed room. The particles differed in size distribution and concentration; for example, the geometric mean diameters of NanoActive® MgO and MgO plus were 3.12 and 11.1 μm, respectively.

The potential of nanostructured particles as IR obscurants was determined and compared with other particles. Four groups of particles were considered: nanostructured particles (NanoActive® MgO plus, MgO, TiO_2); nanorods (MgO, TiO_2); conventional particles ($NaHCO_3$ and ISO fine test dust); and common obscurants (brass, graphite, carbon black). The extinction coefficients of the nanostructured particles were generally significantly smaller than those of the other particles. Graphite flakes had the greatest mass extinction coefficient (3.22 m^2/g), followed by carbon black (1.72 m^2/g), and brass flakes (1.57 m^2/g). Brass flakes had the greatest volume extinction coefficient (1.64 m^2/cc), followed by $NaHCO_3$ (0.93 m^2/cc), and ISO fine test dust (0.91 m^2/cc).

The relative chargeability of nanostructured particles was also investigated. Selected particles were passed through a Teflon tribocharger and their net charge-to-mass ratios were

measured. Tribocharging was able to charge the particles; however, the resulting charge was generally small. NanoActive® TiO_2 gained the highest net charge-to-mass ratio (1.21 mC/kg) followed by NanoActive® MgO (0.81 mC/kg) and ISO fine test dust (0.66 mC/kg).

The transport of NanoActive® MgO plus and hollow glass spheres in an enclosed room was simulated by implementing the discrete phase model of FLUENT. In terms of mass concentrations, there was reasonable agreement between predicted and measured values for hollow glass spheres but not for NanoActive® MgO plus. In terms of number concentration, there was large discrepancy between predicted and measured values for both particles.

AERODYNAMIC, INFRARED EXTINCTION AND TRIBOCHARING PROPERTIES OF NANOSTRUCTURED AND CONVENTIONAL PARTICLES

by

SUSANA CASTRO PJESKY

B.Sc., University of the Philippines at Los Baños, 1996
M.Sc., University of the Philippines at Los Baños, 2002

A DISSERTATION

submitted in partial fulfillment of the requirements for the degree

DOCTOR OF PHILOSOPHY

Department of Biological and Agricultural Engineering
College of Engineering

KANSAS STATE UNIVERSITY
Manhattan, Kansas

2008

Approved by:

Major Professor
Ronaldo G. Maghirang

Copyright

Abstract

Nanostructured particles possess unique chemical and physical properties, making them excellent candidates for air purification, smoke clearing, and obscuration. This research was conducted to investigate the aerodynamic, charging, and infrared (IR) extinction properties of nanostructured particles. Specific objectives were to: (1) measure the size distribution and concentration of aerosolized nanostructured particles; (2) evaluate their IR extinction properties; (3) determine their relative chargeability; and (4) numerically model their transport in enclosed rooms.

The size distribution and concentration of two nanostructured particles (NanoActive® MgO and MgO plus) were measured in an enclosed room. The particles differed in size distribution and concentration; for example, the geometric mean diameters of NanoActive® MgO and MgO plus were 3.12 and 11.1 μm, respectively.

The potential of nanostructured particles as IR obscurants was determined and compared with other particles. Four groups of particles were considered: nanostructured particles (NanoActive® MgO plus, MgO, TiO_2); nanorods (MgO, TiO_2); conventional particles ($NaHCO_3$ and ISO fine test dust); and common obscurants (brass, graphite, carbon black). The extinction coefficients of the nanostructured particles were generally significantly smaller than those of the other particles. Graphite flakes had the greatest mass extinction coefficient (3.22 m^2/g), followed by carbon black (1.72 m^2/g), and brass flakes (1.57 m^2/g). Brass flakes had the greatest volume extinction coefficient (1.64 m^2/cc), followed by $NaHCO_3$ (0.93 m^2/cc), and ISO fine test dust (0.91 m^2/cc).

The relative chargeability of nanostructured particles was also investigated. Selected particles were passed through a Teflon tribocharger and their net charge-to-mass ratios were

measured. Tribocharging was able to charge the particles; however, the resulting charge was generally small. NanoActive® TiO_2 gained the highest net charge-to-mass ratio (1.21 mC/kg) followed by NanoActive® MgO (0.81 mC/kg) and ISO fine test dust (0.66 mC/kg).

The transport of NanoActive® MgO plus and hollow glass spheres in an enclosed room was simulated by implementing the discrete phase model of FLUENT. In terms of mass concentrations, there was reasonable agreement between predicted and measured values for hollow glass spheres but not for NanoActive® MgO plus. In terms of number concentration, there was large discrepancy between predicted and measured values for both particles.

Table of Contents

List of Figures xiii
List of Tables xvii
List of Symbols xx
List of Symbols xx
Acknowledgements xxiii
1. INTRODUCTION 1
1.1 Background 1
1.2 Research Objectives 2
1.3 Organization of the Dissertation 3
1.4 References 4
2. LITERATURE REVIEW 6
2.1 Particle Characterization 6
2.1.1 Particle size distribution 6
2.1.2 Particle shape and size 7
2.1.3 Particle concentration 9
2.1.4 Measurement methods 10
2.1.5 Summary 13
2.2 Infrared Extinction Properties 13
2.2.1 Infrared (IR) obscurant and extinction coefficient 13
2.2.2 Common IR particulate obscurants 15
2.2.3 Calculation of extinction coefficients 15
2.2.4 Measurement of extinction coefficients 16
2.2.5 Summary 17
2.3 Electrostatic Charging 18
2.3.1 Charge measurement 18
2.3.2 Tribocharging of particles 19
2.3.2.1 Tribocharging in powder coating 20
2.3.2.2 Factors affecting tribocharging 21

2.3.2.2.1 Work function and contact potential difference 22
2.3.2.2.2 Surface contact 24
2.3.2.2.3 Surface chemistry 24
2.3.2.2.4 Electrical properties of particles 25
2.3.2.2.5 Charge backflow and gaseous discharge 25
2.3.2.2.6 Environmental factors 26
2.3.2.3 Gaussian limit 26
2.3.3 Charging of Nanoparticles 27
2.3.4 Summary 27
2.4 Numerical Simulation of Particle Transport 28
2.4.1 Two-phase flows 28
2.4.2 Computational fluid dynamics (CFD) 30
2.4.3 Approaches in modeling two-phase flows 30
2.4.3.1 Eulerian-Eulerian approach 30
2.4.3.2 Eulerian-Lagrangian approach 32
2.4.4 Turbulence Model 34
2.4.6 Summary 36
2.5 References 36
3. Size Distribution and Concentration of Aerosolized Nanostructured Particles 47
3.1 Abstract 47
3.2 Introduction 48
3.3 Materials and Methods 50
3.3.1 Experimental set-up and instrumentation 50
3.3.2 Experimental procedure 53
3.3.3 Data analysis 55
3.3.3.1 Conversion from number concentration to mass concentration 55
3.3.3.2 Conversion of mobility diameter to aerodynamic diameter 56
3.3.3.3 Merging of SMPS and APS data 56
3.3.3.4 Particulate matter 57
3.3.3.5 Statistical Analysis 57
3.4 Results and Discussion 57

3.4.1 Particle Deployment 57
3.4.2 Particle size distribution (PSD) 58
3.4.3 Geometric mean diameter (GMD) 60
3.4.4 Decay in number and mass concentrations 61
3.5 Conclusion 63
3.6 References 77
4. Infrared Extinction Properties of Nanostructured and Conventional Particles 81
4.1 Abstract 81
4.2 Introduction 82
4.3 Materials and Methods 84
4.3.1 Experimental apparatus 84
4.3.2 Particulate obscurants 86
4.3.3 Experimental procedure 87
4.3.3.1 Measurement of extinction coefficients and particle size distribution 87
4.3.3.2 Measurement of the tap density 91
4.3.3.3 Data analysis 92
4.4 Results and Discussion 93
4.4.1 Mass extinction coefficients 93
4.4.2 Volume extinction coefficients 95
4.4.3 Effect of particle size distribution and concentration 99
4.5 Conclusions 104
4.6 References 105
5. Relative Chargeability of Nanostructured and Conventional Particles by Tribocharging . 109
5.1 Abstract 109
5.2 Introduction 109
5.3 Materials and Methods 112
5.3.1 Test particles 112
5.3.2 Tribocharger 113
5.3.3 Charge measurement 113
5.3.4 Experimental procedure 115
5.3.5 Data analysis 115

5.4 Results and Discussion 119
5.5 Conclusions 121
5.6 References 124
6. Numerical Simulation of Particle Transport in an Enclosed Room 127
6.1 Abstract 127
6.2 Introduction 127
6.3 Materials and Methods 129
6.3.1 Theoretical background 129
6.3.1.1 Governing equations for the continuous phase 129
6.3.1.2 Governing equations for the discrete phase 131
6.3.2 Case description 132
6.3.3 Test particles 132
6.3.4 Geometry and mesh generation 134
6.3.5 Implementation of the CFD model 135
6.3.4.1 Calculation of number of particles dispersed in the chamber 138
6.3.4.2 Calculation of number of particles in a parcel 139
6.3.4.3 Post-processing of the simulation results 141
6.3.5 Experimental validation 142
6.3.5.1 Data analysis 144
6.4 Results and Discussion 145
6.4.1 Predicted gas velocities 145
6.4.2 Predicted particle trajectories 145
6.4.3 Comparison of predicted results with experimental data 146
6.4.3.1 Hollow glass spheres 146
6.4.3.2 NanoActive® MgO plus 151
6.5 Conclusions 153
6.6 References 153
7. Conclusions and Recommendations 156
7.1 Conclusions 156
7.2 Suggestions for Further Research 157
Appendix A - Photos of instruments and experimental set-ups 158

Appendix B - Calibration of the dynamic Faraday cup sampler 164
Appendix C - Summary of raw data 166

List of Figures

Figure 2.1 An example of a triboelectric series with its corresponding relative work functions (Tianxiang, 1999; Liberto, 1994). 21

Figure 3.1. Schematic diagram of the experimental chamber showing the instruments: Aerodynamic Particle Sizer® (APS) Spectrometer, Scanning Mobility Particle Sizer ® (SMPS) spectrometer, Tapered Element Oscillating Microbalance® (TEOM), and filter samplers 52

Figure 3.2 Scanning electron micrographs: (a) NA MgO plus and (b) NA MgO particles 54

Figure 3.3. Comparison of the two particles in deployed amount (g) and percent deployed. Bars with the same letters are not significantly different at the 5% level. Error bars represent mean of three replicates 59

Figure 3.4. Effect of dispersion pressure (80 vs. 40 psig) on the deployed amount (g) and percent deployed of NA MgO plus. Bars with the same letters are not significantly different at the 5% level. Error bars represent mean of three replicates. 59

Figure 3.5. Effect of nominal amount (50 vs. 20 g) on the percent deployed of NA MgO plus. Bars with the same letters are not significantly different at the 5% level. Error bars represent mean of three replicates 60

Figure 3.6. Particle size distributions of NA MgO (11 g, 80 psig) at 2 min after deployment - SMPS, APS, and merged SMPS-APS data. The goodness of fit of merged data is 0.030. Each curve represents the mean of three replicates. 64

Figure 3.7. Particle size distributions of NA MgO plus (13 g, 80 psig) at 2 min after deployment - SMPS, APS, and merged SMPS-APS data. The goodness of fit of merged data is 0.038. Each curve represents the mean of three replicates. 65

Figure 3.8. Merged SMPS and APS particle size distributions for NA MgO plus and NA MgO at 2 min after deployment. Each curve represents the mean of the three replicates. 66

Figure 3.9. Merged SMPS and APS particle size distributions of NA MgO plus as affected by nominal amount and canister pressure at 2 min after deployment. Each curve represents the mean of the three replicates. The goodness of fit values for the merged data are 0.048, 0.045 and 0.038 for deployed mass and dispersion pressure combinations of 40 g and 80 psig, 30 g and 40 psig, and 13 g and 80 psig, respectively. 67

Figure 3.10. Temporal change in particle size distributions of NA MgO plus measured with APS: number-based (a) and mass-based (b). Each curve represents the mean of three replicates. 68

Figure 3.11. Temporal change in particle size distributions of NA MgO plus measured with SMPS: number-based (a) and mass-based (b). Each curve represents the mean of three replicates. 69

Figure 3.12. Temporal change in particle size distributions of NA MgO measured with APS: number-based (a) and mass-based (b). Each curve represents the mean of the three replicates. 70

Figure 3.13. Temporal change in particle size distributions of NA MgO measured with SMPS: number-based (a) and mass-based (b). Each curve represents the mean of the three replicates 71

Figure 3.14. Temporal change in geometric mean diameters (GMD) of NA MgO and NA MgO plus as measured by SMPS (a) and APS (b). Each curve represents the mean of three replicates. Error bars represent one standard deviation. 73

Figure 3.15. Number concentrations of NA MgO plus and NA MgO, as measured by the SMPS (a) and APS (b). Each curve represents the mean of three replicates. Error bars represent one standard deviation..... 74

Figure 3.16. Mass concentrations of NA MgO plus and NA MgO, as measured by the SMPS (a) and APS (b). Each curve represents the mean of the three replicates. Error bars represent one standard deviation..... 75

Figure 3.17. Temporal change in the PM_4 concentration of the two nanostructured particles 76

Figure 3.18. Mass concentrations of NA MgO plus and NA MgO as measured by the TEOM. Each curve represents the mean of three replicates. Error bars represent one standard deviation..... 76

Figure 3.19. Comparison of the mass concentrations measured by TEOM and filter samplers at 1 min after dispersion. Each curve represents the mean of three replicates. Bars with the same letters are not significantly different at the 5% level. 77

Figure 4.1. Schematic diagram of the experimental chamber showing the instruments (not drawn to scale). 86

Figure 4.2. Scanning electron microscope (SEM) images of the nanostructured metal oxide particles: (a) NanoActive® MgO plus and (b) NanoActive® MgO..... 88

Figure 4.3. SEM images of the conventional particles: (a) $NaHCO_3$ and (b) ISO fine test dust. 88

Figure 4.4. SEM images of the reference particles: (a) brass flakes, (b) graphite flakes, and (c) carbon black. 89

Figure 4.5. SEM images of the nanorods: (a) MgO nanorods and (b) TiO_2 nanorods. 89

Figure 4.6. Mass extinction coefficients of the particles. Each spectrum represents the mean of three replicates. 96

Figure 4.7. Comparison of the mass extinction coefficients of the NanooActive® particles and nanorods. Each nanorod spectrum represents the mean of two replicates..... 96

Figure 4.8. Volume extinction coefficients of the different particles. Each spectrum represents the mean of three replicates. 98

Figure 4.9. Comparison of the volume extinction coefficients of the NanoActive® particles and nanorods. Each nanorod spectrum represents the mean of two replicates. 98

Figure 4.10. Particle size distribution of the particles at time 1 minute after dispersion. Each curve represents the mean of three replicates, except for the curves of the nanorods which represent two replicates. 100

Figure 4.11. Number (a) and mass (b) concentrations of the particles. Each point in the curve represents the mean of three replicates, except for the nanorods which represent two replicates. 102

Figure 5.1 Photograph of the Teflon® charging tube. 114

Figure 5.2. Schematic diagram of the dynamic Faraday-cage sampler for measuring the net charge-to-mass ratio of airborne particles. 117

Figure 5.3. Photograph of the dynamic Faraday-cage sampler. The top cover of outer metal shield was removed to show the inner conducting metal enclosure. 117

Figure 5.4. Schematic diagram of the experimental set-up (not drawn to scale). 118

Figure 5.5. Schematic diagram of the powder disperser system and the tribocharger. 119

Figure 5.6. Background charges of the particles, that is, the Teflon® tribocharger was not in use. 122

Figure 5.7. Charges of the particles after passing through a Teflon® tribocharger. 123

Figure 6.1. Schematic diagram of the experimental chamber used in the simulation. 133

Figure 6.2. Scanning electron micrographs of the particles: (a) hollow glass spheres and (b) NanoActive® MgO plus. 134

Figure 6.3. The experimental set-up with three filter samplers. 143

Figure 6.4. The experimental set-up with the Aerodynamic Particle Sizer® (APS) spectrometer. 143

Figure 6.5. Contour plots of the velocities of the gas at various times: (a) 1 s , (b) 2 s, (c) 3 s, and (d) 4 s using fine mesh. Number scale on the left represents the velocity magnitude in m/s. Inserts are the more detailed picture of the injection. 147

Figure 6.6. Pathlines of the velocity of the gas inside the chamber at various times: (a) 10 s, (b) 60 s, (c),300 s, and (c) 600 s using fine mesh. The plots are in the x-y plane and at the center of the injection port (z = 1.1 cutting plane). Number scale on the left represents the velocity magnitude in m/sec. 148

Figure 6.7. Particle trajectories of hollow glass spheres at various times: (a) 3 s, (b) 60 s, (c) 300 s, and (d) 600 s using fine mesh and 100 parcels. The dots in the plots represent the parcels that contain a large number of particles with the same properties. Number scale on the left represents the particle residence time in s. 149

Figure A.1. The Aerodynamic Particle Sizer® (APS) spectrometer (Model 3321, TSI Inc., Shoreview, MN) with a dilution unit (Model 3302A, TSI, Inc., Shoreview, MN), for measuring the equivalent aerodynamic diameter of particles from 0.5 µm to 20 µm. 159

Figure A.2. The Scanning Mobility Particle Sizer® (SMPS) spectrometer (Model 3936, TSI Inc., Shoreview, MN) for measuring the equivalent mobility diameter of particles from ~ 10 nm to 1000 nm. 159

Figure A.3. The Tapered Element Oscillating Microbalance (TEOM®) (Model 1400a, Thermo-Fisher Scientific, Inc., Waltham, MA), for measuring the mass concentration of particles. 160

Figure A.4. Experimental set-up for measuring the extinction coefficient of particles. 161

Figure A.5 . The powder disperser used to disperse particles in the chamber. 161

Figure A.6. A faraday-cage device for determining the charge of deployed particles. The device consists of two concentric metal cylinders. The inner cylinder, which is insulated from the outer cylinder, is electrically connected to the electrometer input. The outer cylinder is connected to ground and serves to shield the inner cylinder from external fields. The device is placed directly in front of the particle deployment location, allowing deployed particles to pass through the inner cylinder. 162

Figure A.7. The Keithley 6514 Electrometer for measuring electrostatic charge. 163

Figure A.8. Schematic diagram of the circuit for calibrating the Faraday cup sampler. 165

List of Tables

Table 3.1. Properties of the two nanostructured particles. 54

Table 3.2. Summary of experimental design. There were three replicates for each experiment. 55

Table 3.3. The geometric mean diameters (GMD) of the two nanostructured particles at 2 min after dispersion. 72

Table 3.4. The geometric standard deviations (GSD) of the two nanostructured particles at 2 min after dispersion. 72

Table 4.1. Physical and chemical properties of the particles. 90

Table 4.2. Band-averaged mass extinction coefficients, mass dispersed, and mass concentrations of particles. Each value represents the mean of three replicates. 97

Table 4.3. Band-averaged volume extinction coefficients and tap densities of particles. Each value represents the mean of three replicates. 97

Table 5.1. Properties of particles. 113

Table 5.2. Charge-to-mass ratios of the particles. 124

Table 6.1. Description of the three meshing schemes of the geometry of chamber and its inlet for hollow glass spheres. The coarse mesh scheme was used for NanoActive® MgO plus. 135

Table 6.2. Major assumptions used in the simulation of the continuous phase. 137

Table 6.3. Major assumptions used in the simulation of the discrete phase (hollow glass spheres). 138

Table 6.4. Simulation cases and experimental parameters for NanoActive® MgO plus. 138

Table 6.5. Number of particles dispersed inside the chamber calculated using different particle size and density. 139

Table 6.6. Calculated number of particles per parcel of hollow glass spheres using 100 parcels. 141

Table 6.7. Total mass flow rates of particles obtained from the experiments. Each value represents the mean of three replicates. 144

Table 6.8. Simulation and experimental parameters for hollow glass spheres. 144

Table 6.9. Predicted and measured mass concentrations, C_m, of the hollow glass spheres at t = 60 s after injection at three different sampling locations. 150

Table 6.10. Comparison of predicted and measured number concentrations, C_n, of hollow glass spheres at the center of the chamber. Predicted data started at 60 s for comparison to the first measured data which was obtained at 60 s. 150

Table 6.11. Comparison of the predicted and measured mass concentrations, C_m, of NanoActive® MgO plus (10 µm, 400 kg/m^3) at t=60 s. Each experimental data point represents the mean of three replicates. 152

Table 6.12. Comparison of predicted and measured number concentrations, C_n, of NanoActive® MgO plus at the center of the chamber. Predicted data started at 60 s for comparison to the first measured data which was obtained at 60 s. 152

Table B.1. Calibration data for the Faraday cup sampler. 165

Table C.1. Normalized particle number concentrations of NanoActive® MgO (11 g, 80 psig) measured with SMPS. 167

Table C.2. Normalized particle number concentrations of NanoActive® MgO (11 g, 80 psig) measured with APS. 169

Table C.3. Normalized particle number concentrations of NanoActive® MgO (11 g, 80 psig) - merged SMPS and APS data. 171

Table C.4. Normalized particle number concentrations of NanoActive® MgO plus (13 g, 80 psig) measured with SMPS. 173

Table C.5. Normalized particle number concentrations of NanoActive® MgO plus (13 g, 80 psig) measured with APS. 175

Table C.6. Normalized number concentrations of NanoActive® MgO plus (13 g, 80 psig) - merged SMPS and APS data. 177

Table C.7. Geometric mean diameters of NanoActive® MgO and NanoActive® MgO plus based on the SMPS and APS data. 179

Table C.8. Number concentrations of NanoActive® MgO plus and NanoActive® MgO measured with SMPS and APS. 180

Table C.9. Mass concentrations of NanoActive® MgO plus and NanoActive® MgO measured with SMPS and APS. 181

Table C.10. Mass concentrations of NanoActive® MgO plus and NanoActive® MgO measured with TEOM. 182

Table C.11. Mass extinction coefficients of the particles. 183

Table C.12. Masses dispersed and mass concentrations of particles measured using filter samplers. 184

Table C.13. Volume extinction coefficients of the particles. 185

Table C.14. Number and mass concentrations, geometric mean diameters (GMD), and geometric standard deviations (GSD) of the particles measured with APS at time 2 min after dispersion. 186

Table C.15. Charge-to-mass ratios of the particles. 187

Table C.16. Mass concentrations of hollow glass spheres (predicted and measured with filter samplers). 188

Table C.17. Mass concentrations of NanoActive® MgO plus (predicted and measured with filter samplers). 188
Table C.18. Number concentrations of hollow glass spheres (predicted and measured with APS® spectrometer)..... 188
Table C.19. Number concentrations of NanoActive® MgO plus (predicted and measured with APS® spectrometer). 189

List of Symbols

A	Absorbance (dimensionless)
C	Cunningham or slip correction factor (dimensionless)
C_a	Slip correction factor for aerodynamic diameter (dimensionless)
C_D	Drag coefficient (dimensionless)
C_m	Particle mass concentration (mg/m^3)
C_{me}	Slip correction factor for mobility diameter (dimensionless)
C_n	Particle number concentration ($\#/m^3$)
C_o	Observed or measured concentration (mg/m^3 or $\#/m^3$)
C_p	Predicted concentration (mg/m^3 or $\#/m^3$)
C_{12}	Capacitance between two metals (F)
$C_{1\varepsilon}$	Constant for k-ε turbulence model equal to 1.44
$C_{2\varepsilon}$	Constant for k-ε turbulence model equal to 1.92
C_μ	Constant for k-ε turbulence model equal to 0.09
D	Brownian diffusivity (m^2/s)
d/dt	Total time derivative
d_a	Equivalent aerodynamic diameter (μm)
d_p	Particle diameter (μm)
d_e	Equivalent spherical diameter (μm)
d_i	Midpoint size (μm)
d_{me}	Equivalent mobility diameter (μm)
E	Energy (J)
E_a	Breakdown strength of air (3 MV/m)
e	Electrostatic charge (C)
F_D	Drag force per unit particle mass (N/kg)
F_x	Additional acceleration (N/kg)
G_b	Generation of turbulence kinetic energy due to buoyancy
G_k	Generation of turbulence kinetic energy due to the mean velocity gradient
g_x	Gravitational acceleration (m/s^2)
k_{eff}	Effective thermal conductivity (W/m-K)

k	Turbulent kinetic energy (J)
L	Path length (m)
L*	Average interparticle distance (m)
M	Total mass of particles (kg)
m	Mass of a particle (kg)
N	Total number of particles
n	Number of observed or predicted values
n_i	Number of particles in group i
p	Thermodynamic pressure (Pa)
q/m	Charge-to-mass ratio (mC/kg)
Re	Reynolds number (dimensionless)
r	Particle radius (m)
S_c	Particle source term
S_k , S_e	User-defined source terms
T	Temperature (K)
T^*	Transmittance (dimensionless)
T	time (s)
u	Fluid phase velocity (m/s)
u_p	Particle velocity (m/s)
u'(t)	Fluctuating velocity component (m/s)
$\bar{u}$	Mean velocity (m/s)
$\bar{u}_i$	Average air velocity component in x, y, or z direction (m/s)
V	Relative velocity of particle with respect to fluid (m/s)
V_c	Contact potential difference (eV)
v_p	Particle turbulent diffusion coefficient (m^2/s)
x	Position of a particle (m)
Y_M	Contribution of fluctuating dilatation in compressible turbulence to the overall dissipation rate

Greek symbols

α_c	Continuous phase volume fraction (dimensionless)
α_p	Particulate volume fraction (dimensionless)
β	Particulate loading (dimensionless)
γ	Material density ratio (dimensionless)
ε	Turbulent dissipation rate (m^2/s^3)
ε_o	Permittivity of free space (8.85×10^{-12} F/m)
Γ	Effective particle diffusivity (m^2/s)
ζ	Gaussian random number
λ	Wavelength (μm)
λ_p	Mean free path (m)
μ	Viscosity (kg/s-m)
μ_t	Turbulent (or eddy) viscosity (kg/m-s)
σ_ε	Turbulent Prandtl number for ε (dimensionless)
σ_k	Turbulent Prandtl number for k (dimensionless)
σ_m	Mass extinction coefficient (m^2/g)
σ_v	Volume extinction coefficient (m^2/cc)
ρ, ρ_c	Fluid density (kg/m^3)
ρ_o	Unit density or density of water droplet (1000 kg/m^3)
ρ_p	Particle density (kg/m^3)
ϕ	Transported fluid property
τ	Stress tensor
τ_{eff}	Effective stress tensor
Φ_{m1}, Φ_{m2}	Work function of two metals (eV)
χ	Shape factor of particle
∇	Del operator
∇^2	Laplacian operator

Acknowledgements

With special thanks:

- To my major professor, Dr. Ronaldo Maghirang, for patiently editing and giving valuable comments on my manuscript.
- To my committee members, Dr. Larry Erickson, Dr. Larry Glasgow, and Dr. Zhongquan Zheng, who also spent time reading and giving helpful comments on my manuscript.
- To Dr. Oliver Weaver, for representing the Graduate School as outside chair during my defense.
- To the funding agency of my research, U.S. Department of Defense through M2 Technologies. Also to Ryan Green and Blase Leven, who are also members of our project team.
- To Bala Kakumanu, Rachit Yadav and Brandon Braley, for the help in my initial experiments.
- To Dr. Kenneth Klabunde and Aaron Yang, for the nanorod samples.
- To Dr. Steve Eckels, for allowing me to use the ME department's FLUENT software. To Eric Waters, for the installation of the software. And to Evraam Gorgy for helping me to access the FLUENT software at ME.
- To Steve O'Halloran, Ning Zhang and FLUENT acad support group, for technical help in using the FLUENT software.
- To my friends and laboratory mates, Edna Razote, Josephine Boac, Haidee Gonzales, Emad Almuhanna, Li Guo, and Dr. Sheryll Jerez for their assistance and support in every way.
- To Darrell Oard, for his valuable ideas and help in my experimental set-up. Also to Kevin Hamilton, for his help on the FT-IR chamber construction.
- To Wei Han and the BAE Graduate Students, for their help and friendship.
- To Kent Hampton, for assistance in SEM imaging of my samples.
- To Roby Joehanes, for help in the statistical analysis of my data.
- To Randy Erickson, Barb Moore and the BAE administrative staff, for facilitating necessary documents and supplies that I needed during the study.
- To Lydia Aseneta, Joy Boac and the Filipino community in Manhattan, who imparted valuable help while studying at K-State.
- To Pastor Robert Flack and my churchmates at Grace Baptist Church, for their love and prayers.
- To my HIS (helping international students) friends, Grandma Betty and Grandpa Allan Nelson, for their time and friendship during my adjustment period at K-State.
- To my father-in-law, Barry, mother-in-law, Pam, Grandma Mary Ellen, and Grandpas Donald and Arnold, who continually love and believe in my capability.
- To my family in the Philippines --- Papa, Mama, Ate Maricris, Kuya Edwin, Alex, Lhen and Arlo, who keep on loving and supporting me.
- To my husband Tyler, for his love, patience, and encouragement.
- To my Creator, God and Savior, Jesus Christ, for the unconditional love and forgiveness.

Dedication

To my husband,

Tyler

1. INTRODUCTION

1.1 Background

Nanostructured materials, because of their unique structure and morphology, are of significant interest and promise to revolutionize many key areas of science and technology (Powers et al., 2007; Zhang, 2003). The electronic, magnetic, optical, and chemical properties of these materials have been found to be very different from their bulk forms and depend on size, shape, and composition (Khanna, 1997). One important area of application is air purification. Metal oxide nanostructured particles have been found to be effective in inactivating a wide variety of chemical warfare agents, biological agents, and toxic industrial chemicals, and in detoxification of indoor spaces (Wagner et al., 1999; Carnes and Klabunde, 2002; Decker et al., 2002; Koper et al., 2002). Some metal oxide particles also have been found to be effective in clearing aerosol-type smokes in enclosed spaces (Yadav et al., 2008; Zhang et al., 2007).

In regards to the global market for nanotechnology, the share of nanostructured materials is expected to rise from $152 million in 2005 to $569 million in 2010 at an average annual growth rate of 30.2% (BCC Research, 2005). This rapid increase in the market projection makes basic research (e.g., synthesis of different types of nanoparticles) and applied research (e.g., finding new applications) on nanotechnology a major research priority today in many countries, including the United States.

Biswas and Wu (2005) noted that little research has been conducted to characterize the particle size distribution of airborne nanostructured particles. Most of the characterization studies for toxicological and epidemiological studies have used the Scanning Electron Microscopy and the Atomic Force Microscopy techniques (Wang et al., 2003; Zhang, 2003).

Friedlander and Pui (2004) listed some of the key areas of research to improve physical characterization capabilities of nanoparticles: rapid aerosol nanoparticle measurements, detection and characterization in the low nanometer (<5 nm) size regime, particle standards for size and concentration, and charging behavior throughout the ultrafine and the nanoparticle size regimes. Zhang (2003) also noted that the applications of nanoparticles are not yet fully explored.

1.2 Research Objectives

This research was conducted to investigate the unique characteristics of airborne nanostructured particles, which are important in many applications including air purification, smoke clearing, and obscuration. Specific objectives were to:

(1) measure the size distribution and concentration of aerosolized nanostructured particles using near real-time measurement techniques. These results are important in assessing the effectiveness of nanostructured particles in applications that require optimum concentration and sufficient coverage distribution (i.e., inactivation of harmful agents, detoxification of indoor air, and smoke clearing). Results are also useful in toxicological investigation and in establishing standards and/or threshold limits for nanostructured particles. Information such as the length of time particles stay airborne is also important for development of proper and safe usage and handling methods for these types of particles.

(2) evaluate the infrared (IR) extinction properties of nanostructured particles and compare them with conventional particles. Common IR particulate obscurants used by the military are brass flakes and graphite flakes which are highly toxic to the environment and human health. Results of this study could be used as the foundation for future investigations of nanostructured particles as IR obscurants.

(3) determine the relative chargeability of nanostructured particles. Determination of charge magnitude and charge polarity is crucial for predicting, monitoring, and improving the separation/attraction of fine particles. For example, the charging of airborne nanostructured particles may further enhance their smoke clearing effectiveness and remediation ability.

(4) numerically model the transport of particles in enclosed rooms. Understanding particle-laden turbulent flow is important in solving indoor air quality problems and in controlling particle dispersion.

1.3 Organization of the Dissertation

This dissertation has seven chapters and an Appendix section. This chapter summarizes the rationale, significance, and major objectives behind this research. Chapter 2 reviews the literature related to this research. Chapter 3 deals with real-time measurement of the concentration and size distribution of aerosolized nanostructured particles (specific objective # 1). Chapter 4 focuses on the measurement of extinction properties of nanostructred particles in the mid-IR wavelength range (specific objective # 2). Chapter 5 discusses the chargeability of nanostructured particles using tribocharging (specific objective # 3). Chapter 6 deals with numerical simulation of the transport of particles in enclosed spaces (specific objective # 4). Chapter 7 provides the conclusions and recommendations for future work. The Appendix contains information on the instruments, details of the experimental set-up, and summary of data.

1.4 References

BCC Research. 2005. Global market for nanotechnology application in the life sciences to reach $3.4 Billion by 2010. Available at: www.bccresearch.com. Accessed 08 April 2006.

Biswas, P. and C.Y. Wu. 2005. Nanoparticles and the environment. *Journal of Air and Waste Management Association* 55: 708-746.

Carnes C.L. and K.J. Klabunde. 2002. Unique chemical reactivities of nanocrystalline metal oxides toward hydrogen sulfide. *Chemistry of Materials* 14(4):1806-1811.

Decker S.P., J. Klabunde, A. Khaleel, and K.J. Klabunde. 2002. Catalyzed destructive adsorption of environmental toxins with nanocrystalline metal oxides. *Environmental Science and Technology* 36(4):762-768.

Khanna, S. N. 1997. Effect on properties of reduced size and dimensions. In *Handbook of Nanophase Materials*, 1-13. A. N. Goldstein, ed. New York, NY: Marcel Dekker, Inc.

Koper O.B., J. Klabunde, G.L. Marchin, K.J. Klabunde, P. Stoimenov, and L. Bohra. 2002. Nanoscale powders and formulations with biocidal activity toward spores and vegetative cells of Bacillus species, viruses, and toxins. *Current Microbiology* 44(1):49-55.

Friedlander, S.K. and D.Y.H. Pui. 2004. Emerging issues in nanoparticle aerosol science and technology. Workshop report sponsored by NSF, South California Particle Center, and UCLA.

Powers, K.W., M. Palazuelos, B.M. Moudgil, and S.M. Roberts. 2007. Characterization of the size, shape, and state of dispersion of nanoparticles for toxicological studies. *Nanotoxicology* 1(1):42-51

Wagner, G.W., P.W. Bartram, O. Koper, and K.J. Klabunde. 1999. Reactions of VX, GD, and HD with Nanosize MgO. *Journal of Physics and Chemistry B* 103(16):3225-3228.

Wang, Z.L., Y. Liu and Z. Zhang. 2003. Handbook of nanophase and nanostructured materials. Vol. II: Characterization. New York: Kluwer Academic/Plenum Publishers.

Yadav, R., R.G. Maghirang, L.E. Erickson, B. Kakumanu, and S.G. Castro. 2008. Laboratory evaluation of the effectiveness of nanostructured and conventional particles in clearing smoke in confined spaces. *Fire Safety Journal* 43(1):36-41.

Zhang, J. Z. 2003. Dynamic properties of nanoparticles. In *Handbook of Nanophase and Nanostructured Materials*, Volume 2: Characterization, 219-251. Z.L. Wang, Y. Liu, and Z. Zhang, eds. New York: Kluwer Academic/Plenum Publishers.

Zhang, N., Z.C. Zheng, and R.G. Maghirang. 2007. Numerical simulation of smoke dissipation with dispersed nanoparticle aggregates. *International Journal for Numerical Methods in Engineering.* (DOI: 10.1002/nme.2186).

2. LITERATURE REVIEW

This chapter presents a summary of published information related to this research. In section 2.1, important physical properties, including size and shape, that affect the fate of the particles are emphasized. Section 2.2 deals with extinction properties of particles in the mid-infrared (IR) wavelength range. Important terms are defined and factors affecting the effectiveness of an obscurant are presented; Section 2.3 focuses on electrostatic charging of particles using the tribocharging method. The last section (section 2.4) presents two-phase flows and turbulence modeling using the computational fluid dynamics (CFD) method.

2.1 Particle Characterization

The behavior of particles, including nanostructured particles, in air and how they interact with other airborne entities depend to a large degree on their concentration, particle size distribution (PSD), shape, and electrostatic charge. For example, the settling velocity of a particle is strongly dependent on its size.

Nanostructured particles are agglomerates of nanoparticles. Zhang (2003) defined nanoparticles as materials with size of up to a few hundred nanometers. Their properties are often strongly dependent on their size, shape, and surface (Zhang, 2003).

2.1.1 Particle size distribution

Most ambient aerosols are polydisperse and have a wide PSD (Hinds, 1999). Nanostructured particles are similar to ambient aerosol particles, since they also have a wide size variation ranging from a few nanometers to several micrometers (Khlystov et al., 2004). Peters

et al. (1993) and Hinds (1999) indicated that characterization of PSD of aerosol on an aerodynamic basis is critical in many aerosol-related studies.

The PSD is most often depicted as a log-normal histogram with particle diameter on a logarithmic abscissa and the ordinate representing the particle concentration in a given size class (Powers et al., 2007). It is often described by the geometric mean diameter (GMD) and geometric standard deviation (GSD). The GMD and GSD are the counterparts of mean diameter and standard deviation of a normally distributed curve. The GMD and GSD based on particle number are calculated using the following formulas (Hinds, 1999):

$$\ln \mathrm{GMD} = \frac{\Sigma n_i \ln d_i}{N} \tag{2.1}$$

$$\ln \mathrm{GSD} = \left(\frac{\Sigma n_i (\ln d_i - \ln \mathrm{GMD})^2}{N-1} \right)^{1/2} \tag{2.2}$$

$$N = \Sigma n_i \tag{2.3}$$

where n_i, d_i, and N are the number of particles in group i, midpoint size of each size group i, and total number of particles, respectively.

2.1.2 Particle shape and size

The settling velocity and other dynamic behavior of a particle are affected by both particle size and shape (Cheng et al., 1988). Individual or primary particles can be either spherical or non-spherical in shape. Liquid droplets (less than 1 mm) and some solid particles formed by condensation are spherical; however, most other types of particles are non-spherical. Some have regular geometric shapes such as cube, cylindrical, single crystals or cluster of spheres (Hinds, 1999). The physical and chemical characterization of non-spherical and fractal

particles is an important area of current aerosol research (Friedlander and Pui, 2003; DeCarlo et al., 2004).

A special case of non-spherical particles called aggregates or agglomerates are composed of several primary particles or crushed materials and have irregular shapes (Hinds, 1999; Friedlander, 2000; DeCarlo et al., 2004). Nanostructured particles are examples of aggregates that consist of nanoparticles.

The shape of a particle affects its drag force, F_D, and settling velocity. For example, when particles are suspended in fluid, the F_D on a non-spherical particle is generally greater than that on a sphere of the same volume moving with the same velocity (Cheng et al., 1988). To account for the effect of shape on particle motion, the dynamic shape factor, χ, is applied to Stoke's law. This factor is defined as the ratio of the actual resistance force of the non-spherical particle to the resistance force of a sphere having the same volume and velocity as the non-spherical particle:

$$\chi = \frac{F_D}{3\pi\mu V d_e} \tag{2.4}$$

where μ is the viscosity, V is relative velocity of the particle with respect to the fluid, and d_e is the equivalent spherical diameter (Hinds, 1999). Spheres have a χ value of 1. Dynamic shape factors greater than 1 indicate a higher degree of deviation from a spherical shape (Cheng et al., 1988). A cube, for example, has a χ value of 1.08 and a compact cluster of three spheres has a χ value of 1.15 (Hinds, 1999).

The common method of sizing of solid particles that are irregular or non-spherical is the use of an equivalent diameter. Baron et al. (2001) defines equivalent diameter as the diameter of a sphere having the same value of a specific physical property as the irregularly-shaped particle being measured. Two common types of equivalent diameter are the aerodynamic diameter (d_a)

and mobility diameter (d_{me}). The d_a of a particle is the diameter of a standard unit density (1000 kg/m^3) sphere having the same gravitational (terminal) settling velocity as the particle being measured whatever its size, shape, and density (Hinds, 1999; Powers et al. 2007). The equivalent mobility diameter, on the other hand, is defined as the diameter of a sphere with the same mobility as the particle in question (Friedlander, 2000; Baron et al., 2001). DeCarlo et al. (2004) further defines d_{me} as the diameter of a sphere with the same migration velocity in a constant electric field as the particle of interest. The d_a depends on particle density (ρ_p) (DeCarlo et al., 2004). The d_{me} depends on particle cross-section.

To convert d_a to d_{me}, the following equation may be used (Hinds, 1999):

$$\sqrt{C_a d_a} = \sqrt{\frac{C_{me}\rho_p}{\chi\rho_o}}\, d_{me} \tag{2.5}$$

where C_a, C_{me}, and ρ_o are the slip correction factor for d_a, slip correction factor for d_{me}, and unit density (1 g/cm^3), respectively. The slip correction factor, C_a or C_{me}, is calculated using the following equation (Hinds, 1999):

$$C = 1 + \frac{2\lambda_p}{d_p}\left(1.142 + 0.558e^{\frac{-0.999 d_p}{2\lambda_p}}\right) \tag{2.6}$$

where λ_p is the mean free path (6.65e^{-8} m) and d_p is the particle diameter (d_a or d_{me}).

2.1.3 Particle concentration

Particle concentration can be expressed in terms of either number or mass. Particle number concentration, C_n, which is expressed as number of particles per unit volume of gas, is usually used to characterize clean rooms and atmospheric cloud condensation nuclei. On the other hand, particle mass concentration, C_m, which is expressed as particle mass per unit volume of gas, is usually used for air pollution standards both for the atmosphere and for industrial emissions (Friedlander, 2000). Current indoor air quality standards are expressed in terms of C_m

as total or respirable dust. One major limitation of using particle mass standards is that the values of C_m are heavily biased towards larger particles. The mass of a small number of large particles can be significantly larger than the mass of a large number of small particles. In ambient environment, number concentrations of small particles are usually significantly higher than those of the larger particles. Therefore, it appears that for health risk assessments, knowledge of C_n could be more important than knowledge of C_m (Oberdorster et al., 1994; Seaton et al., 1995; Li et al., 1996). Because of this, more research efforts have been directed towards experimental characterization of particle number concentration (Morawska et al., 1998; Pomeroy et al., 2000).

The number concentration, C_n, of particles can be converted to the mass concentration, C_m, using: (Hinds, 1999)

$$C_m = \frac{\pi}{6}\rho_p C_n \left(\frac{d_p}{\sqrt{\rho_p}} \right)^3 \qquad 2.7$$

where ρ_p and d_p are density and diameter of the particle, respectively.

2.1.4 Measurement methods

The assessment of exposures to particles often requires instruments that provide a fairly rapid measurement of particle concentration by size (Peters et al., 2006). Previous method of size distribution analysis involves inertial impactor (e.g., cascade impactor). This method has the disadvantage of being labor intensive (Stein et al., 2003; Myrdal et al., 2004) and the precision is limited due to the imperfectly sharp stage collection efficiency curves and manufacturing tolerances (Friedlander, 2000).

In order to study aerosols with wide PSD, a combination of instruments is necessary, because currently there is no single instrument that is available to cover wide PSDs (Khlystov et

al., 2004). In several recent studies, a combination of real-time instruments, such as a Scanning Mobility Particle Sizer (SMPS) and an Aerodynamic Particle Sizer® (APS), is employed (Shi et al., 2001, Shen et al., 2002; Hand and Kreidenweis, 2002; Khlystov et al., 2004). Many studies have evaluated the reliability of these two real-time instruments by using generated aerosols with known density and size (Morawska et al., 1998; Sioutas et al., 1999; Stein et al., 2003). Peters et al. (2006) used the APS (Model 3321, TSI, Inc., Shoreview, MN) as a reference to evaluate the performance of other real-time instruments such as the portable aerosol spectrometer. The measurement performance of the SMPS (Model 3934, TSI, Inc., Shoreview, MN) and the APS (Model 3310A, TSI, Inc., Shoreview, MN) were evaluated by Sioutas et al. (1999) to assess their ability to obtain C_m from near real-time C_n values. Comparisons were made between mass concentrations determined from these real-time instruments and the time-averaged mass concentrations collected on open-faced filters, as well as with the Micro-Orifice Uniform Deposit Impactor (MOUDI). Results generally showed good agreement in the mass concentration obtained.

Peters et al. (1993) combined the results of a Differential Mobility Particle Sizer (DMPS) and an Electrical Aerosol Analyzer (EAA) with the data from an APS to obtain the mass distribution of sodium chloride solution from the measured number distribution. A Low Pressure Impactor (LPI), a direct measurement method, was used to verify the combined results. The near-real time measurements provided mass distribution data that compared favorably with that from the LPI. Their study, however, did not account for the temporal change of the GMD and concentration of the aerosols.

Because of different measurement principles (e.g., electrical mobility versus aerodynamic sizing), difficulties arise in attempts to create a single spectrum from data measured with SMPS

and APS (Khlystov et al., 2004). Shen et al. (2002) approached this problem by selecting certain kinds of data from each instrument. For example, the SMPS was used up to a certain size, and beyond that size the APS was used. Hand and Kreidenweis (2002) first matched the optical particle counter (OPC) with the SMPS spectrum by finding an optimal refractive index; the APS data were then matched to the modified OPC spectrum by finding an effective density that would best fit with the OPC. The reason for matching the APS and the OPC and directly to the SMPS was that the size overlap between the APS and the SMPS is rather small (Khlystov et al., 2004).

Khlystov et al. (2004) developed a simple algorithm for combining d_{me} and d_a measured by the SMPS (Model 3936N25) and APS (Model 3320), respectively, to create a wider size distribution range for ambient aerosols. The algorithm provided a ratio of the ρ_p value to the χ value in the overlap range. The APS was found to agree well with the SMPS in the overlap size range (580-720 nm). Their result indicated constant counting efficiency and close to 100% except for the first APS channel. The integrated volume concentrations from SMPS-APS showed good correlation with $PM_{2.5}$ mass concentration obtained with a Tapered Element Oscillating Microbalance (TEOM). Both the GMD and GSD showed good correlation of the SMPS-APS with MOUDI cascade impactor. The size-fractionated comparison of MOUDI and the SMPS-APS appeared to be well-correlated.

Congrong et al. (2005) studied indoor particle deposition rates by analyzing the number concentration decay curves derived from the SMPS and APS for sub-micrometer and super-micrometer particles. Measured deposition rates were shown to be particle size dependent. The response of two OPCs in comparison with that of an APS (Model 3321, TSI, Inc., Shoreview, MN) was studied by Peters et al. (2006) for three sizes of monodisperse and one polydisperse aerosols. Similar results were obtained from the three instruments.

2.1.5 Summary

The behavior of particles, including nanostrucutred materials, in air and how they interact with other airborne entities depend on their concentration, size distribution, and shape. Particle concentration can be expressed in terms of either number or mass. Recent methods to measure both concentration and size distribution involve a combination of Scanning Mobility Particle Sizer (for sub-micrometer particles) and Aerodynamic Particle Sizer (for the larger particles).

2.2 Infrared Extinction Properties

2.2.1 Infrared (IR) obscurant and extinction coefficient

Obscurants are natural (e.g., fog, rain, dust) or manmade (e.g., smoke) airborne particles that can attenuate the electromagnetic energy. Infrared (IR) particulate obscurants are IR absorbing particles or particles that have low IR transmission. For obscurants to be considered effective, they must exhibit high extinction coefficients and at the same time not be harmful to human health and environment. The extinction coefficient or extinction cross-section of an obscurant is a measure of its ability to attenuate the incident energy at a certain wavelength (Shi et al., 1998).

Highly conducting materials (e.g., brass flakes, graphite flakes) are effective IR obscurants. Materials such as salts, metal oxides, and semiconductors also have moderately strong molecular vibration in the IR region (Owrutsky et al., 2001). Molecular vibrations (e.g., stretching and bending) and rotations of a material are indications of its IR absorption properties (Stuart, 2004). Other factors that affect extinction coefficients include chemical composition, size distribution, number concentration, and morphology of particles (Ladouceur et al., 1997; Shi et al., 1998; Widmann et al., 2005). Morphology is particularly important as it influences the coagulation process and removal of particles from the air (Colbeck et al., 1997). The molecular

structure of the material forming the aerosol, primary particle size, and structure of the aggregate also affect the efficiency of obscurants (Dobbins et al., 1994; Shi et al., 1998). Other important criteria for an effective obscurant are ease of deployment, availability, and cost (Owrutsky et al., 2000).

Infrared obscurants have played a major role in military operations because they provide protection of military personnel, equipment, and installation from IR seeking sensors of unfriendly forces (Singh et al., 1994; Butler, 1998). Obscurants that are effective in IR have received renewed interest due to the increasing threat of emerging IR sensors (Farmer and Krist, 1981; Farmer et al., 1982; Shi et al., 2003; Singh et al., 1994; Appleyard and Davies, 2004b; Wang et al., 2004). These obscurants can screen the potential target from threatening IR sensor systems (Singh et al., 1994; Ladouceur et al., 1997; Shi et al., 1998; Shi et al., 2003).

The effectiveness of an obscurant for military applications may be represented either by mass extinction coefficient (extinction cross section per unit mass), σ_m, or the volume-extinction coefficient (extinction cross section per unit volume), σ_v, depending on how the material is deployed (Owrutsky et al., 2000). Mass and volume extinction coefficients are related to one another by the packing or tap density (Owrutsky et al., 2000). For military applications, the σ_v value is generally more important than the σ_m value because most deployment methods (e.g., grenade) are volume- rather than mass-limited (Owrutsky et al., 2001).

Extinction coefficients are typically expressed as averages over the spectral band of interest (i.e., band-averaged extinction coefficients) (Farmer, 1991). In military applications, the wavebands of increasing importance are the 3-5 μm (short) and 8-12 μm (long) wavelengths in the mid-IR region. These ranges are the main "atmospheric windows" or the region in the electromagnetic spectrum in which IR transmission is close to 100% regardless of the presence

of atmospheric gases, including water vapor and carbon dioxide (CO_2) (Jacobson, 1999; Bailey et al., 2002; Hutchison and Cracknell, 2005).

2.2.2 Common IR particulate obscurants

Common IR particulate obscurants include brass flakes and graphite flakes. Of all the materials tested at the Naval Research Laboratory (NRL), graphite (with nominal 2 μm particle size) had the highest σ_m value (Owrutsky et al., 2000). Also, graphite has much lower toxicity (rated 4 by Environmental Protection Agency (EPA) on a scale of 0-9) and environmental impact than brass (with EPA toxicity rating of 9). The σ_m values were reported by Ladouceur et al. (1997) to be between 1.4 and 2.6 m^2/g for graphite and 0.08 m^2/g for brass; therefore, graphite was clearly more attractive. However, the U.S. Army chose brass over graphite because brass has higher packing density, which is about three times that of graphite (Ladouceur et al, 1997). Carbon black was also tested and was identified as another good obscurant material (Owrutsky et al., 2000; 2001) although its packing density is small.

2.2.3 Calculation of extinction coefficients

The σ_m value is calculated based on Beer's law, which relates the optical measurement to the mass concentration of the obscurant (Smith, 1996):

$$\sigma_{m_{(\lambda)}} = \frac{2.303 A_{(\lambda)}}{C_m L} \tag{2.8}$$

$$A_{(\lambda)} = \log\left(1 \Big/ T^*_{(\lambda)} \right) \tag{2.9}$$

where A is the absorbance (dimensionless), T^* is the transmittance (dimensionless), λ is wavelength, C_m is the particle mass concentration (g/m^3), and L is the path length (m). The σ_v (m^2/cm^3) value is obtained by multiplying the σ_m value by the tap density (g/cm^3):

$$\sigma_{v(\lambda)} = \sigma_{m(\lambda)} \cdot (\text{tap density}) \tag{2.10}$$

2.2.4 Measurement of extinction coefficients

Many theoretical and experimental investigations have been conducted to determine the extinction coefficients of various particles. Appleyard (2007) modeled the extinction properties of non-spherical particles as a function of particle orientation with respect to the incident light. Appleyard (2006) noted that, based on theoretical analysis, the most important property to maximize and manipulate in the optical properties of metal particles is conductivity. Additionally, structures such as thin disc flakes and thin fibers had the maximum extinction coefficients (Appleyard and Davies, 2004b; Appleyard, 2006). Comparison of theoretical and experimental results on extinction coefficients indicated good agreement for TiO_2 and SiO_2 (Appleyard and Davies, 2004a) but not for iron oxides (Owrutsky et al., 2000; 2001). Optical extinction spectra for different military smokes (e.g., red phosphorus, fog oil) have been obtained experimentally in the 3-5, 8-13, and 0.4-2.4 μm spectral regions (Milham, 1976). Shi et al. (1998) focused on the size designing aspect of the aerosol in order to find the optimum particle size distribution that provides the maximum band extinction per unit mass. Three successive studies were conducted by the NRL in an effort to find a suitable obscurant to replace brass due to its toxicity. The first study (Ladouceur et al.,1997) constructed an experimental apparatus using the Fourier Transform Infrared (FTIR) spectrometer and measured the extinction properties of readily available powders with acceptable toxicological and optical properties (i.e., boron nitride, boric acid). They found good agreement between experimental and theoretical methods (i.e., Mie theory) for boron nitride, although brass still has higher extinction coefficient. The second and third studies (Owrutsky et al., 2000; 2001) focused on experimental measurements of several powders, including natural graphite, glassy carbon spheres, iron oxide,

and carbon black (Owrutsky et al., 2000; 2001). The PSD appeared to dramatically affect the extinction properties of the particles they studied (Owrutsky et al., 2000; 2001).

According to Widmann et al., (2005), direct experimental measurement is the preferred approach to determine the extinction coefficient of particles. This approach, however, poses a challenge due to difficulty in measuring the IR absorption into the particle-laden flow and the mass concentration corresponding to that transmission value (Owrutsky et al., 2000).

Moreover, numerous studies on extinction coefficient determination are limited in the visible and near-IR regions of the electromagnetic spectrum and not in the mid-IR region (Appleyard and Davies, 2004a; Widmann et al., 2003).

2.2.5 Summary

Infrared particulate obscurants are IR absorbing particles or particles that have low IR transmission. For obscurants to be considered effective, they must exhibit high extinction coefficients and at the same time not be harmful to human health and environment. Highly conducting materials (e.g., brass flakes, graphite flakes) are effective IR obscurants. The effectiveness of an obscurant for military applications may be represented either by the mass extinction coefficient (extinction cross section per unit mass) or the volume-extinction coefficient (extinction cross section per unit volume). For military applications, the volume extinction coefficient is generally more important than the mass extinction coefficient because most deployment methods (e.g., grenade) are volume- rather than mass-limited. Direct experimental measurement is the preferred approach to determine the value of the extinction coefficient of particles. Numerous studies of the extinction coefficient determination are limited in the visible and near-IR regions of the electromagnetic spectrum and not in the mid-IR region.

2.3 Electrostatic Charging

Electrostatic charge is one of the three most important parameters governing aerosol behavior; the other two are particle size and shape. A particle with charge, q, in an electric field of strength, E_f, experiences a force of strength $F_e = qE_f$. Under normal conditions, an atom is electrically neutral because the positive charge of the protons is balanced by the negative charge of the electrons (Tianxiang, 1999). In typical ambient conditions, aerosol particles usually carry only a small number of elementary charges because of the low ion densities and slow charge transfer kinetics (Tianxiang, 1999).

For dry, solid materials, the charge carriers are the electrons and ions. The electron is the basic element of charge. Ions can be either positive or negative. A particle that is charged with negative polarity ion must have an electron transferred to the surface. If the polarity of charge is positive, electrons must then be given up by the particle (Liberto, 1994). Charging of particles occurs in normal atmospheres containing about 10^3 ion pairs/cm^3 (Colver, 1999).

2.3.1 Charge measurement

Several instruments (i.e., atomic force microscope, laser Doppler tracking devices) are capable of detecting charge interaction at the particle level; other instruments depend on some cumulative electrostatic effect (i.e., Faraday cage, particle anemometers, and electrostatic voltmeters) (Colver, 1999).

A Faraday cage or cup consists of two conducting enclosures, one is enclosed and insulated from the other. The outer enclosure serves to shield the inner enclosure. Any net charge within the inner cup will induce an equal magnitude of net charge on the outer cup which can then be detected as a voltage or charge using a high impedance device such as an electrometer (ASTM Standards, 1997). It is common practice to report triboelectric charge on a

charge-to-mass basis when using the Faraday cage method since net charge and mass are easily measured (Colver, 1999). However, triboelectric charging is more closely related to the surface area of the particles rather than to volume or mass, such that the particle diameter should also be reported along with the charge (Colver, 1999). A disadvantage of the Faraday cage method for powders containing both positive and negative charge (bipolar charge) is that only the net charge is indicated.

2.3.2 Tribocharging of particles

Solid materials are usually charged by induction, corona, and tribocharging (Higashima and Asano, 1998). Colver (1999) noted that charging of solid and liquid particles is also associated with other phenomena including flame ionization, thermionic emission, radioactive emission, phase change, and particle breakup. Only the tribocharging process is discussed in the following sections since it is the main interest of this research.

When two materials are rubbed together electrical charge is usually transferred from one to the other. This phenomenon is called triboelectrification or tribocharging. It is one of the oldest yet still misunderstood methods of charging (Lowell and Rose-Innes, 1980). Matsuka and Masuda (2003) noted that in spite of the long history of contact charging, there are still unsolved problems and inconsistent experimental results. This is likely due to the many factors affecting tribocharging, including the physical, chemical and electrical characteristics of the particles, and environmental conditions.

In powder tribocharging, electrons are transferred by direct physical contact with the surface of the powder particle (Liberto, 1994). The spontaneous transfer of electrons or ions between two dissimilar contacting materials leaves the surfaces oppositely charged following separation (Colver, 1999). According to Makin (1974), intrinsic charging of particles is

achieved to some extent when two materials of different work functions are in contact. A contact potential of approximately 1 V enables alignment of the Fermi level and there is a charge transfer between materials (Makin, 1974).

The physics of tribocharging centers on the idea that under friction some materials give up electrons easily and that other materials readily accept electrons (Liberto, 1994). The triboelectric series, which is a loose ranking of a material's polarity after tribocharging with another material, is usually used. The triboelectric series (Fig. 2.1) shows that materials that most easily give up electrons (donors) are at the top and those that most readily accept electrons (acceptors) are at the bottom. The farther apart the materials are on the series, the more charge will be transferred by contact (Liberto, 1994). One of the best acceptors in the triboelectric series is polytetrafluorethylene (PTFE) or Teflon. Thus, most materials rubbed on PTFE will be positively charged. If the coating material is a better acceptor than PTFE, then the resultant charge on the material will be negative (Liberto, 1994).

Banerjee and Law (1995) studied the triboelectric chargeability of pecan pollen and lycopodium using the commercial Teflon® and nylon chargers. The pecan pollen and lycopodium have bimodal size distribution with diameters of 0-15 µm or 40-50 µm and 5-10 µm or 20-30 µm, respectively. Their results indicated that tribocharging is a feasible method of imparting charge to pollen in electrostatic pollination technology.

2.3.2.1 Tribocharging in powder coating

The powder coating industry is one of the commercial applications of tribocharging. The electrostatic application of powder coating to the part that needs to be coated typically starts with fluidization or the process where the powder to be sprayed is mixed with compressed air (Liberto, 1994). The fluidized powder is pumped from the container and supplied to the spray

guns for charging. The charged powder then moves towards the grounded work piece and the electrostatic attraction makes the charged powder adhere to the part. The spray guns are sensitive to powder formulation, particle size, and environmental conditions. Because of their sensitivity to coating variables, the spray guns are less forgiving in operation wherein charge is not easily controlled by the end-user (Liberto, 1994). Charge transfer occurs only at the small contact area of impact, but it is necessary to have many impacts to the gun to obtain high charge levels on the powder particles (Liberto, 1994).

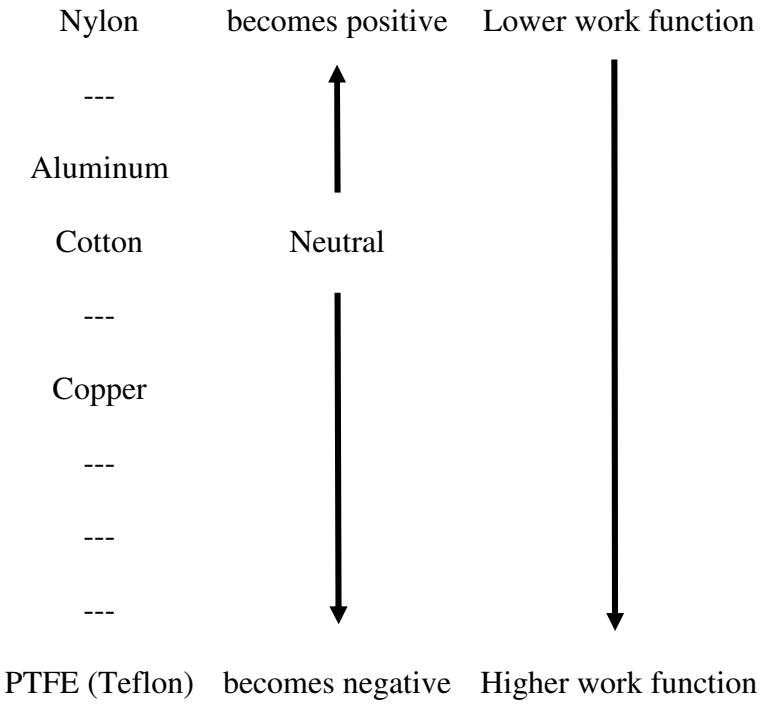

Figure 2.1 An example of a triboelectric series with its corresponding relative work functions (Tianxiang, 1999; Liberto, 1994).

2.3.2.2 Factors affecting tribocharging

According to Mazumder et al. (2006), the amount of triboelectric charge exchanged between two contacting surfaces depends upon their relative speed, difference in work function, and on the pressure between the surfaces in contact. In their work, as the pressure increased, the

area or the number of contact points also increased (Mazumder et al., 2006). Plowman (1995) also noted that charge depends on a number of factors such as conductivity, speed of separation/rubbing, pressure, and contact area. Colver (1999) cited that tribocharging of contacting materials is the result of differences in surface potentials or Fermi levels, as well as, the physical nature of contact. Environmental factors such as monolayers of adsorbed gases can also affect on charging between surfaces (Colver, 1999).

Tianxiang (1999) investigated the particle charge and charge exchange related to triboelectric beneficiation of physical mixtures of fine particles (i.e., silica beads). The magnitude of charge and charge exchanged was measured by the Faraday cup and laser Phase Doppler Particle Analyzer (PDPA). In their experiment, charging velocity and charging duration were the most important factors affecting tribocharging. They also found that the charge on the particle surface could become saturated well below a theoretical maximum charge limit due to charge backflow.

2.3.2.2.1 Work function and contact potential difference

According to the surface theory of electrostatic charging, when two materials are in contact, the difference in work functions causes electron transfer between the contacting materials until the Fermi levels are equalized (Lowell and Rose-Innes, 1980). Work function is the energy required for moving an electron from Fermi level (the highest occupied energy level at 0 K) to the free state. Usually a material that is able to lose electrons has lower work function while materials that gain electrons have high work functions (Frese, 1979). Work functions depend not only on the internal structure of materials, but also on their surface contamination. The drawback is for most materials, the work function values are not available (Tianxiang,

1999). However, relative work functions could be predicted qualitatively if the charge polarities and magnitudes of contact materials are known.

Trigwell et al. (2003) performed experiments on tribocharging (by milling with stainless steel beads) of various powders of different PSDs. Results showed that the charge acquired by the powder could be correlated with the actual work function difference between the powder and the stainless steel. Ultraviolet and x-ray photoelectron spectroscopy were performed on various powders used and showed that work functions increased with surface contamination and oxidation. Moreover, their experiments showed that while charge acquired increased with particle size, the charge distribution was generally bipolar.

When two metals of different work functions are in contact with each other, a charge exchange, Q_c, takes places by electron tunneling. The maximum potential difference between the materials equals the difference in the work functions; generally, a larger difference in work functions can cause more electrons to be transferred (Tianxiang, 1999). The contact potential difference, V_c, is given by (Mazumder et al., 1994):

$$V_c = \frac{\left(\Phi_{m2} - \Phi_{m1}\right)}{e} \tag{2.11}$$

$$Q_c = C_{12} V_c \tag{2.12}$$

where Φ_{m1} and Φ_{m2} are the work functions in electron volts, eV, of materials 1 and 2, respectively; C_{12} is the capacitance between the two metals; and e is the electrostatic charge.

While the mechanisms of electron transfer between metals have been well established both in theory and experiments, contact charging mechanisms between a metal and a polymer and between two polymers are not as well understood (Mazumder et al., 1994).

2.3.2.2.2 Surface contact

Surface contact is another major contributing factor in tribocharging. The greater the surface contact, the greater is the resulting net charge. On the surface of a dielectric material, the positions of the static charges are fixed and therefore, the charge separation between either a metal and a dielectric or two dielectrics must depend upon the actual area of contact (Schnurmann, 1941). The electrical charges at the surface of a metal are mobile, thus, the charge separation between two metals in direct contact is independent of the area of contact (Schnurmann, 1941).

Mazumder et al. (1994) simultaneously measured the particle size and electrostatic charge of triboelectrically charged powder paint and other powders in the particle size range of 1 to 65 µm using the electrical single particle aerodynamic relaxation time (E-SPART) analyzer. Their results showed that the magnitude of charge increased linearly with surface area of the particle and consequently, the charge-to-mass ratio decreased inversely with respect to aerodynamic size in the entire size range.

According to Lowell and Akande (1988) and Murtomaa (2002), it is usually difficult to repeat the experiments in tribocharging because of the significant role of the surfaces of the samples in the charge transfer process where exactly similar surfaces are quite impossible to obtain.

2.3.2.2.3 Surface chemistry

Surface chemistry (e.g., surface composition, contamination and oxidation) was determined to control partly the amount and polarity of charge transferred between two dissimilar materials, such as metals and polymer powder (Trigwell et al. 2003; Sharma et al., 2004; Mazumder et al., 2006). When an oxidized metal is used as a charging material, it is speculated that the oxidized layer rather the base metal determines the charge imparted on

particle surfaces (Tianxiang, 1999). It was also observed that metals with higher levels of contamination showed smaller increase in work function, while polymers appeared to cause large increase in work function with only small deviation in its surface composition (Mazumder et al., 2006).

2.3.2.2.4 Electrical properties of particles

Conductivity is an electrical property of a material that indicates its ability to conduct electricity and is directly proportional to charge, charge density, and drift mobility. Generally, a material is considered a conductor when conductivity is greater than 10^5 $Ohm^{-1}m^{-1}$ and a non-conductor or dielectric when conductivity is below 10^{-8} $Ohm^{-1}m^{-1}$ (Tianxiang, 1999).

Powders having a low bulk density resistivity, 10^7-10^9 Ohm-m, can be used successfully with electrostatic guns only for small particles (~5 μm) due to charge and particle loss, while resistivities > 10^{12} Ohm-m are desirable for use with larger particles. One rule of significant charging is that at least one of the materials should have a bulk resistivity > 10^7 Ohm-m (Colver, 1999). A high specific resistivity of the powder is essential to retain charge in the layer (Kleber and Makin, 1998).

Permittivity is another parameter influencing the charging process between two solid materials. It is a measure of the ability of the material to become polarized. Coehn's law states that when two materials are in contact with each other, the one with the highest permittivity becomes positive (Plowman, 1995; Tianxiang, 1999).

2.3.2.2.5 Charge backflow and gaseous discharge

Charge backflow is a phenomenon that happens when upon separation, some electrons flow back under the action of a potential difference between the materials. Charge backflow results in reduced net charge on the contacting surfaces. Charge backflow is also related to

relaxation time. Fast separation or longer charge relaxation time results in lower charge backflow. The charge relaxation time depends on electrical properties of contacted materials and the environmental conditions during contact such as surface cleaning, impurity levels, contact geometry, and temperature (Tianxiang, 1999). A material of high conductivity or low permittivity has a short charge relaxation time, resulting in high charge backflow (Tianxiang, 1999).

2.3.2.2.6 Environmental factors

Moisture adsorbed on the surface can dramatically lower the charge magnitude (Tianxiang, 1999). Ambient conditions, especially humidity, can decrease the surface and volume resistivities of materials, and therefore affect the characteristics of tribocharging (Banerjee and Law, 1995). Decrease in resistivity due to higher humidity would cause a decrease in tribocharging by lowering the charge decay time constant.

2.3.2.3 Gaussian limit

For solid particles charged by triboelectrification, the maximum charge-to-mass ratio, $(q/m)_{max}$, attainable or the Gaussian limit is given by the equation (Banerjee and Law, 1995; Tianxiang, 1999):

$$\left(\frac{q}{m}\right)_{max} = \frac{6\varepsilon_o E_a}{\rho_p d_p} \tag{2.13}$$

where ε_o is the permittivity of free space (8.85×10^{-12} F/m), E_a is the breakdown strength of air under normal temperature and pressure(3 MV/m), ρ_p is the density of the particle, and d_p is the particle diameter. The charge on the particle surface could become saturated well below its theoretical maximum charge limit possibly due to charge backflow (Tianxiang, 1999).

2.3.3 Charging of Nanoparticles

Chen and Pui (1999) mentioned that because of their small cross sections, nanoparticles are difficult to charge, and when charged, can easily be lost within the charging device. They also added that the challenge in the design of a nanoparticle charger is obtaining high charging efficiency while minimizing particle loss.

Alonso et al. (2003) mentioned that it is of great interest to have a device that is highly-efficient charger for nanoparticles, so that they can be subsequently collected by electrostatic precipitation. As the particle size decreases, electrical charging becomes more and more difficult, as most of the particles below about 10 nm remain uncharged and thus, penetrate the electrostatic precipitator without being collected (Alonso et al., 2003). Alonso et al. (2003) further added that the particle charging efficiency (i.e., the number fraction of originally neutral particles that acquire one or more electrical charges in the corona field) increases with particle size in such a manner that one can safely assume that all the particles larger than about 50 nm become charged and can, thus, can be deposited on the collecting electrode. Another major limitations with nanoparticles is that the charge transport between particles is very limited compared to bulk single crystalline materials (Zhang, 2003).

2.3.4 Summary

The amount of triboelectric charge exchanged between two contacting surfaces depends upon numerous factors, including their relative speed, difference in work function, pressure between the surfaces in contact, physical, chemical and electrical characteristics of the surfaces, and environmental conditions. Nanoparticles because of their small cross sections are difficult to charge, and when charged, can easily be lost within the charging device.

2.4 Numerical Simulation of Particle Transport

The deposition of particles on surfaces in indoor environments has significant implications for many areas such as indoor air quality and human health (Lai, 2004; Zhang, 2005). Indoor particles are usually polydisperse with size range that extends from submicron to larger than 100 μm in diameter. This feature makes the transport process complicated since deposition is strongly related to particle size (Gao and Niu, 2007). Gao and Niu (2007) noted that in order to address indoor air quality problems and control particle dispersion, understanding of particle-laden turbulent flow is important. However, limited data are available on the dispersion and deposition of particles (Lai, 2004). Also, the present knowledge on turbulence limits the further exploration of the nature of interaction between turbulence and individual particles (Gao and Niu, 2007).

2.4.1 Two-phase flows

Two-phase flows are encountered in a wide range of flow configurations. A sub-category of two-phase flows is the dispersed phase flows in which one phase does not constitute a connected continuum like the particles in a particle-laden flow (Crowe et al., 1996). Study of two-phase flows has applications to many natural systems, including environmental particulate pollution problems.

The dispersed phase can be classified as either dilute or dense (Hari, 2003; Crowe, 1982). In the case of dilute flows, the forces exerted by the fluid control the particle motion and particle-particle interactions become insignificant (Hari, 2003). In a dense flow, the particle motion is controlled primarily by particle-particle collisions or interactions (Hari, 2003; Crowe et al., 1996).

The dispersed or secondary phase is considered dilute if its volume fraction in a cell/domain is < 10 %. In the dilute case, the average inter-particle distance is around twice the particle diameter; thus, interaction among particles can be neglected (FLUENT, 2006).

Coupling between phases depends on particulate loading. Particulate loading, β, is defined as the material density ratio, γ, of dispersed and continuous/carrier phase:

$$\beta = \frac{\alpha_p}{\alpha_c}\gamma \tag{2.14}$$

$$\gamma = \frac{\rho_p}{\rho_c} \tag{2.15}$$

where α_p, $\alpha_{c,}$, $\rho_{p,}$ and ρ_c are the particulate volume fraction, continuous phase volume fraction, particle density, and carrier material density, respectively. The material density ratio is generally greater than 1000 for gas-solid flows.

For very low particulate loading ($\beta << 1$), the coupling between phases is one-way, that is, the fluid carrier influences the particles via drag and turbulence, but the particles have no influence on the carrier fluid (FLUENT, 2006).

Using the parameters above, it possible to estimate the average distance between individual particles of the particulate phase, which is important for determining how the dispersed phase should be treated (Crowe et al., 1998; FLUENT, 2006):

$$\frac{L^*}{d_p} = \left(\frac{\pi}{6} \frac{L^* + \left(\frac{\beta}{\gamma}\right)}{\left(\frac{\beta}{\gamma}\right)} \right)^{1/3} \tag{2.16}$$

where L* is the average inter-particle distance. For an interparticle space of about 8 (very low particulate loading), the particle can be treated as isolated.

2.4.2 Computational fluid dynamics (CFD)

Crowe et al. (1996) noted that numerical simulation of fluid-particle flows plays a key role by aiding fundamental research and complementing engineering systems design. A technique that utilizes numerical simulation methods, called computational fluid dynamics (CFD), has been widely used in predicting air flow patterns and particle transport and distribution in enclosed spaces and it has been proven to offer a competitive and flexible alternative to physical modeling (Liddament 1991; Haghighat, et al., 1992; Jones and Whittle, 1992; Zhang and Chen, 2007). Konecni et al. (2002) noted that CFD codes offer some advantages such as time and cost savings over experimental techniques in investigating fluid flow. FLUENT is one of the commercially-available CFD software products that are widely used for modeling fluid flow and heat transfer in complex geometries.

2.4.3 Approaches in modeling two-phase flows

There are two approaches to model two-phase flows: Eulerian-Eulerian and Eulerian-Lagrangian (Gao and Niu, 2007). The selection between the two is based on the research objective, required computational resources (cost), and characteristics of the problem under examination (Loth, 2000; Gao and Niu, 2007; Zhang and Chen, 2007).

2.4.3.1 Eulerian-Eulerian approach

The Eulerian-Eulerian approach is also called the two-fluid model. In this model, particulate phase is treated as another flow and calculated in the fixed coordinate system (Zhang, 2005). This is similar to solving equations for two gas species in a binary mixture, except that the momentum transfer between the two fluids are not the same (Zhang, 2005; FLUENT, 2006). Moreover, in the Eulerian-Eulerian approach, the conservation equations for the fluid and particle phases are independently solved, by assuming average particle phase properties (Hari,

2003). The interaction between phases is modeled by means of interphase terms that are included in the conservation equations.

In FLUENT, three different Eulerian-Eulerian models are available: (1) the volume of fluid (VOF) model for the surface-tracking designed for two or more immiscible fluids; (2) the mixture model designed for two or more phases (fluid or particulate); and (3) the Eulerian model (most complex and expensive), which solves a set of *n* momentum and continuity equations for each phase (FLUENT, 2006).

Holmberg and Li (1998) presented two requirements for the Eulerian-Eulerian approach in modeling of indoor environments. First, the particle size should be significantly smaller than the Kolmogorov microscale. The Kolmogorov microscale is at the magnitude of 1 mm for normal ventilated room, which is several times greater than indoor particle sizes (Holmberg and Li, 1998; Etheridge and Sandberg, 1996; Gao and Niu, 2007). Second, there should be a sufficient number of particles in each computational cell so that the particulate phase can be statistically assumed as a continuum (Gao and Niu, 2007).

With the one-way coupling of flow to particles, the Eulerian-Eulerian method uses only particle concentration equations to couple with momentum and turbulence equations. The particle phase follows the following transport equations (Zhang and Chen, 2007):

$$\frac{\partial \rho\varphi}{\partial t} + \frac{\partial}{\partial x_i}\left(\rho \bar{u}_i \varphi - \Gamma \frac{\partial \varphi}{\partial x_i}\right) = S_c \tag{2.17}$$

$$\Gamma = \rho\left(D + \nu_p\right) \tag{2.18}$$

where φ is the transported fluid property (e.g., particle concentration), t is the time, ρ is the density of air, x_i (i =1, 2, 3) is the three coordinates, $\bar{u}_i$ is the averaged air velocity component

in three directions, Γ is the effective particle diffusivity, S_c is the particle source term, D is the Brownian diffusivity of particles, and v_p is the particle turbulent diffusion coefficient.

Chang et al. (2007) noted that most previous CFD work on indoor particle transport is mainly based on the Eulerian advection-diffusion approach which takes less computing resources. However, this approach neglects the particulate nature of indoor particles and is only adequate for simulating gaseous pollutant or small, neutrally buoyant particles that exactly follow the fluid flow (Chang et al., 2007).

2.4.3.2 Eulerian-Lagrangian approach

In the Eulerian-Lagrangian approach, the fluid or carrier gas is considered as the continuum phase and the particles are considered as the discrete phase (Zhang, 2005). After the fluid flow field is resolved in the domain, a number of particles are then introduced into the domain at appropriate locations and the path of individual particles is tracked by solving the particle force balance (Hari, 2003). The interaction between the phases may or may not be present (Hari, 2003). The phases may be coupled to a different extent depending on the physical nature of the problem under consideration (Hari, 2003).

The Lagrangian method usually tracks a large quantity of particles transiently, where it first solves the transient momentum equation for each particle using the equation (Zhang and Chen, 2007; FLUENT, 2006):

$$\frac{du_p}{dt} = F_D(u - u_p) + \frac{g_x(\rho_p - \rho)}{\rho_p} + F_x \qquad (2.19)$$

where u, u_p, g_x, ρ_p, ρ, and F_x are the fluid phase velocity, particle velocity, gravitational acceleration, particle density, fluid density, and an additional acceleration (force/unit particle mass), respectively. F_D is the drag force per unit particle mass equal to:

$$F_D = \frac{18\mu}{\rho_p d_p^2} \frac{C_D Re}{24} \tag{2.20}$$

where μ, and Re are the molecular viscosity of the fluid and the relative Reynolds number, which is defined as:

$$Re \equiv \frac{\rho d_p \mid u_p - u \mid}{\mu} \tag{2.21}$$

If phases are separated and the density ratio is of order 1 or if the particle volume fraction is low (<10%), then a single-phase turbulence model such as the standard k-ε can be used to represent the mixture (FLUENT, 2006). The standard k-ε model is a semi-empirical model based on model transport equations for the turbulence kinetic energy (k) and its dissipation rate (ε). The model transport equation for k is derived from the exact equation, while the model transport equation for ε is obtained using physical reasoning and bears little resemblance to its mathematically exact counterpart. In the derivation of the k-ε model, the assumption is that the flow is fully turbulent, and the effects of molecular viscosity are negligible (FLUENT, 2006).

In FLUENT, the discrete phase model (DPM) follows the Eulerian-Lagrangian approach. Particle trajectories are computed individually at specified intervals during the fluid phase calculation. Each trajectory represents a group of particles of the same initial properties. Particle-to-particle interactions are neglected (Fluent, 2006). The use of DPM is limited to low volume fractions and this is the only multiphase model that allows specification of particle distribution or inclusion of combustion simulation. Turbulent dispersion in DPM can be modeled using either stochastic tracking or a "particle cloud" model (Fluent, 2006).

When the flow is turbulent, FLUENT will predict the trajectories of particles using the mean fluid phase velocity, $\bar{u}$, in the trajectory equation (2.19) . Optionally, the instantaneous

value of the fluctuating gas flow velocity, u'(t), can be included to predict the dispersion of the particles due to turbulence:

$$u = \bar{u} + u'(t) \tag{2.22}$$

In the stochastic tracking approach, FLUENT predicts the turbulent dispersion of particles by integrating the trajectory equations for individual particles, using the instantaneous fluid velocity along the particle path during the integration. By computing the trajectory in this manner for a sufficient number of representative particles, the random effects of turbulence on the particle dispersion maybe accounted for (Fluent, 2006).

Zhang and Chen (2007) compared the Eulerian-Eulerian and Eulerian-Lagrangian methods in predicting particle concentration distributions in ventilated spaces. Results showed that both methods predicted well the steady-state particle concentration distribution (Zhang and Chen, 2007). For the unsteady state condition, however, their result showed that the Eulerian-Lagrangian method performed better than the Eulerian-Eulerian method (Zhang and Chen, 2007). Loomans and Lamaire (2002) claimed that the Eulerian-Lagrangian method can be more precise than the Eulerian-Eulerian method in predicting particle distribution in a room, although they did not provide sufficient evidence with experimental validation. Riddle et al. (2004) also concluded that Eulerian-Lagrangian method gave better results than Eulerian-Eulerian method in predicting the dispersion of a gaseous pollutant around buildings.

2.4.4 Turbulence Model

The vast majority of natural and industrial flows are turbulent. Multiphase flows (i.e., two phase flows) are turbulent or at least "pseudo-turbulent." The CFD modeling of turbulence is advantageous because of lower turnaround time, lower cost, more flexibility, and occasionally

higher accuracy when compared to physical modeling (Kleinstreuer, 2003). The most common turbulence model, the k-ε model, has been used over three decades as the basis for turbulence flow computation (Crowe et al., 1996).

The turbulence kinetic energy, k, and its rate of dissipation, ε, are obtained from the following transport equations (Fluent, 2006):

$$\frac{\partial}{\partial t}(\rho k)+\frac{\partial}{\partial x_i}(\rho k u_i)=\frac{\partial}{\partial x_j}\left[\left(\mu+\frac{\mu_t}{\sigma_k}\right)\frac{\partial k}{\partial x_j}\right]+G_k+G_b+\rho\varepsilon+Y_M+S_k \tag{2.23}$$

$$\frac{\partial}{\partial t}(\rho \varepsilon)+\frac{\partial}{\partial x_i}(\rho \varepsilon u_i)=\frac{\partial}{\partial x_j}\left[\left(\mu+\frac{\mu_t}{\sigma_\varepsilon}\right)\frac{\partial \varepsilon}{\partial x_j}\right]+C_{1\varepsilon}\frac{\varepsilon}{k}(G_k+C_{3\varepsilon}G_b)-C_{2\varepsilon}\rho\frac{\varepsilon^2}{k}+S_\varepsilon \tag{2.24}$$

where G_k and G_b represent the generation of turbulence kinetic energy due to the mean velocity gradients and buoyancy, respectively; Y_M represents the contribution of the fluctuating dilatation in compressible turbulence to the overall dissipation rate; σ_k and σ_ε are the turbulent Prandtl numbers for k and ε, respectively; and S_k and S_ε are user-defined source terms.

The turbulent (or eddy) viscosity, μ_t, is computed by combining k and ε as follows (FLUENT, 2006):

$$\mu_t=\rho C_\mu\frac{k^2}{\varepsilon} \tag{2.25}$$

The model constants $C_{1\varepsilon}$, $C_{2\varepsilon}$, C_μ, σ_k and σ_ε have the following default values in FLUENT:

$$C_{1\varepsilon}=1.44,\ C_{2\varepsilon}=1.92;\ C_\mu=0.09;\ \sigma_k=1.0;\ \sigma_\varepsilon=1.3$$

Small particles tend to decrease the gas phase turbulence because they follow the turbulent fluctuations and add mass to the fluid. Large particles do not follow the gas phase

turbulent fluctuations and generate turbulence in the gas phase as a result of the instantaneous relative velocity between the particles and the gas (Elghobashi, 1991; Zhang, 2005).

2.4.6 Summary

Understanding of the particle-laden turbulent flow is important in solving indoor air quality problems and controlling particle dispersion. Limited data are available on dispersion and deposition of particles in indoor spaces. Numerical simulation using computational fluid dynamics can be used to study particle transport in rooms. There are two approaches to model two-phase flows: Eulerian-Eulerian and Eulerian-Lagrangian. The selection between the two is based on the research objective, the required computational resources/cost, and the characteristics of the problem under examination.

2.5 References

Alonso, M., A. Hernandez-Sierra, and I.J. Alquacil. 2003. Electrical charging of aerosol nanoparticles and some practical applications. *Revista de Mettalurgica*. Madrid: Centro Nacional de Investigaciones Metalurgicas.

Appleyard, P. G. 2006. Infrared extinction performance of high aspect ratio carbon nanoparticles. *Journal of Optics A-Pure and Applied Optics* 8(2): 101-113.

Appleyard, P. G. 2007. Modeled infrared extinction and attenuation performance of atmospherically disseminated high aspect ratio metal nanoparticles. *Journal of Optics A-Pure and Applied Optics* 9: 278-300.

Appleyard, P. G. and N. Davies. 2004a. Calculation and measurement of infrared mass extinction coefficients of selected ionic and partially ionic insulators and semiconductors: a guide for infrared obscuration applications. *Optical Engineering* 43(2): 376-386.

Appleyard, P. G. and N. Davies. 2004b. Modeling infrared extinction of high aspect ratio, highly conducting small particles. *Journal of Optics A-Pure and Applied Optics* 6(10): 977-990.

ASTM Standards. 1997. D 4470 – 97: Standard test methods for static electrification. Philadelphia, PA: ASTM.

Bailey, R. A., H. M. Clark, S. Krause, J. P. Ferris, and R. L. Strong. 2002. *Chemistry of the environment*. 2nd ed. San Diego, CA: Academic Press.

Banerjee, S. and S. Law. 1995. Characterization of chargeability of biological particulates by triboelectrification. *IEEE Transactions on Industry Applications* 34(6):1201-1205.

Baron P.A., M.K. Mazumder, and Y.S. Cheng. 2001. Direct-reading techniques using particle motion and optical detection. In *Aerosol measurement: principles, techniques, and applications*. P.A. Baron and K. Willeke, eds. New York, N.Y.: Wiley-Interscience.

Butler, B.A. 1998. Smoke and obscurant operations in a joint environment. Maxwell Air Force Base. AL. Unpublished Thesis.

Chang, T., H. Kao, and Y. Hsieh. 2007. Numerical study of the effect of ventilation pattern on coarse, fine, and very fine particulate matter removal in partitioned indoor environment. *Journal of the Air and Waste Management Association* 57:179-189.

Chen, D. and D. Pui, 1999. A high efficiency, high throughput unipolar aerosol charger for nanoparticles. *Journal of Nanoparticle Research* 1(1):115-126.

Cheng, Y.S., H.C. Yeh, and M.D. Allen. 1988. Dynamic shape factor of plate-like particles. *Aerosol Science and Technology* 8:109-123.

Colbeck, I., B. Atkinson, and Y. Johar. 1997. The morphology and optical properties of soot produced by different fuels. *Journal of Aerosol Science* 28(5): 715-723.

Colver, G. M. 1999. Chapter 3: Electrostatic measurements. In *Instrumentation for fluid-particle flow*, 47-83. S. L. Soo, ed. Norwich, N.Y.: William Andrew Inc.

Congrong, H., M. Lidia, and G. Dale. 2005. Particle deposition rate in residential houses. *Atmospheric Environment* 39(21):3891-3899.

Crowe, C.T. 1982. Review: Numerical models for dilute gas-particle flows. *Journal of Fluids Engineering* 104:297-303.

Crowe, C., M. Sommerfield, and Y.Tsuji. 1998. *Multiphase flows with droplets and particles*. Baca Raton, FL.: CRC Press.

Crowe, C.T., T.R. Troutt, and J.N. Chung. 1996. Numerical models for two-phase turbulent flows. *Annual Review of Fluid Mechanics* 28:11-43.

DeCarlo, P.F., J.G. Slowik, D.R. Worsnop, P. Davidovits, and J.L. Jimenez. 2004. Particle morphology and density characterization by combined mobility and aerodynamic diameter measurements. Part 1: Theory. *Aerosol Science and Technology* 38(12):1185-1205.

Dobbins, R. A., G. W. Mulholland, and N. P. Bryner. 1994. Comparison of a fractal smoke optics model with light extinction measurements. *Atmospheric Environment* 28(5):889-897.

Elghobashi, S.E. 1991. Particle-laden turbulent flows: Direct simulation and closure models. *Applied Science Research* 48:301-314.

Etheridge, D. and M. Sandberg. 1996. *Building ventilation: Theory and measurement*. Chichester, UK: Wiley.

Farmer, W. M. 1991. Prediction of broad-band attenuation computed using band-averaged mass extinction coefficients and band-averaged transmittance. *Optical Engineering* 30(9): 1255-1261.

Farmer, W. M. and K. L. Krist. 1981. Comparison of methods used to determine the mass extinction coefficient for phosphorous smokes. *Proceedings of the Society of Photo-Optical Instrumentation Engineers* 305: 7-16.

Farmer, W. M., F. A. Schwartz, R. D. Morris, M. A. Binkley, and L. M. Boyd. 1982. Optical characteristics at 3.4-um wavelength of munition-produced phosphorus smoke as a function of relative humidity. *Aerosol Science and Technology* 1(4): 409-425.

FLUENT. 2006. User's Guide. Lebanon, NH: Fluent, Inc.

Frese, K.W., Jr. 1979. Simple method for estimating energy levels of solids. *Journal of Vacuum Science and Technology* 16(4):1042-1044.

Friedlander, S. K. 2000. *Smoke, dust and haze: Fundamentals of aerosol dynamics*. 2nd ed. New York, N.Y.: Oxford University Press.

Friedlander, S.K. and D.Y.H. Pui. 2003. Emerging issues in nanoparticle aerosol science and technology. In *Workshop report sponsored by NSF, South California Particle Center, and UCLA*. Los Angeles, CA.

Gao, N. P. and J. L. Niu. 2007. Modeling the particle dispersion and deposition in indoor environments. *Atmospheric Environment* 41:3862-3876.

Haghighat, F., Z. Jiang, J.C. Y. Wang, and F. Allard. 1992. Air movement in buildings using computational fluid dynamics. *Transactions of ASME* 114:84-92.

Hand, J. L. and S.M. Kreidenweis. 2002. A new method for retrieving particle refractive index and effective density from aerosol size distribution data. *Aerosol Science and Technology* 36:1012-1026.

Hari, S. 2003. Computational fluid dynamics (CFD) simulations of dilute fluid-particle flows in aerosol concentrations. PhD diss. College Station, TX: Texas A&M University.

Higashima, Y. and K. Asano. 1998. Recent progress in electrostatic separation technology. *Particulate Science and Technology* 16:77-90.

Hinds, W. C. 1999. *Aerosol technology: Properties, behavior, and measurement of airborne particles*. 2nd ed. New York, N.Y.: John Wiley & Sons.

Holmberg, S and Y. Li. 1998. Modeling of the indoor environment – particle dispersion and deposition. *Indoor Air* 8:113-122.

Hutchison, K. D. and A. P. Cracknell. 2005. *Visible infrared imager radiometer suite: A new operational cloud imager*. New York, N.Y.: Taylor & Francis.

Jacobson, M. Z. 1999. *Fundamentals of atmospheric modeling*. UK: Cambridge University Press.

Jones, P.J. and G.E. Whittle. 1992. Computational fluid dynamics for building airflow for building air flow predictions – current status and capabilities. *Building and Environment* 27(30):321-338.

Khlystov, A., C. Stanier, and S. N. Pandis. 2004. An algorithm for combining electrical mobility and aerodynamic size distribution data when measuring ambient aerosol. *Aerosol Science and Technology* 38(S1): 229-238.

Kleber, W. and B. Makin. 1998. Triboelectric powder coating: A practical approach for industrial use. *Particulate Science and Technology* 16:43-53.

Kleinstreuer, C. 2003. *Two-phase flows: Theory and applications.* New York, N.Y.: Taylor and Francis.

Konecni, S., J. J. Whicker, and R. A. Martin. 2002. Computational modeling and experimental characterization of indoor aerosol transport. In *Proceedings of ASME FEDSM'02, ASME 2002 Fluids Engineering Division Summer Meeting*, 933-939. Quebec, Canada.

Ladouceur, H. D., A. P. Baronavski, and H. H. Nelson. 1997. Obscurants for infrared countermeasures. Washington, D.C.: Naval Research Lab.

Lai, A.C.K. 2004. Particle deposition indoors: A review. *Indoor Air* 12(4):211-224.

Li, X., P. Gilmour, K. Donaldson, and W. MacNee. 1996. Free radical activity and pro-inflammatory effects of particulate air pollution (PM10) in vivo and in vitro. *Thorax* 51(12):1216-1222.

Liberto, N. P. 1994. *Powder coating: The complete finisher's handbook*. Alexandria, VA: The Powder Coating Institute.

Liddament, M. W. 1991. A review of building air flow simulation. Technical Note AIVC33. Air Infiltration and Ventilation Center. Coventry, Great Britain: University of Warwick Science Park.

Loomans, M. and T. Lemaire. 2002. Particle concentration calculation using CFD – a comparison. In *Proceedings of Indoor Air*, 153-156. Edinburg, Scotland.

Loth, E. 2000. Numerical approaches for motion of dispersed particles, droplets and bubbles. *Progress in Energy and Combustion Science* 26:161-223.

Lowell, J. and A. R. Akande. 1988. Contact electrification – why is it variable? *Journal of Physics D: Applied Physics* 21(1):125-137

Lowell, J. and A.C. Rose-Innes. 1980. Contact electrification. *Advanced Physics* 29(6): 947-1023.

Makin, B. 1974. Physics and fundamentals of charged particles. *Physics Education* 9(6):389-393.

Matsuka, S. and H. Masuda. 2003. Electrostatics of particles. *Advanced Powder Technology* 14(2):143-166.

Mazumder, M. K., S. Banerjee, R. E. Ware, C. Mu, N. Kaya, and C. C. Huang. 1994. Characterization of tribocharging properties of powder paint. *IEEE Transactions on Industry Applications* 30(2): 365-369.

Mazumder, M. K., R. A. Sims, A. S. Biris, P. K. Srirama, D. Saini, C. U. Yurteri, S. Trigwell, S. De, and R. Sharma. 2006. Twenty-first century research needs in electrostatic processes applied to industry and medicine. *Chemical Engineering Science* 61:2192-2211.

Milham, M. 1976. A catalog of optical extinction data for various aerosols/smokes. ED-8P-770022-85. Aberdeen Proving Ground, MD: Edgewood Arsenal

Morawska, L., N.D. Bofinger, L. Kocis, and A. Nwankwoala. 1998. Submicrometer and supermicrometer particles from diesel vehicle emissions. *Environmental Science and Technology* 32(14):2033-2042.

Murtomaa, M. 2002. Electrostatic studies on pharmaceutical powders and aerosols. Thesis. Turku, Finland: University of Turku

Myrdal, P.B., S. W. Stein, E. Mogalian, W. Hoye, and A. Gupta. 2004. Comparison of the TSI model 3306 impactor inlet with the Andersen cascade impactor: solution metered dose inhalers. *Drug development and Industrial Pharmacy* 30(8):859-868.

Oberdorster, G., J. Ferin, and B. Lehnert. 1994. Correlation between particle size, in vivo particles persistence, and lung injury. *Environmental Health Perspectives* 102 (Suppl. 5): 173-179.

Owrutsky, J. C., H. H. Nelson, H. D. Ladouceur, and A. P. Baronavski. 2000. Obscurants for infrared countermeasures II. Washington, D.C.: Naval Research Lab.

Owrutsky, J. C., D. A. Steinhurst, H. D. Ladouceur, H. H. Nelson, and A. P. Baronavski. 2001. Obscurants for infrared countermeasures III. Washington, D.C.: Naval Research Lab.

Peters, T. M., C. HungMin, D. A. Lundgren, and P. B. Keady. 1993. Comparison and combination of aerosol size distributions measured with a low pressure impactor, differential mobility particle sizer, electrical aerosol analyzer, and aerodynamic particle sizer. *Aerosol Science and Technology* 19: 396-405.

Peters, T. M., D. Ott, and P.T. O'Shaughnessy. 2006. Comparison of the Grimm 1.108 and 1.109 Portable Aerosol Spectrometer to the TSI 3321 Aerodynamic Particle Sizer for dry particles. *Annals of Occupational Hygiene* 50(8):843-850

Pomeroy, N., D. Webber, and C. Murphy. 2000. Monitoring of particle mass and number in urban air. *Environmental Monitoring and Assessment* 65(1-2):175-180.

Powers, K.W., M. Palazuelos, B.M. Moudgil, and S.M. Roberts. 2007. Characterization of the size, shape, and state of dispersion of nanoparticles for toxicological studies. *Nanotoxicology* 1(1):42-51

Plowman, R. 1995. Electrostatic discharge: A review. In *The Institution of Electrical Engineers, IEE Colloquim on ESD (Electrostatic Discharge) and ESD Counter Measures*. London, UK.

Riddle, A., D. Carruthers, A. Sharpe, C. McHugh, and J. Stocker. 2004. Comparisons between FLUENT and ADMS for atmospheric dispersion modeling. *Atmospheric Environment* 38:1029-1038.

Schnurmann, R. 1941. Contact electrification of solid particles. *Proceedings of the Physical Society* 53:547-553.

Seaton, A., W. MacNee, K. Donalson, and D. Godden. 1995. Particulate air pollution and acute health effects. *Lancet* 345(8943):176-178.

Sharma, R., S. Trigwell, S., R.A. Sims, and M.K. Mazumder. 2004. Modification of electrostatic properties of polymer powders using atmospheric plasma reactor. In *Polymer Surface Modification: Relevance to Adhesion*, Vol. 3, 25. Mittal, K.L. ed. VSP, AH. Zeist, The Netherlands.

Shen, S., P. Jacques, Y. Zhu, M. Geller, and C. Sioutas. 2002. Evaluation of the SMPS-APS system as a continuous monitor for measuring the $PM_{2.5}$, PM_{10} and coarse ($PM_{2.5-10}$) concentrations. *Atmospheric Environment* 36(24):3939-3950.

Shi, J. M., L. L. Chen, Y. S. Ling, and Y. Lu. 1998. Infrared extinction of artificial aerosols and the effects of size distributions. *International Journal of Infrared and Millimeter Waves* 19(12): 1671-1679.

Shi, J.P., R.M. Harrison, and D. Evans. 2001. Comparison of ambient particle surface area measurement by epiphaniometer and SMPS/APS. *Atmospheric Environment* 35:6193-6200.

Shi, J. M., J. Y. Wang, B. Xu, J. C. Wang, and Z. C. Yuan. 2003. Calculation and optimization of the effective extinction cross section of the spherical cold obscuring smoke. *International Journal of Infrared and Millimeter Waves* 24(11): 2007-2013.

Singh, A., S. G. Avachat, and H. Singh. 1994. Infrared screening smokes - a review. *Journal of Scientific & Industrial Research* 53(9): 667-673.

Sioutas, C., E. Abt. J.M. Wolfson, and P. Koutrakis. 1999. Evaluation of the measurement performance of the scanning mobility particle sizer and aerodynamic particle sizer. *Aerosol Science and Technology* 30(1):84-92

Smith, B.C. 1996. *Fundamentals of fourier transform infrared spectroscopy*. Boca Raton, FL: CRC Press.

Stein, S.W., P.B. Myrdal, B.J. Gabrio, D. Obereit, and T.J. Beck. 2003. Evaluation of a new Aerodynamic Particle Sizer® spectrometer for size distribution measurements of solution metered dose inhalers. *Journal of Aerosol Medicine-Deposition Clearance and Effects in the Lung* 16(2):107-119

Stuart, B. 2004. *Infrared spectroscopy: Fundamentals and applications*. Chichester, England: J. Wiley and Sons, Ltd.

Tianxiang, L. 1999. An experiment study of particle charge and charge exchange related to triboelectric beneficiation. PhD diss. Lexington, KY: University of Kentucky.

Trigwell, S., N. Grable, C.U. Yurteri, R. Sharma and M.K. Mazumder. 2003. Effects of surface properties on the tribocharging characteristics of polymer powder as applied to industrial processes. *IEEE Transactions of Industry Applications* 39(1):79-86.

Wang, J. Y., J. M. Shi, B. Xu, J. C. Wang, and Z. C. Yuan. 2004. Calculation of overall effective extinction cross section of several cold smoke infrared ammunitions. *Defense Science Journal* 54(3): 329-334.

Widmann, J. F., J. Duchez, J. C. Yang, J. M. Conny, and G. W. Mulholland. 2005. Measurement of the optical extinction coefficient of combustion-generated aerosol. *Journal of Aerosol Science* 36(2): 283-289.

Widmann, J. F., J. C. Yang, T. J. Smith, S. L. Manzello, and G. W. Mulholland. 2003. Measurement of the optical extinction coefficients of post-flame soot in the infrared. *Combustion and Flame* 134(1-2): 119-129.

Zhang, J. Z. 2003. Dynamic properties of nanoparticles. In *Handbook of Nanophase and Nanostructured Materials, Volume 2: Characterization*, 219-251. Z.L. Wang, Y. Liu and Z. Zhang, ed. Tsinghua University Press: Kluwer Academic/Plenum Publishers.

Zhang, N. 2005. Motion and distribution of micro-sized solid particles in turbulent gas flow. PhD diss. Manhattan, KS: Kansas State University.

Zhang, Z. and Q. Chen. 2007. Comparison of the Eulerian and Lagrangian methods for predicting particle transport in enclosed spaces. *Atmospheric Environment* 41:5236-5248.

3. Size Distribution and Concentration of Aerosolized Nanostructured Particles

3.1 Abstract

Metal oxide nanostructured particles have been shown to be effective in inactivating a wide variety of chemical warfare agents, biological agents, and toxic industrial chemicals, and in detoxification of indoor spaces. Such applications may require aerosolization of these metal oxide nanomaterials into the affected space to scavenge unwanted entities. To be effective, the particles must be deployed with the desired particle size distribution, concentration, and sufficient coverage distribution over the affected space. This research was conducted to characterize two metal oxide nanostructured particles (i.e., NanoActive® MgO and NanoActive® MgO plus), which differed in terms of size of the primary particle and specific surface area. Each metal oxide material was aerosolized and dispersed into an enclosed chamber (3.6 m x 2.4 m x 2.4 m) using a pressurized canister. The size distribution and number concentration of the particles inside the chamber were monitored with a Scanning Mobility Particle Sizer® (SMPS) spectrometer and an Aerodynamic Particle Sizer® (APS) spectrometer. A Tapered Element Oscillating Microbalance® (TEOM) was also used to monitor particle mass concentration. The effect of canister pressure (40 vs. 80 psig) and nominal mass (50 vs. 20 g) on NanoActive® MgO plus was also investigated. Results showed that the two particles differed significantly in particle size distribution. Compared to the NanoActive® MgO plus, the NanoActive® MgO had higher number concentration of the smaller particles (<6 μm) and smaller number concentration of the larger particles (>6 μm). In addition, the NanoActive® MgO had a mean geometric mean diameter (GMD) of 3.12 μm (s.d. = 1.30 μm) while

NanoActive® MgO plus had mean GMD of 11.1 μm (s.d. = 0.68 μm). NanoActive® MgO had higher GSD value (2.85, s.d. = 0.32) than NanoActive® MgO plus (1.70, s.d. = 0.061). The deployment pressure (80 vs. 40 psig) had little influence on the amount deployed and percent deployed of NanoActive® MgO plus. Decreasing the nominal amount of NanoActive® MgO plus from 50 to 20 g, also decreased the mean percent deployed from 80% to 67%, but these values were not significantly different.

3.2 Introduction

Metal oxide nanostructured particles, because of their high surface area, unique morphology, and reactivity have been shown to be effective in inactivating a wide variety of chemical warfare agents, biological agents, and toxic industrial chemicals, and in detoxification of indoor spaces (Wagner et al., 1999; Carnes and Klabunde, 2002; Decker et al., 2002; Koper et al., 2002). Some metal oxide nanostructured particles also have been found to be effective in clearing aerosol-type smokes in enclosed spaces (Yadav et al., 2007; Zhang et al., 2007). They can be used for mitigation of the hazards posed by aerosols or contaminated surfaces. Furthermore, they have a long shelf life and do not require water or mixing. Koper et al. (2002) also noted that the particles are converted to harmless common minerals after several days' exposure to the atmosphere.

The above applications may involve aerosolization of the nanostructured particles into the affected space to scavenge unwanted particles and/or gaseous contaminants. To be effective, the nanostructured particles must be deployed with the desired particle size distribution, concentration, and sufficient coverage distribution over the affected space (Kakumanu, 2005; Braley, 2005). It is therefore necessary to characterize the dispersion and behavior of nanostructured particles dispersed in air.

Characterization of nanostructured materials is also needed for toxicological purposes. Short-term changes in particle concentration by size appear to be related to some adverse health effects. Thus, assessment of potential particle exposure requires instruments that provide rapid physical characterization (Peters et al., 2006).

Limited research has been conducted to characterize the particle size distribution of nanostructured particles. Jillavenkatesa and Kelly (2002) noted that there is a need to characterize dispersed nanopowders and their state of agglomeration. Most of the characterization studies for toxicological and epidemiological studies have used the Scanning Electron Microscopes (SEM) and Atomic Force Microscopes (AFM) (Wang et al., 2003), which require that the particles have to be collected on appropriate substrates.

Kakumanu (2005) characterized aerosolized nanostructured particles and a conventional material. A cascade impactor, Tapered Element Oscillating Microbalance (TEOM), respirable dust cyclone, and sedimentation plates were used to measure aerodynamic particle size distribution, mass concentration, respirable mass concentration, and particle deposition, respectively.

This research was conducted to characterize two metal oxide nanostructured particles, NanoActive® MgO plus and NanoActive® MgO, using real-time instruments. The two particles have similar chemical composition, but differed in primary particle size and specific surface area. They also differed in their effectiveness in clearing smoke in enclosed spaces (Yadav et al., 2008). Specific objectives were to:

1. measure the size distribution, number and mass concentrations, and geometric mean diameter (GMD) of aerosolized nanostructured particles; and

2. determine the effect of dispersion pressures and particle mass dispersed on particle size distribution and concentration.

3.3 Materials and Methods

3.3.1 Experimental set-up and instrumentation

All experiments were conducted inside an experimental chamber (3.6 m x 2.4 m x 2.4 m) (Fig. 3.1). The chamber was equipped with a HEPA filtration system and instrumented with particle measuring instruments, including an Aerodynamic Particle Sizer® (APS) spectrometer (Model 3321, TSI, Inc., Shoreview, MN)) with a diluter (Model 2202A, TSI, Inc., Shoreview, MN), Scanning Mobility Particle Sizer® (SMPS) spectrometer (Model 3936, TSI, Inc., Shoreview, MN), Tapered Element Oscillating Microbalance® (TEOM) (Model 1400a, Thermo-Fisher Scientific, Inc., Waltham, MA), and filter samplers.

The APS spectrometer measures the equivalent aerodynamic diameter (d_a) of particles from 0.5 to 20 μm using the time-of-flight technique. In this technique, the d_a of a particle is measured based on its velocity immediately downstream of a flow-accelerating nozzle. As the particle passes through overlapping beams, it generates one signal with two crests; the time between the crests is used to determine d_a (TSI, 2005a; 2005b). In this study, the APS was configured to sample the aerosol at 1 L/min (sheath flow rate of 4 L/min) every 2 min.

The SMPS spectrometer measures the equivalent mobility diameter (d_{me}) of a particle. It consists of an electrostatic classifier, with a long differential mobility analyzer (LDMA), and an ultrafine condensation particle counter (UCPC). It operates in the range of approximately 10 nm to 1000 nm mobility diameter. The aerosol sample first passes through an inertial impactor to remove large particles (>1000 nm mobility diameter) and then through a radioactive charger in the electrostatic classifier. The radioactive charger imparts bipolar equilibrium charge levels to

the particles. The charged aerosol then enters the tube of the LDMA in which particles are selected according to their electrical mobility (Morawska et al., 1998; TSI, 2005c; TSI, 2005d). The effective particle size range settings of the SMPS can be modified by varying the sample aerosol and sheath air flow rates and the voltage setting of the electrostatic classifier. For this study, a sample aerosol airflow rate of 0.2 L/min, sheath airflow rate of 2 L/min, and voltage range of 10-9845 V were used. These settings gave a d_{me} range of 19.1 to 898 nm, which adequately covered the number distribution of the nanostructured particles used. The SMPS was configured to have a scan-up time of 2 min that provides an adequate accuracy for SMPS. For example, the use of shorter scan time (e.g., 30 sec) is applicable to an aerosol that changes substantially during sampling while longer scan time is used if higher particle size accuracy is desired (TSI, 2005c; Tokonami and Knutson, 2000).

The TEOM was used to measure particle mass concentration. The natural frequency of a tapered element inside the instrument's mass transducer depends on its mass and the change in frequency is proportional to the particulate mass collected. The TEOM was operated with an air sampling flow rate of 16.7 L/min and a sampling interval of 1 min. It was equipped with an inlet for total suspended particulates ($da \leq 30$ μm).

Two filter samplers were used to collect particles on pre-weighed filters. The samplers, with an air sampling flow rate of 2 L/min each, were operated for 1 min immediately after the dispersion of the particles. The mass of particles was determined by weighing the filters on a microbalance with a sensitivity of 0.01 mg.

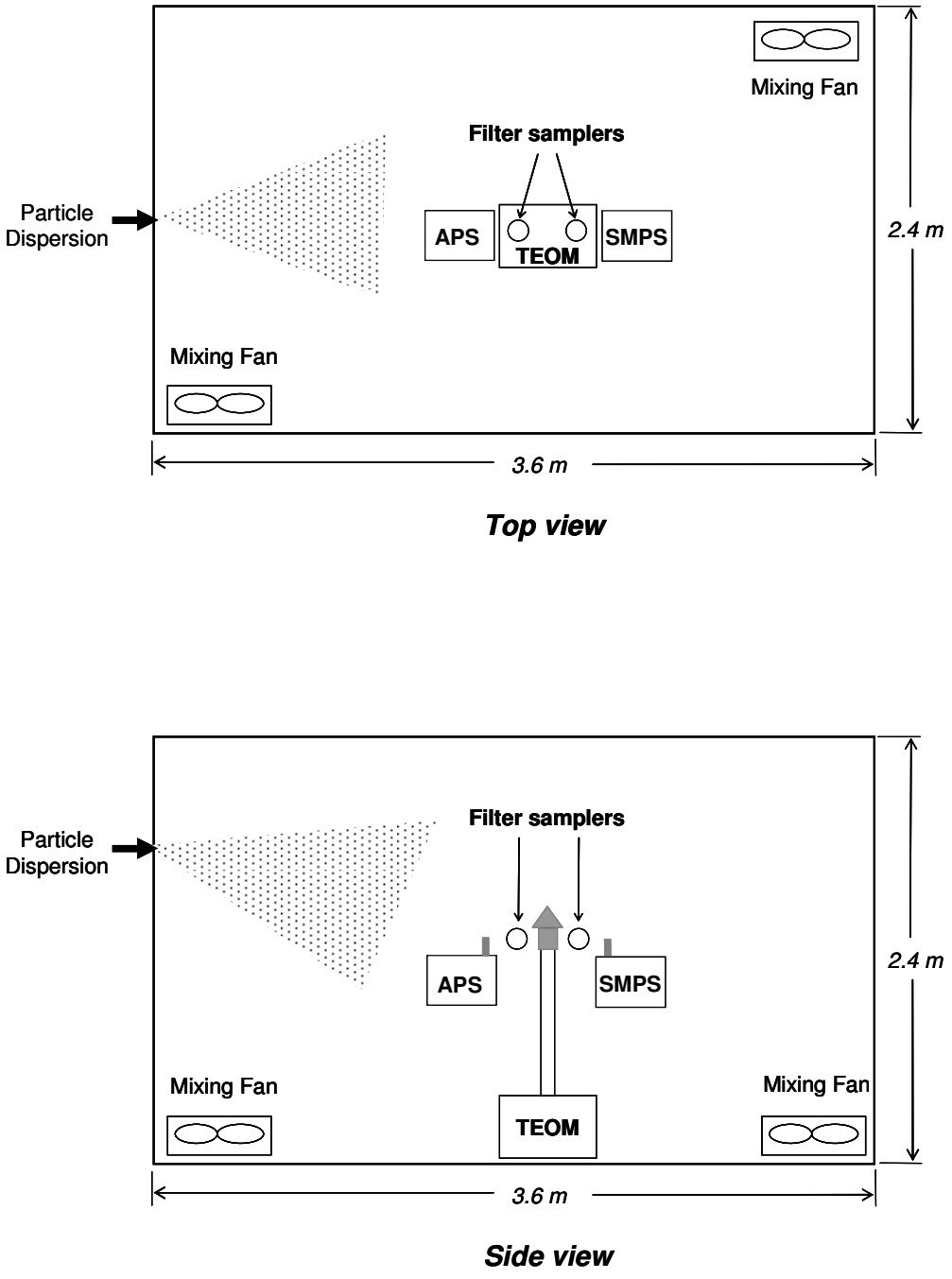

Figure 3.1. Schematic diagram of the experimental chamber showing the instruments: Aerodynamic Particle Sizer® (APS) Spectrometer, Scanning Mobility Particle Sizer ® (SMPS) spectrometer, Tapered Element Oscillating Microbalance® (TEOM), and filter samplers.

3.3.2 Experimental procedure

This study considered two metal oxide nanostructured products: NanoActive® MgO and NanoActive® MgO plus, herein referred to as NA MgO and NA MgO plus (Fig. 3.2), respectively. The two materials were purchased from NanoScale Corporation (Manhattan, KS). They have high surface areas and unique crystal morphologies with numerous edges/corners and other reactive sites. The two particles differed in specific surface area, individual crystallite size, and true density (Table 3.1). The specific surface areas of NA MgO plus and NA MgO were approximately 600 m^2/g and 230 m^2/g, respectively; the individual crystallite sizes were <4 nm and 8 nm, respectively (NanoScale Corporation, 2004a; 2004b). Using a multipycnometer, the true densities of NA MgO plus and NA MgO were 2.42 g/cc and 3.24 g/cc, respectively (Table 3.1). The two particles also differed in their ability to clear smoke in enclosed spaces. Yadav et al. (2008) reported that NA MgO plus was considerably more effective than NA MgO in clearing glycol smoke in an enclosed space.

The study also considered the effects of nominal mass and dispersion pressure for NA MgO plus. Table 3.2 summarizes the experiments conducted. For each experiment, there were three replicates.

Experiments involved cleaning the experimental chamber by thoroughly vacuuming the floor and the walls and running its HEPA filtration system for at least 30 min to remove any unwanted particles. The "clean" chamber had number concentrations of less than 500 and 10 particles/cm^3 using SMPS and APS, respectively.

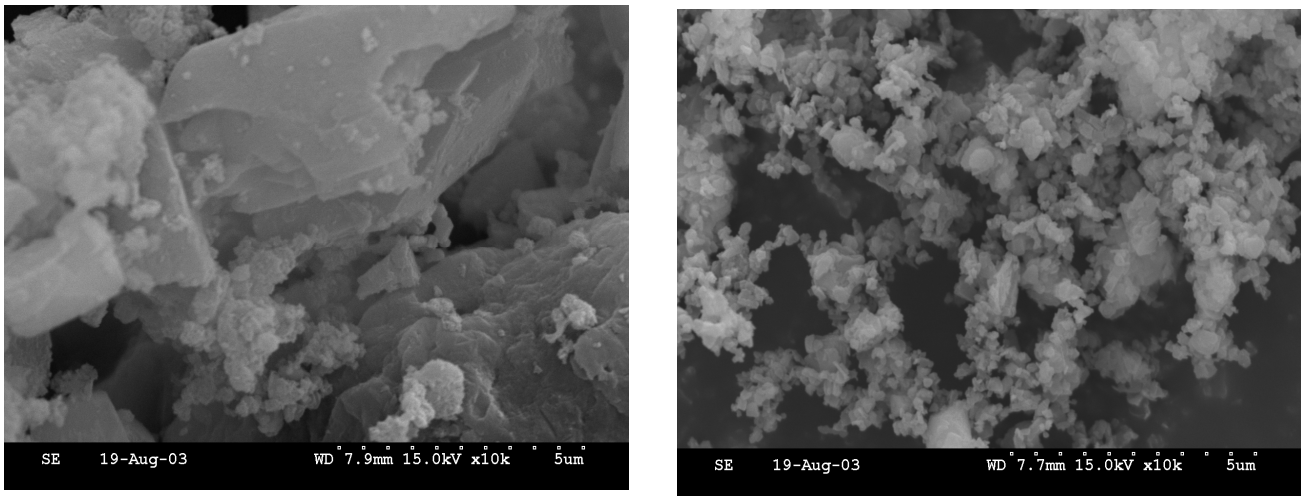

(a) (b)

Figure 3.2 Scanning electron micrographs: (a) NA MgO plus and (b) NA MgO particles.

Table 3.1. Properties of the two nanostructured particles.

Particles	Specific surface area[a], m^2/g	Crystal size[a], nm	Bulk density[a], g/cc	True density[b], g/cc	Mean aggregate size[a], nm	t^*_{10}[c]
NanoActive® MgO	> 230	8	0.6	3.24	3,300	0.38
NanoActive® MgO plus	> 600	< 4	0.4	2.42	12,000	0.10

[a]Source: Nanoscale Corp., Manhattan, KS.

[b]Measured with a multipycnometer at Kansas State University, Manhattan, KS.

[c]Source: Yadav (2005). The t^*_{10} value represents the smoke-clearing effectiveness of a material. Small values of t_{10}* indicate effective smoke clearing.

The SMPS, APS, and TEOM were operated for at least 10 min before dispersing the particles inside the chamber. The two mixing fans inside the chamber were also first turned on before dispersion to allow mixing of particles. Particles were dispersed into the chamber using a pressurized canister. Once the particles were dispersed, the fans were turned off.

Table 3.2. Summary of experimental design. There were three replicates for each experiment.

Nanostructured Particle	Nominal amount, g	Dispersion pressure, psig
NanoActive® MgO	50	80
NanoActive® MgO plus	50	80
NanoActive® MgO plus	20	80
NanoActive® MgO plus	50	40

3.3.3 Data analysis

3.3.3.1 Conversion from number concentration to mass concentration

The SMPS and APS were operated using the Aerosol Instrument Management (AIM) software (TSI, Inc., Shoreview, MN) to obtain the number concentration, C_n, of particles. The AIM software was also used to calculate the mass concentration, C_m, from the C_n values using the equation:

$$C_m = \frac{\pi}{6}\rho_p C_n \left(\frac{d_p}{\sqrt{\rho_p}}\right)^3 \qquad (3.1)$$

where ρ_p and d_p are particle density and diameter, respectively. The diameter used for calculations was the logarithmic midpoint (geometric mean) of the bin boundaries (Congrong et al., 2005; TSI, 2005c). In converting from number-based to mass-based diameter, particle densities used were 2.42 g/cm^3 and 3.24 g/cm^3 for NA MgO plus and NA MgO, respectively (Table 3.1).

The AIM software also has the data correction for multiple charges and coincidence incurred in using the SMPS and APS, respectively. Multiple charges occur when particles with multiple charges are counted as if they only have one charge and thus, classified as being smaller

than their actual particle diameter. Coincidence occurs when particles are erroneously counted by the detector of the instrument (Sioutas et al., 1999; Heitbrink et al., 1991; TSI, 2005c).

3.3.3.2 Conversion of mobility diameter to aerodynamic diameter

The Data Merge software module (Model 390069, TSI, Inc., Shoreview, MN) was used to convert $d_{me,}$ measured by the SMPS to d_a measured by the APS using the following equation (Hinds, 1999):

$$\sqrt{C_a d_a} = \sqrt{\frac{C_{me}\rho_p}{\chi\rho_o}} d_{me} \tag{3.2}$$

where C_a, C_{me}, χ, and ρ_o are the slip correction factor for d_a, slip correction factor for d_{me}, dynamic shape factor, and unit density (1 g/cm^3), respectively. In this study, particles were assumed to be perfect spheres, i.e., χ=1. The slip correction factor, C (C_a or C_{me}), was calculated using the following equation (Hinds, 1999):

$$C = 1 + \frac{2\lambda_p}{d_p}\left(1.142 + 0.558e^{\frac{-0.999 d_p}{2\lambda_p}}\right) \tag{3.3}$$

where λ_p is the mean free path (6.65 x 10^{-8} m) and d_p is the particle diameter (d_a or d_{me}).

3.3.3.3 Merging of SMPS and APS data

The Data Merge software module was also used to merge and fit the SMPS and APS data files into one combined or composite size distribution. The software also calculates a "goodness of fit" parameter that represents the average difference between the fitted size distribution and the data. As the value of the goodness of fit approaches 0, the better is the fit.

3.3.3.4 Particulate matter

The PM_4 or particulate matter with aerodynamic diameter of 4 μm or less was also obtained from the mass concentration data using APS and SMPS. The PM_4 concentration provides information on respirable dust that could reach the human lungs.

3.3.3.5 Statistical Analysis

Data were analyzed statistically using SAS (version 9.1, SAS Institute Inc., Cary, NC). The PROC GLM procedure was used to determine the effects of type of particle, dispersion pressure, and nominal amount on size distribution and concentration. The Tukey's Multiple Comparison Method was used to compare the means at $\alpha = 0.05$.

3.4 Results and Discussion

3.4.1 Particle Deployment

The two particles, with the same nominal mass (50 g) and canister pressure (80 psig), differed greatly in terms of the mass deployed and percent deployed. With NA MgO plus, the mass deployed was 40 g (80%, s.d.= 0.12%); with NA MgO, on the other hand, the mass deployed was only 11 g (22%, s.d.=1.6%) (Fig. 3.3). Similar observation was reported by Yadav et al. (2008). This implies that in dispersing nanostructured particles (i.e., NA MgO), special attention must be given to the aerosolization method, nominal amount, and deployment pressure to attain the desired concentration.

The deployment pressures (80 vs. 40 psig) had little influence on the amount deployed and percent deployed for NA MgO plus (Fig. 3.4). With a canister pressure of 40 psig and a nominal mass of 50 g, the mean value of percent deployed was 73% (s.d.=7.21%). This was smaller but not significantly different from the mean percent deployed of 80% obtained from using a canister pressure of 80 psig and a nominal mass of 50 g.

The percent deployed for NA MgO plus was also not significantly affected by the nominal mass. Decreasing the nominal amount for NA MgO plus from 50 to 20 g also decreased the mean percent deployed from 80% (40 g) to 67% (13 g), but the values were not significantly different (Fig. 3.5).

3.4.2 Particle size distribution (PSD)

The PSDs of NA MgO and NA MgO plus are shown in Figures 3.6 and 3.7, respectively. The merged SMPS-APS data for NA MgO and NA MgO plus had goodness of fit values of 0.030 and 0.038, respectively, indicating relatively good fit of data from the two instruments. By merging the PSD, however, underestimation of SMPS data and overestimation of APS data could be observed..

The advantage of merged PSD is that it could give a good estimate of a wider size distribution of particles. As shown in Figure 3.8, the two particles differed significantly in merged PSD. The SMPS data showed that NA MgO had higher number concentration of small particles (<1000 nm) than NA MgO plus. The APS data also confirmed that the NA MgO had higher number concentration of the smaller particles (<6 µm), and smaller number concentration of the larger particles (>6 µm) than Na MgO plus.

Figure 3.9 shows the merged PSD of NA MgO plus for various nominal amounts and dispersion pressures. As expected, the higher the mass dispersed (40 g), the higher was the number concentration of particles. The canister pressure seemed to affect the size distribution of the NA MgO plus, especially the smaller particles. Use of higher pressure (80 psig) showed higher number of submicrometer particles, possibly due to more deagglomeration of particles with 80 psig pressure.

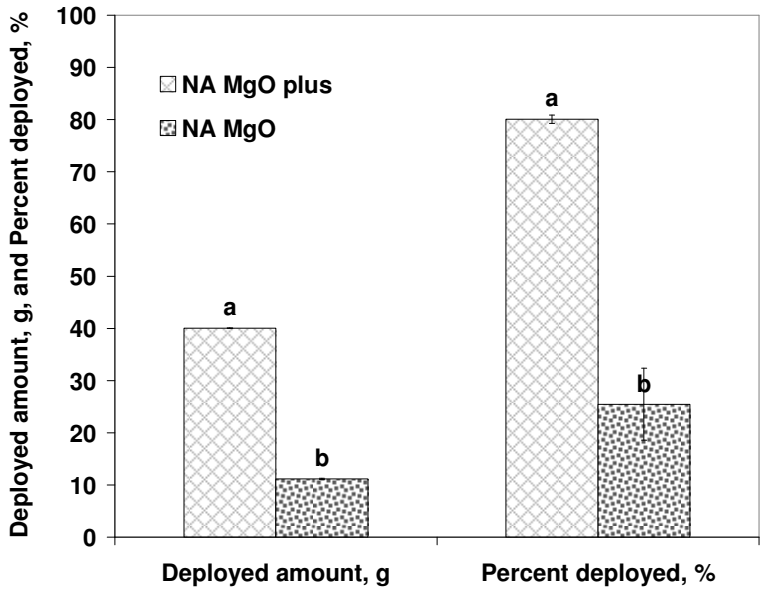

Figure 3.3. Comparison of the two particles in deployed amount (g) and percent deployed. Bars with the same letters are not significantly different at the 5% level. Error bars represent mean of three replicates.

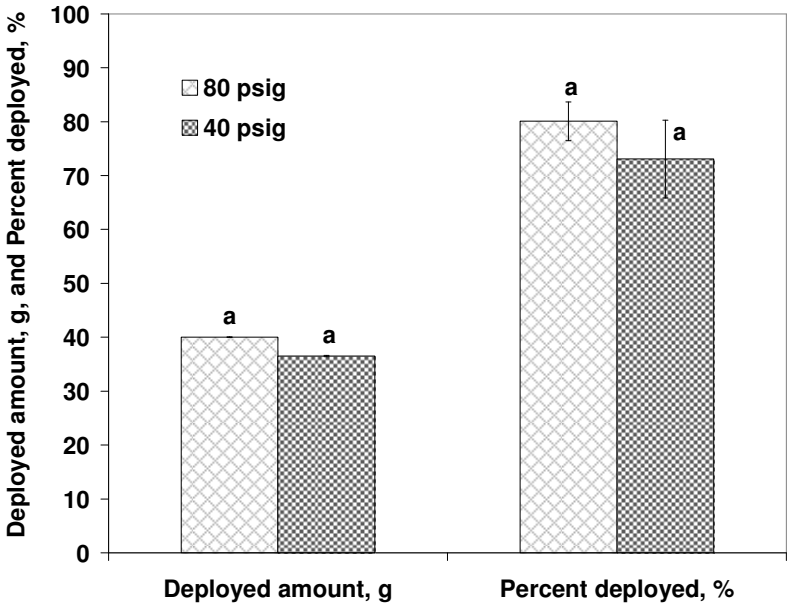

Figure 3.4. Effect of dispersion pressure (80 vs. 40 psig) on the deployed amount (g) and percent deployed of NA MgO plus. Bars with the same letters are not significantly different at the 5% level. Error bars represent mean of three replicates.

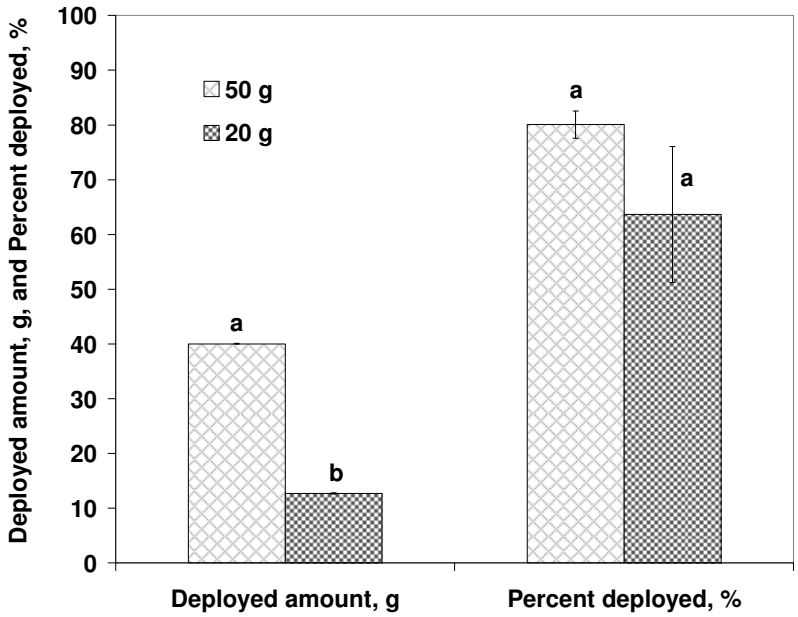

Figure 3.5. Effect of nominal amount (50 vs. 20 g) on the percent deployed of NA MgO plus. Bars with the same letters are not significantly different at the 5% level. Error bars represent mean of three replicates.

The temporal variation in the particle size distribution (number and mass concentrations) of NA MgO and NA MgO plus are shown in Figures 3.10-3.13. Generally, these plots show the bias of number concentration to smaller particles, and the bias of mass concentration to larger particles.

3.4.3 Geometric mean diameter (GMD)

The GMD and GSD values of the two nanostructured particles at time 2 min after dispersion are shown in Tables 3.3 and 3.4, respectively. The GMD and GSD values of NA MgO plus did not significantly change with the nominal amount and pressure used. Using the SMPS, NA MgO showed higher GMD (mass-based) value of 1087 nm (s.d. = 5) compared with NA MgO plus, which had GMD ranging from 894 nm (s.d. = 24) to 920 nm (s.d. = 27) (Table 3.3). From the APS data, the NA MgO plus, had higher GMD values ranging from 10.5 μm

(s.d. = 1.23 μm) to 11.3 μm (s.d. = 0.28 μm) while NA MgO had lower GMD of 4.19 μm (s.d. =0.98 μm). From the merged data, NA MgO had a GMD of 3.12 μm (s.d. = 1.30 μm) while NA MgO plus had GMD values ranging from 10.6 μm (s.d. = 1.17 μm) to 11.6 μm (s.d. = 0.33 μm), with mean value of 11.1 μm (s.d. = 0.49 μm). These GMD values were slightly lower than the mean aggregate sizes that were specified by the manufacturer (Table 3.1). Comparing the GSD values, NA MgO had higher GSD (2.85, s.d. = 0.32) than NA MgO plus (Table 3.4) which had GSD values ranging from 1.68 (s.d. = 0.087) to 1.74 (s.d. = 0.080).

The change in GMD with time is shown in Figure 3.14. The SMPS data showed that both particles have GMD of less than 1000 nm that stayed nearly constant and did not change much with time (Fig. 3.14a). From the APS data, NA MgO plus had faster decay in GMD than NA MgO. This is possibly due to the size dependence of particle decay wherein bigger particles settle faster (Fig. 3.14b).

3.4.4 Decay in number and mass concentrations

The decay in number concentration of NA MgO plus and NA MgO is shown in Figure 3.15. Overall, NA MgO showed greater number concentration than NA MgO plus, in both SMPS and APS measurements probably due to its smaller mean diameter. Higher variability of number concentration values was observed in measurement using the SMPS compared to APS. NA MgO showed steeper slope than NA MgO plus (Fig. 3.14a) probably due to higher particle density of NA MgO (3.24 g/cm^3) than NA MgO plus (2.42 g/cm^3). A significant fraction of particles remained suspended in air even 60 min after dispersion. At t=60 min, NA MgO had number concentrations of 22,687 (s.d. = 12,968) and 61,133 (s.d.= 7,715) particles/cm^3 using SMPS and APS, respectively; NA MgO plus had 9,356 (s.d. = 11,781) and 4,483 (s.d. = 715) particles/cm^3 using SMPS and APS, respectively. It should be noted that the initial number

concentration inside the chamber before dispersion of particles was <500 and <10 particles/cm^3 for SMPS and APS, respectively. Figure 3.16 shows the decay in mass concentration of NA MgO plus and NA MgO using the SMPS and APS. The mass concentration of NA MgO from the SMPS data showed higher values due to its large number of smaller particles (Fig. 3.16a). NA MgO plus showed higher mass concentration in the first 10 min from the APS data that shows a steep slope implying a faster mass concentration decay (Fig. 3.16b). The mass concentration obtained from SMPS also represents the PM_4 values of the two nanostructured particles since the size range measured was below 1 μm. The PM_4 values from the APS are shown in Figure 3.17. NA MgO had higher PM_4 value of 19.2 mg/m^3 (s.d. = 3.76) at t = 2 min after dispersion relative to NA MgO plus (8.55 mg/m^3, s.d. = 3.80). At t = 60 min, the PM_4 values of NA MgO and NA MgO plus were 6.19 mg/m^3 (s.d. = 1.48) and 1.01 mg/m^3 (s.d. = 0.20), respectively. The threshold limit value for time weighed average (TLV-TWA) for respirable dust is 5 mg/m^3 exposure concentration for normal 8 to 10 h workday (ACGIH, 1993).

The mass concentration measured by TEOM, which includes particles size range up to 30 μm, is shown in Figure 3.18. NA MgO plus has a steeper slope compared to NA MgO. The mass concentration measured by the APS and SMPS (Fig. 3.16) were considerably smaller than those measured by TEOM. This could be due to the difference in the particle diameter range that each instrument could measure. The three instruments did show similar trend/decay. Figure 3.19 compares the mass concentrations from TEOM and filter samplers measured 1 min after the dispersion. The TEOM and filter samplers did not differ significantly in measured concentration.

3.5 Conclusion

This research was conducted to measure the size distribution and concentration of two nanostructured materials, which differed in primary particle size, surface area, and effectiveness in clearing smoke in enclosed spaces. The following conclusions were drawn from this research:

1. The two particles differed significantly in particle size distribution. The SMPS and APS data showed that NA MgO had higher number concentration of small particles (<1000 nm) than NA MgO plus. From the merged data, the NA MgO had a mean GMD of 3.12 µm (s.d. = 1304) while the NA MgO plus had mean value of 11.1µm (s.d. = 675).
2. The SMPS data showed that both particles have GMD of less than 1000 nm that stayed nearly constant and did not change much with time. From the APS data, NA MgO plus had faster decay in GMD than NA MgO. This is possibly due to the size dependence of particle decay wherein bigger particles settle faster.
3. A significant fraction of each product stayed long in air even 60 min after dispersion.
4. For NA MgO plus, the nominal amount (50 vs. 20 g) and deployment pressures (80 vs. 40 psig) had little influence on the percent deployed and size distribution.

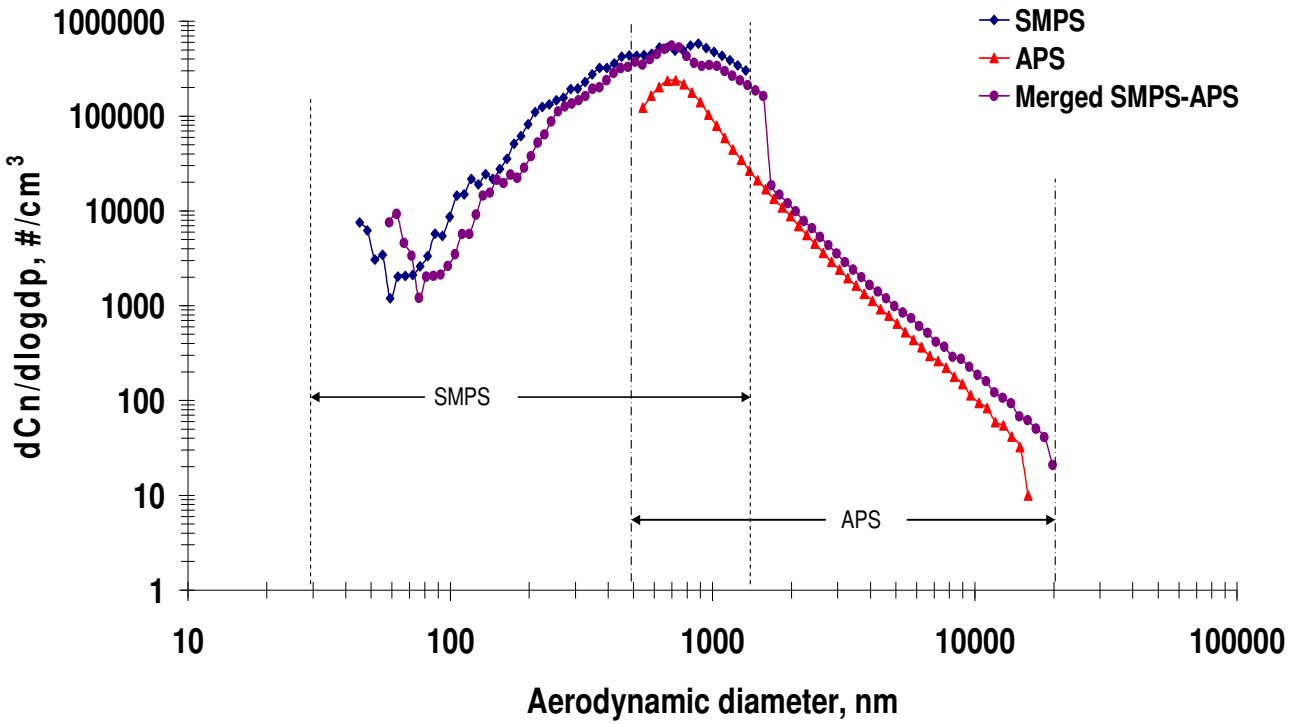

Figure 3.6. Particle size distributions of NA MgO (11 g, 80 psig) at 2 min after deployment - SMPS, APS, and merged SMPS-APS data. The goodness of fit of merged data is 0.030. Each curve represents the mean of three replicates.

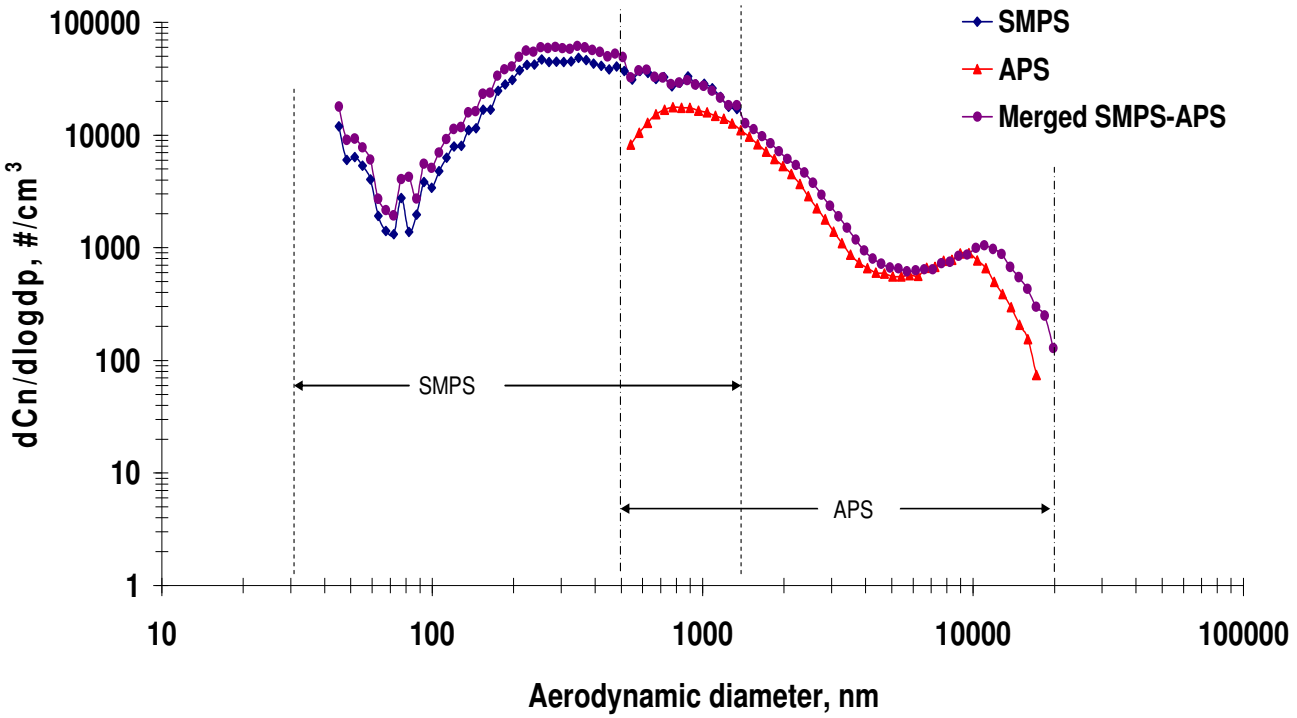

Figure 3.7. Particle size distributions of NA MgO plus (13 g, 80 psig) at 2 min after deployment - SMPS, APS, and merged SMPS-APS data. The goodness of fit of merged data is 0.038. Each curve represents the mean of three replicates.

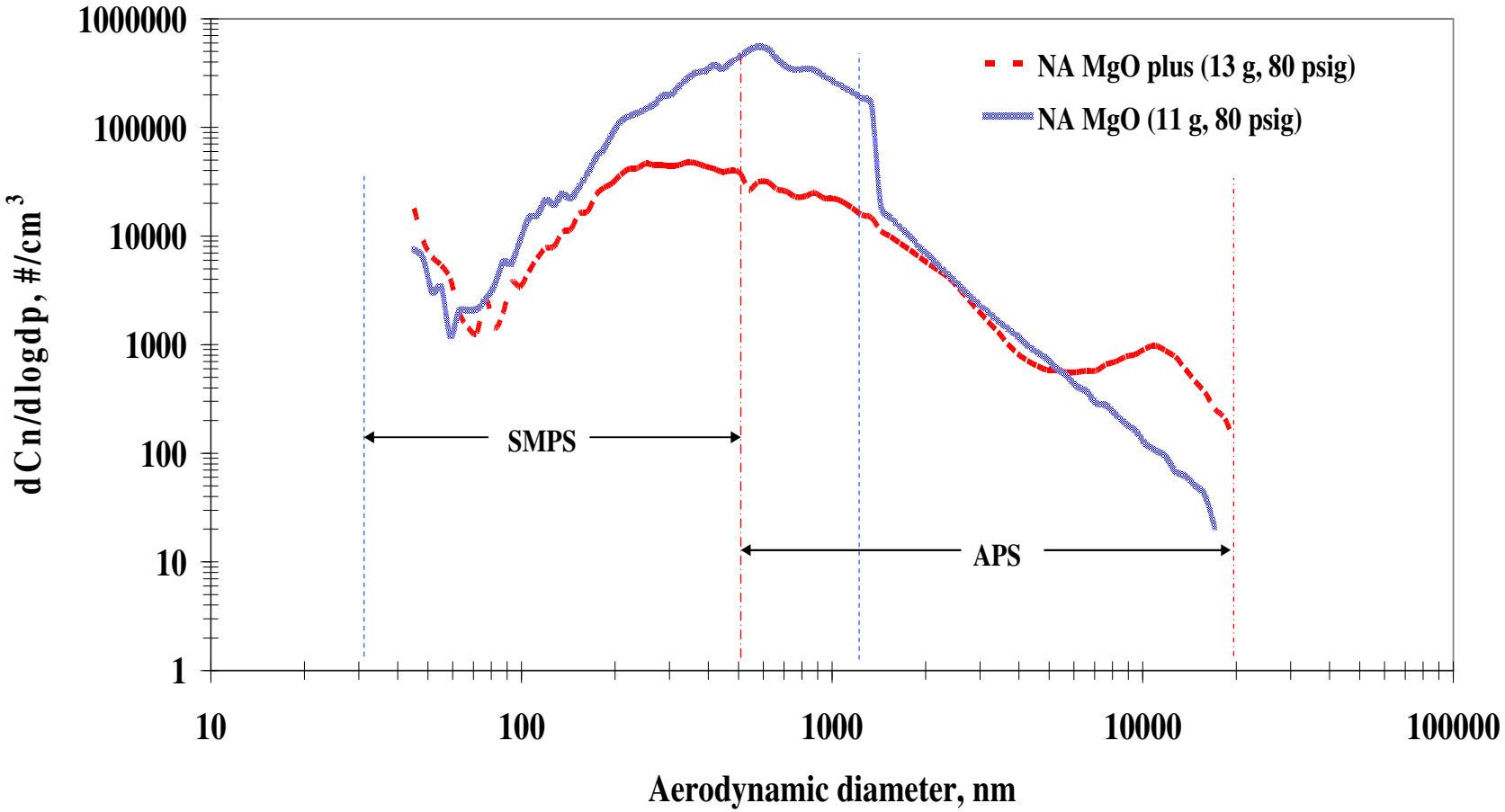

Figure 3.8. Merged SMPS and APS particle size distributions for NA MgO plus and NA MgO at 2 min after deployment. Each curve represents the mean of the three replicates.

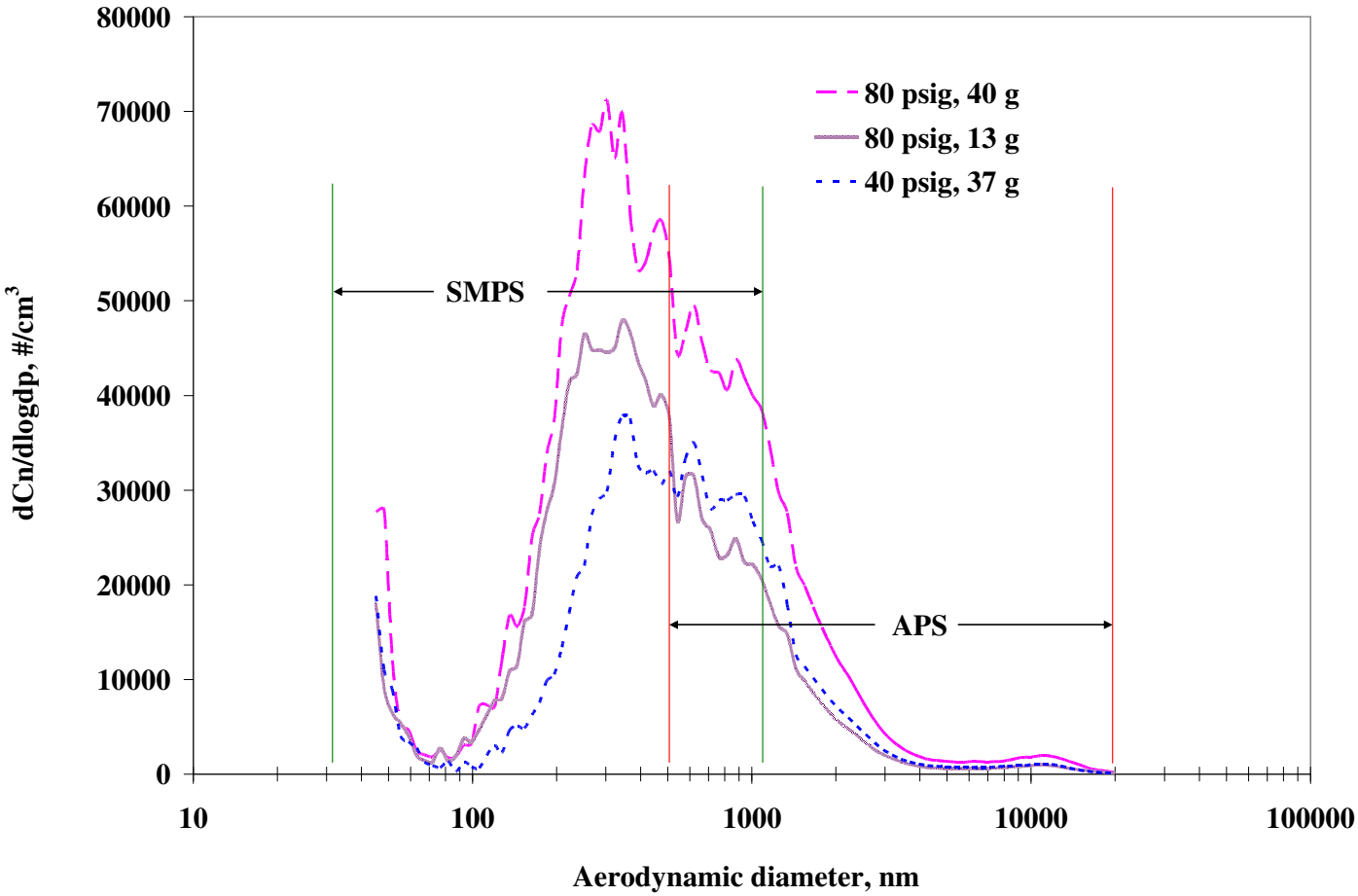

Figure 3.9. Merged SMPS and APS particle size distributions of NA MgO plus as affected by nominal amount and canister pressure at 2 min after deployment. Each curve represents the mean of the three replicates. The goodness of fit values for the merged data are 0.048, 0.045 and 0.038 for deployed mass and dispersion pressure combinations of 40 g and 80 psig, 30 g and 40 psig, and 13 g and 80 psig, respectively.

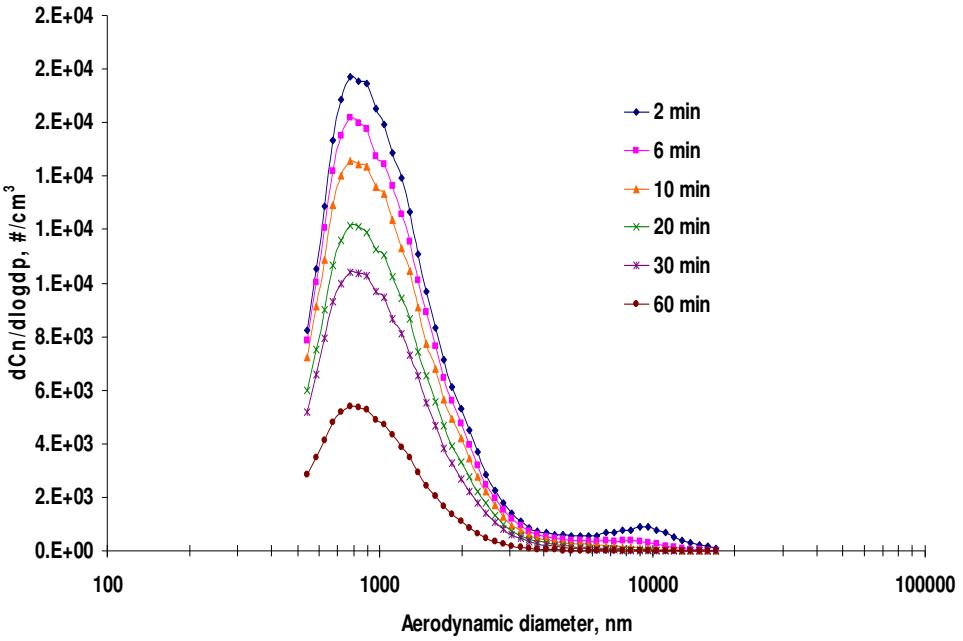

(a)

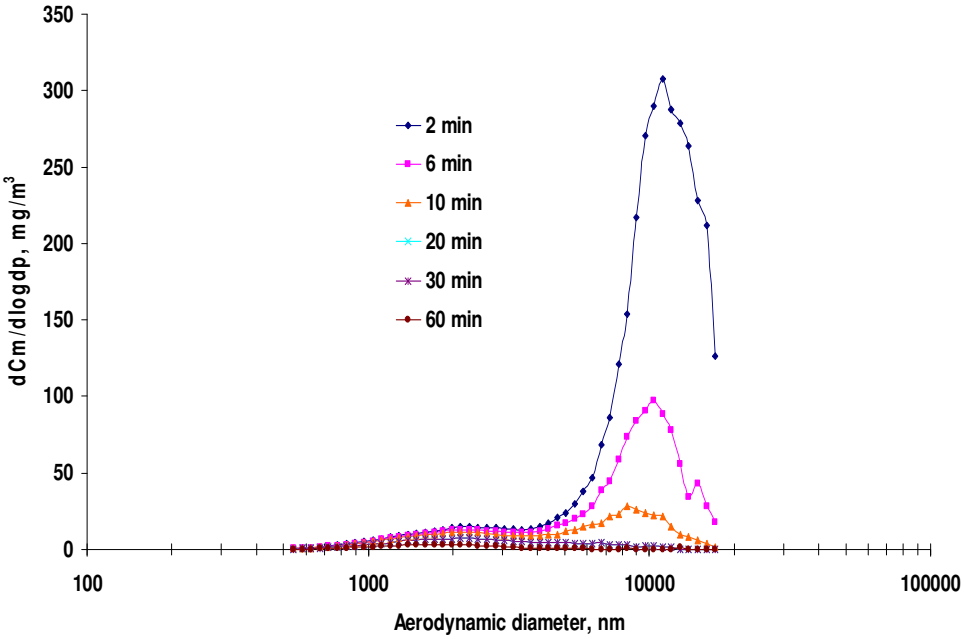

(b)

Figure 3.10. Temporal change in particle size distributions of NA MgO plus measured with APS: number-based (a) and mass-based (b). Each curve represents the mean of three replicates.

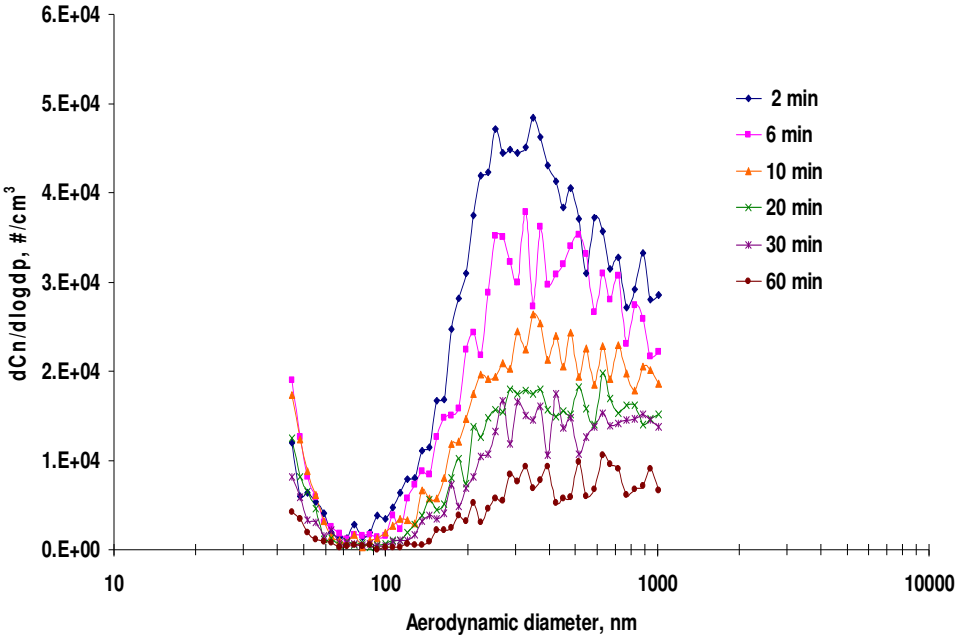

(a)

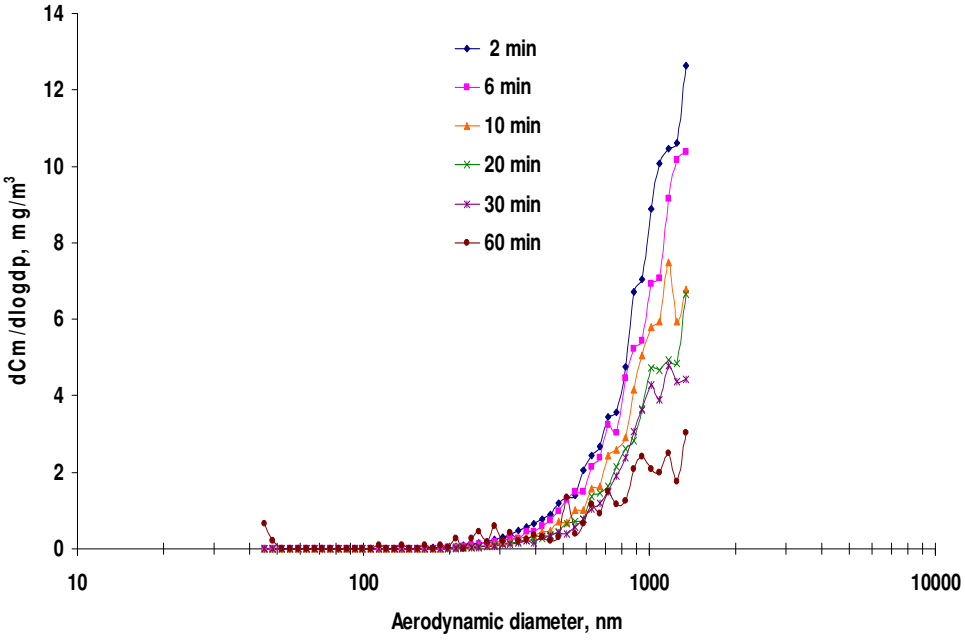

(b)

Figure 3.11. Temporal change in particle size distributions of NA MgO plus measured with SMPS: number-based (a) and mass-based (b). Each curve represents the mean of three replicates.

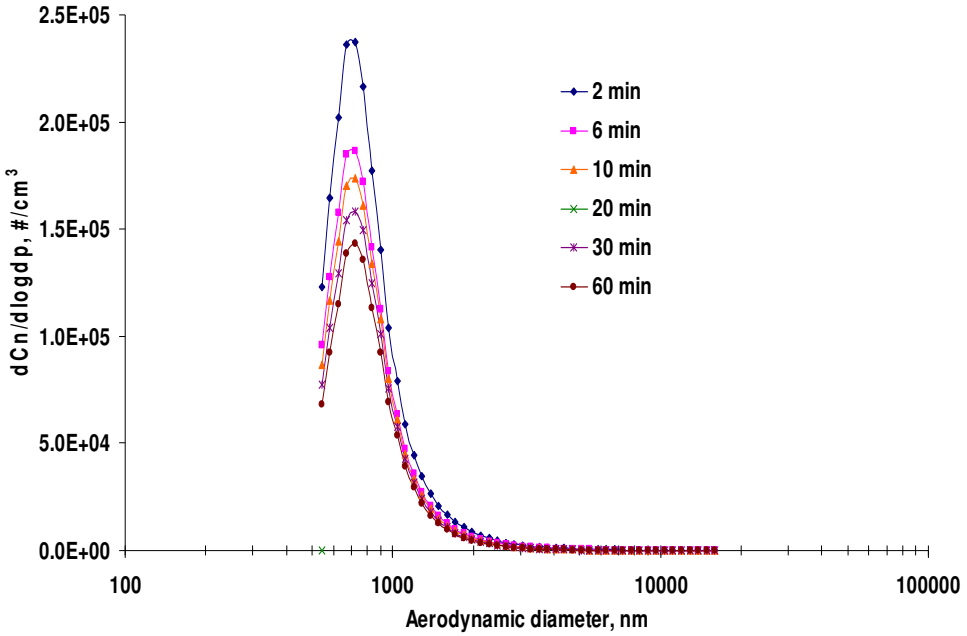

(a)

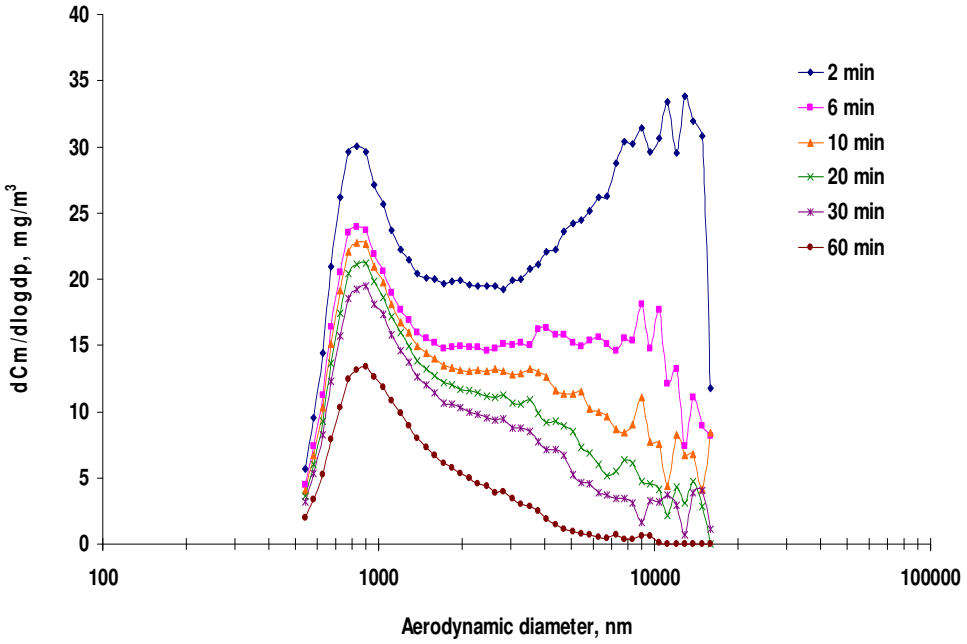

(b)

Figure 3.12. Temporal change in particle size distributions of NA MgO measured with APS: number-based (a) and mass-based (b). Each curve represents the mean of the three replicates.

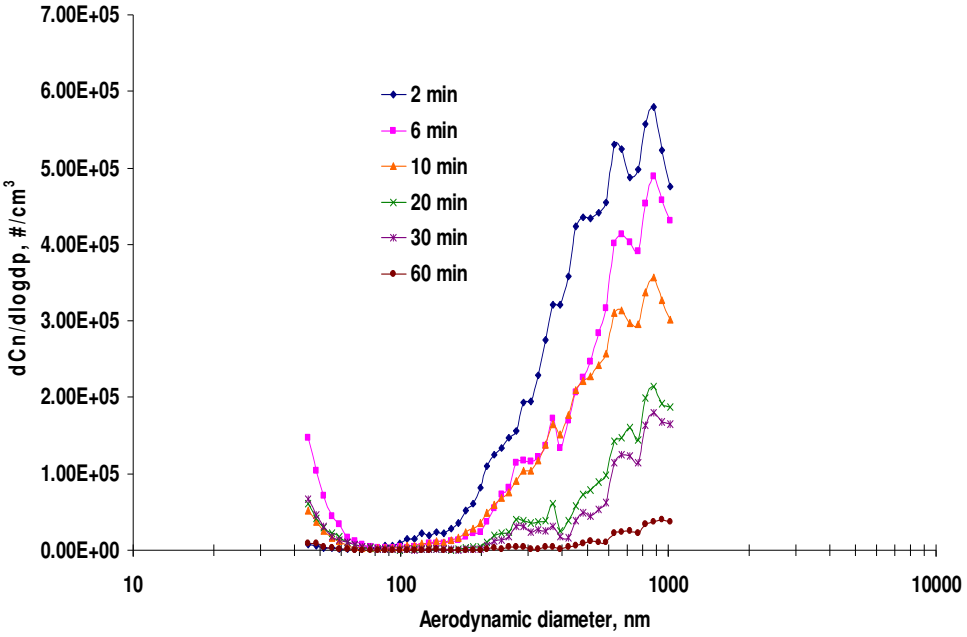

(a)

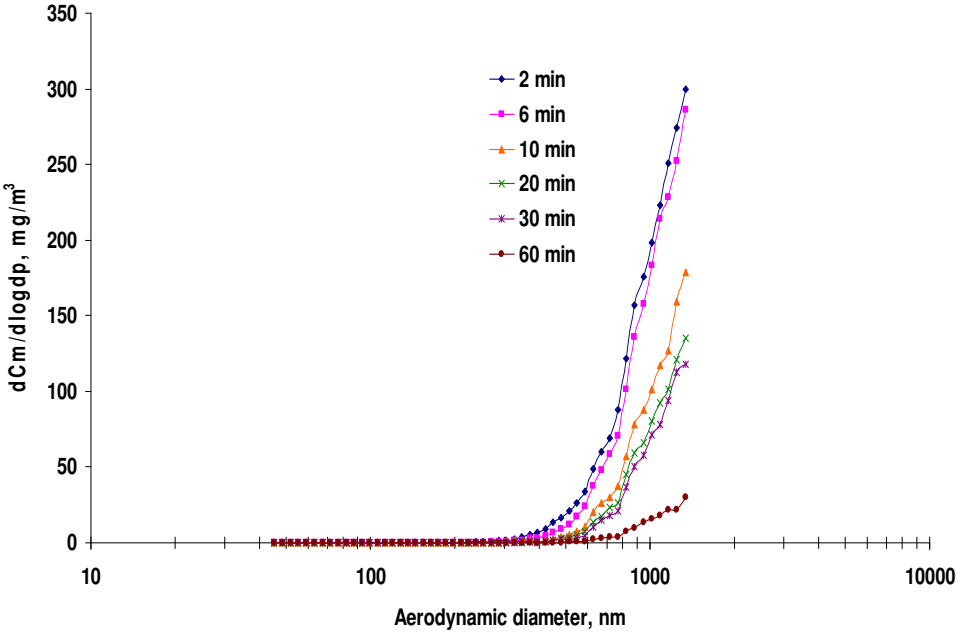

(b)

Figure 3.13. Temporal change in particle size distributions of NA MgO measured with SMPS: number-based (a) and mass-based (b). Each curve represents the mean of the three replicates

Table 3.3. The geometric mean diameters (GMD) of the two nanostructured particles at 2 min after dispersion.

Particle	SMPS[a]		APS		Merged	
	GMD[b], nm	s.d.	GMD[b], µm	s.d.	GMD[b], µm	s.d.
NanoActive® MgO plus, 80 psig, 50 g	911 (b)	35	10.94 (a)	0.60	11.14 (a)	0.51
NanoActive® MgO plus, 80 psig, 20 g	894 (b)	24	11.30 (a)	0.28	11.57 (a)	0.33
NanoActive® MgO plus, 40 psig, 50 g	920 (b)	27	10.51 (a)	1.23	10.60 (a)	1.18
NanoActive® MgO, 80 psig, 50 g	1087 (a)	5	4.19 (b)	0.98	3.12 (b)	1.30

[a]The mobility diameter measured by SMPS was converted to aerodynamic diameter.

[b]Column means followed by the same letter are not significantly different at the 5% level.

Table 3.4. The geometric standard deviations (GSD) of the two nanostructured particles at 2 min after dispersion.

Particle	SMPS		APS		Merged	
	GSD[a]	s.d.	GSD[a]	s.d.	GSD[a]	s.d.
NanoActive® MgO plus, 80 psig, 50 g	1.36 (ab)	0.04	1.66 (b)	0.07	1.69 (b)	0.02
NanoActive® MgO plus, 80 psig, 20 g	1.40 (a)	0.01	1.64 (b)	0.05	1.68 (b)	0.09
NanoActive® MgO plus, 40 psig, 50 g	1.35 (ab)	0.03	1.68 (b)	0.10	1.74 (b)	0.08
NanoActive® MgO, 80 psig, 50 g	1.31 (b)	0.01	2.93 (a)	0.09	2.85 (a)	0.32

[a]Column means followed by the same letter are not significantly different at the 5% level.

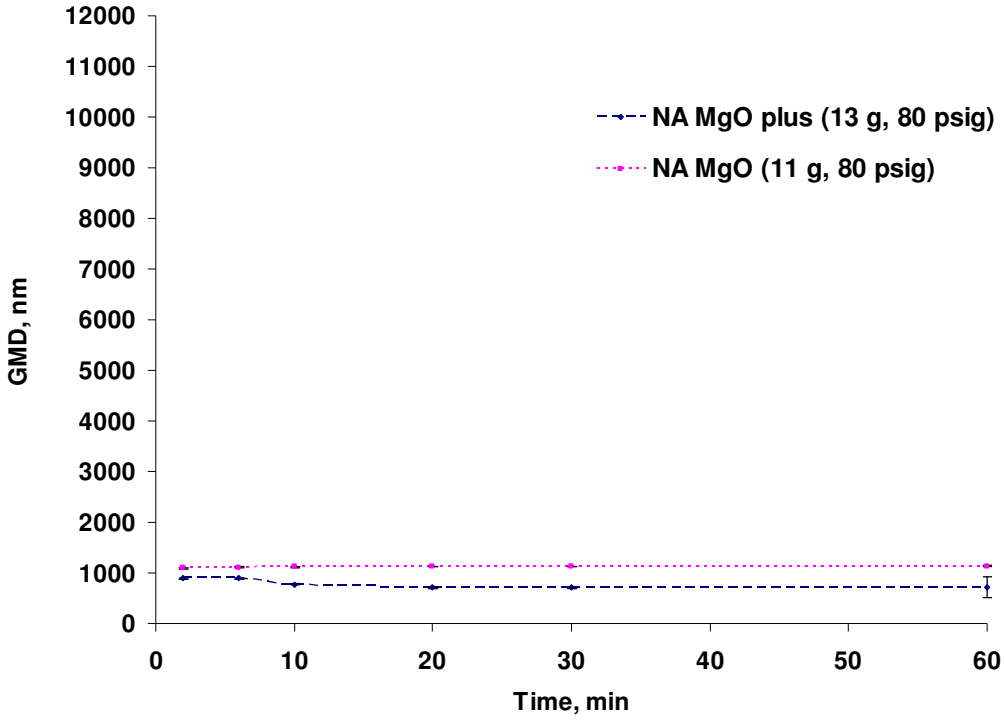

(a)

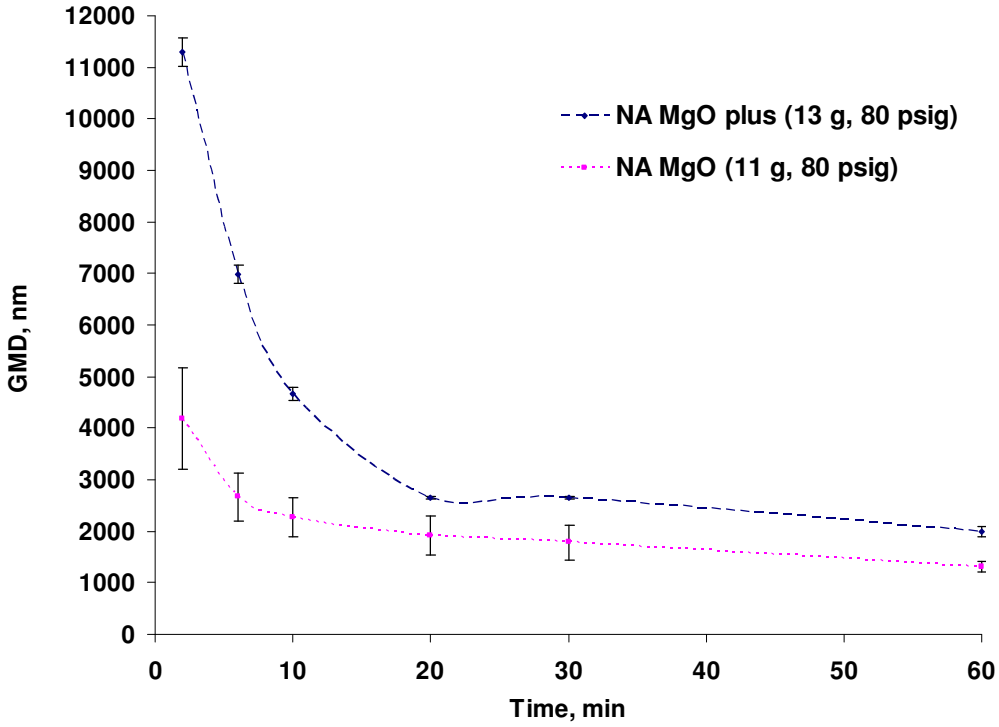

(b)

Figure 3.14. Temporal change in geometric mean diameters (GMD) of NA MgO and NA MgO plus as measured by SMPS (a) and APS (b). Each curve represents the mean of three replicates. Error bars represent one standard deviation.

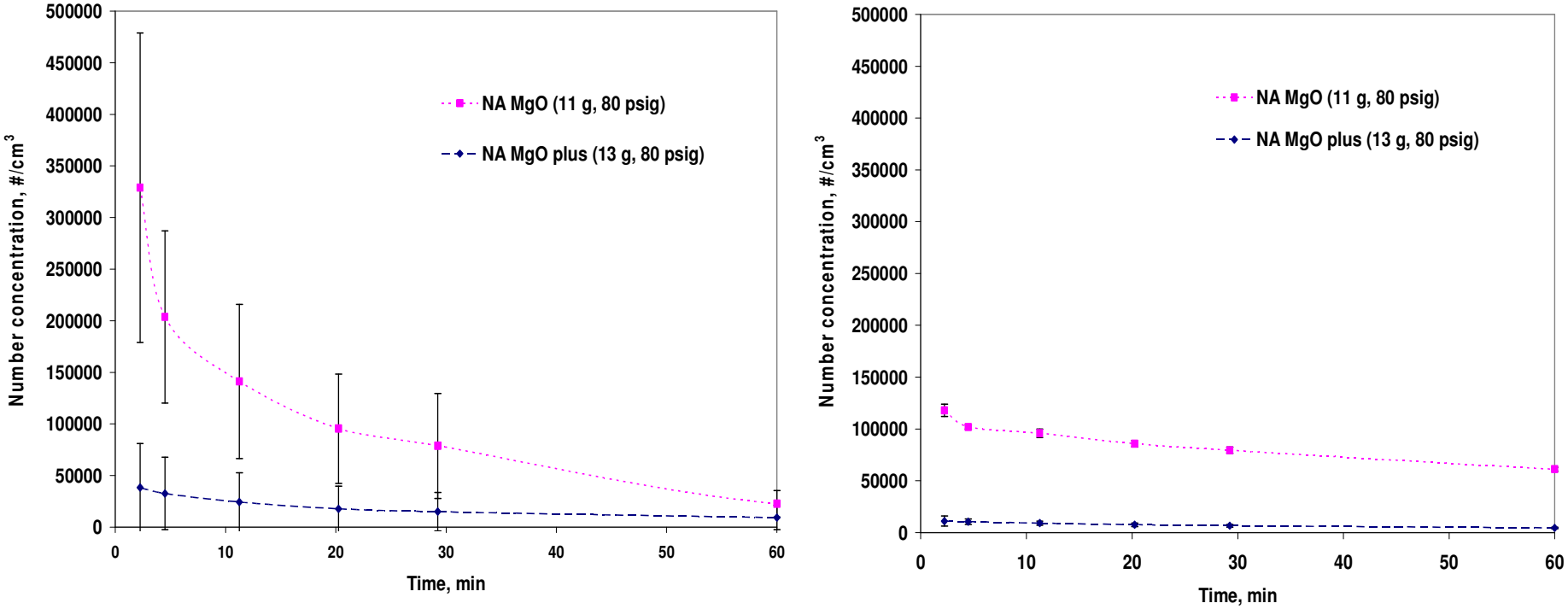

Figure 3.15. Number concentrations of NA MgO plus and NA MgO, as measured by the SMPS (a) and APS (b). Each curve represents the mean of three replicates. Error bars represent one standard deviation.

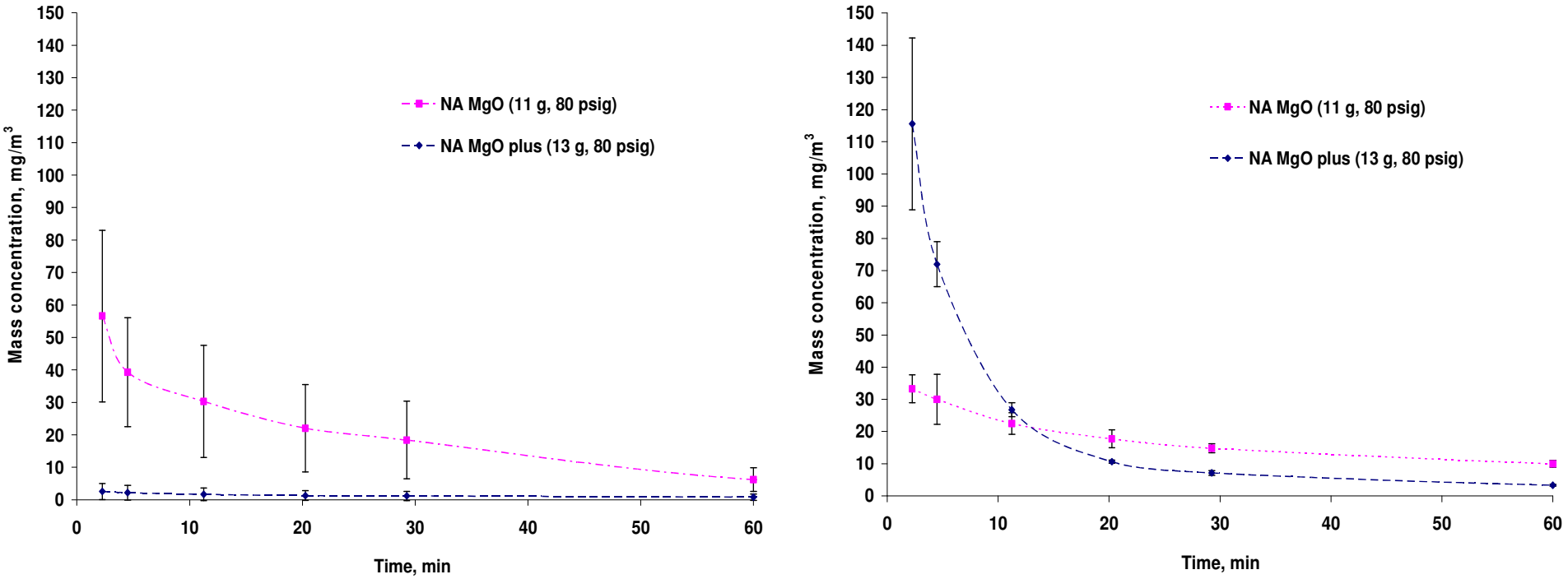

Figure 3.16. Mass concentrations of NA MgO plus and NA MgO, as measured by the SMPS (a) and APS (b). Each curve represents the mean of the three replicates. Error bars represent one standard deviation.

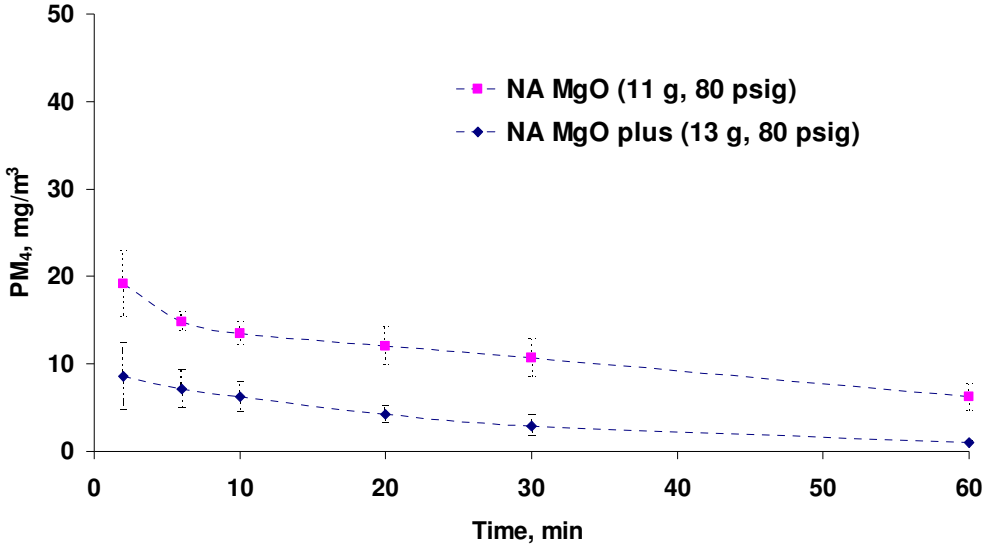

Figure 3.17. Temporal change in the PM_4 concentration of the two nanostructured particles from APS. Each curve represents the mean of three replicates. Error bars represent one standard deviation.

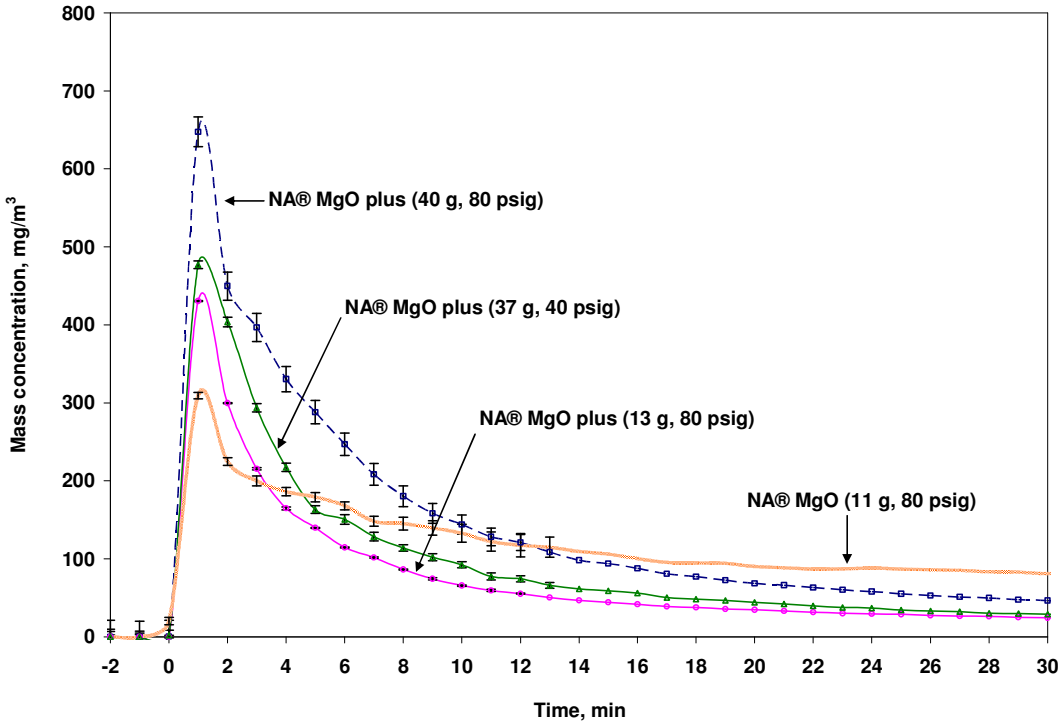

Figure 3.18. Mass concentrations of NA MgO plus and NA MgO as measured by the TEOM. Each curve represents the mean of three replicates. Error bars represent one standard deviation.

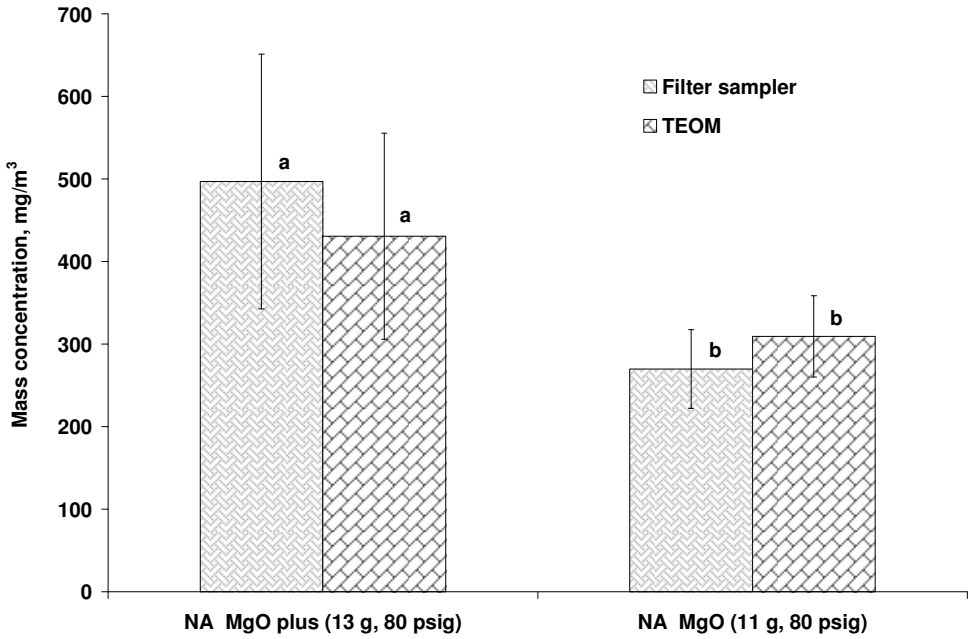

Figure 3.19. Comparison of the mass concentrations measured by TEOM and filter samplers at 1 min after dispersion. Each curve represents the mean of three replicates. Bars with the same letters are not significantly different at the 5% level.

3.6 References

ACGIH. 1993. Threshold limit values for chemical substances and physical agents and biological exposure indices. Cincinnati, OH: American Conference of Government Industrial Hygienists.

Braley, B. 2005. P articulate deployment: manipulation and control. M.S. Thesis. Manhattan, KS: Kansas State University

Carnes C.L. and K.J. Klabunde. 2002. Unique chemical reactivities of nanocrystalline metal oxides toward hydrogen sulfide. *Chemistry of Materials* 14(4):1806-1811.

Congrong, H., M. Lidia, and G. Dale. 2005. Particle deposition rate in residential houses. *Atmospheric Environment* 39(21):3891-3899.

Decker S.P., J. Klabunde, A. Khaleel, and K.J. Klabunde. 2002. Catalyzed destructive adsorption of environmental toxins with nanocrystalline metal oxides. *Environmental Science and Technology* 36(4):762-768.

Heitbrink, W.A., P.A. Baron, and K. Willeke. 1991. Coincidence in time-of-flight aerosol spectrometers. Phantom particle creation. *Aerosol Science and Technology* 14(1):112-126.

Jillavenkatesa, A. and J.F. Kelly. 2002. Nanopowder characterization: challenges and future directions. *Journal of Nanoparticle Research* 4(5):463-468.

Kakumanu, B. 2005. Physical characterization of aerosolized particles. M.S. Thesis. Manhattan, KS: Kansas State University.

Koper O.B., J. Klabunde, G.L. Marchin, K.J. Klabunde, P. Stoimenov, and L. Bohra. 2002. Nanoscale powders and formulations with biocidal activity toward spores and vegetative cells of Bacillus species, viruses, and toxins *Current Microbiology.* 44(1):49-55.

Morawska, L., N.D. Bofinger, L. Kocis, and A. Nwankwoala. 1998. Submicrometer and supermicrometer particles from diesel vehicle emissions. *Environment Science and Technology* 32(14):2033-2042.

NanoScale Materials. 2004a. NanoActive Magnesium Oxide. Na102 v. 2. Available at: www.nanoactive.com. Accessed 12 April 2006.

NanoScale Materials. 2004b. NanoActive Magnesium Oxide Plus. Na101 v. 2. Available at: www.nanoactive.com. Accessed 12 April 2006.

Peters, T.M., D. Ott, and P.T. O'Shaughnessy. 2006. Comparison of the Grimm 1.108 and 1.109 portable aerosol spectrometer to the TSI 3321 aerodynamic particle sizer for dry particles. *Annals of Occupational Hygiene* 50(8):843-850.

Sioutas, C., E. Abt, J.M. Wolfson, and P. Koutrakis. 1999. Evaluation of the measurement performance of the scanning mobility particle sizer and aerodynamic particle sizer. *Aerosol Science and Technology* 30(1):84-92.

Tokonami, S. and E.O. Knutson. 2000. The scan time effect on the particle size distribution measurement in the scanning mobility particle sizer system. *Aerosol Science and Technology* 32(3):249-252.

TSI. 2005a. Model 3321 Aerodynamic Particle Sizer® Spectrometer. Revision E. Shoreview, MN: TSI Inc.

TSI. 2005b. Aerosol Instrument Manager® Software for APS™ Spectrometer. Revision C. Shoreview, MN: TSI Inc.

TSI. 2005c. Model 3936 Scanning Mobility Particle Sizer™ (SMPS) Spectrometer. Revision J. Shoreview, MN: TSI Inc.

TSI. 2005d. Aerosol Instrument Manager® Software for Scanning Mobility Particle Sizer™ (SMPS) Spectrometer. Revision C. Shoreview, MN: TSI Inc.

Wang, Z.L., Y. Liu and Z. Zhang. 2003. Handbook of nanophase and nanostructured materials. Vol. II: Characterization. New York: Kluwer Academic/Plenum Publishers.

Wagner, G.W., P.W. Bartram, O. Koper, and K.J. Klabunde. 1999. Reactions of VX, GD, and HD with Nanosize MgO. *Journal of Physical Chemistry B* 103(16):3225-3228.

Yadav, R. 2005. Effectiveness of nanostructured particles in clearing glycol smoke in enclosed spaces. M.S. Thesis. Manhattan, KS: Kansas State University.

Yadav, R., R.G. Maghirang, L.E. Erickson, B. Kakumanu, and S.G. Castro. 2008. Laboratory evaluation of the effectiveness of nanostructured and conventional particles in clearing smoke in confined spaces. *Fire Safety Journal* 41(1):36-41.

Zhang, N., Z.C. Zheng, and R.G. Maghirang. 2007. Numerical simulation of smoke dissipation with dispersed nanoparticle aggregates. *International Journal for Numerical Methods in Engineering* (DOI: 10.1002/nme.2186).

4. Infrared Extinction Properties of Nanostructured and Conventional Particles

4.1 Abstract

The increasing threat of emerging battlefield sensors within the infrared (IR) region of the electromagnetic spectrum has led to renewed interest in particulate obscurants that are effective in the IR bands. Brass flakes and carbon-based particulates are effective IR obscurants; however, they are toxic, causing respiratory problems and environmental concerns. There is a need to develop or identify non-toxic IR obscurants. This research was conducted to determine the potential of nanostructured particles as IR obscurants. Three commercial nanostructured particles (i.e., NanoActive® MgO plus, NanoActive® MgO, and NanoActive® TiO_2) and two metal oxide nanorods (i.e., MgO and TiO_2) were considered and compared with other particulates, including two conventional particles (i.e., $NaHCO_3$ and ISO fine test dust) and common obscurants (i.e., brass flakes, graphite flakes, and carbon black). Experiments involved dispersing a known mass of particles into the sample chamber of a Fourier Transform Infrared spectrometer and measuring simultaneously the IR transmission, the mass concentration, and the aerodynamic diameter of dispersed particles. The tap or packing density of the particles was also measured. From the measured data, the mean values of the mass extinction coefficient, σ_m, and volume extinction coefficient, σ_v, for the spectral bands of interest (i.e., 3-5 and 8-12 μm) were calculated. Results showed that the nanostructured particles had significantly smaller σ_m and σ_v values than the other particles. Graphite flakes had the greatest overall mean σ_m value (3.22 m^2/g, s.d. = 0.40), followed by carbon black (1.72 m^2/g, 0.41), brass flakes (1.57 m^2/g, 0.38), and ISO

fine test dust (0.74 m^2/g, 0.03). Brass flakes had the greatest overall mean σ_v (1.64 m^2/cc, 0.39), followed by $NaHCO_3$ (0.93 m^2/cc, 0.12), ISO fine test dust (0.91 m^2/cc, 0.03), and graphite flakes (0.80 m^2/cc, 0.10).

4.2 Introduction

Obscurants in the infrared (IR) region of the electromagnetic spectrum have played a major role in military operations because they provide protection of military personnel, equipment, and installation from IR seeking sensors of unfriendly forces (Singh et al., 1994; Ladouceur et al., 1997; Butler, 1998; Shi et al., 1998; Shi et al., 2003). Obscurants that are effective in IR have received renewed interest because of increasing threat of emerging IR sensors (Farmer and Krist, 1981; Farmer et al., 1982; Shi et al., 2003; Singh et al., 1994; Appleyard and Davies, 2004b; Wang et al., 2004).

For obscurants to be considered effective, they must exhibit high extinction coefficients and at the same time not be harmful to human health and the environment. They also must be easy to deploy, readily available, and cost effective (Owrutsky et al., 2000). The extinction coefficient or extinction cross-section of an obscurant is a measure of its ability to attenuate the incident radiant energy at a certain wavelength (Shi et al., 1998). It is expressed either as the mass extinction coefficient, σ_m, or volume extinction coefficient, σ_v (Owrutsky et al., 2000). For military applications, the σ_v value of an obscurant is likely more important than the σ_m value because most deployment methods (e.g., grenade) are volume-limited rather than mass-limited (Owrutsky et al., 2001).

Extinction coefficients are typically expressed as averages over the spectral band of interest (Farmer, 1991). In military applications, the wavebands of increasing importance are the 3-5 and 8-12 μm wavelengths in the mid-IR region. These ranges are the main “atmospheric

windows" or the regions in the electromagnetic spectrum in which IR transmission is close to 100% regardless of the presence of atmospheric gases, including water vapor and carbon dioxide (CO_2) (Jacobson, 1999; Bailey et al., 2002; Hutchison and Cracknell, 2005).

Many factors can influence the IR extinction properties of particles. In general, highly conducting materials (e.g., brass flakes, graphite flakes) are effective IR obscurants. Appleyard (2006) noted that, based on theoretical analysis, the conductivity of the particles appeared to be the most important property. Salts, metal oxides, and semiconductors generally have good IR absorption properties, because of their moderately strong molecular vibrations in the IR region (Owrutsky et al., 2001; Stuart, 2004). Other factors that affect extinction properties include chemical composition, size distribution, concentration, and morphology of particles (Ladouceur et al., 1997; Shi et al., 1998; Widmann et al., 2005). Morphology is particularly important as it influences the coagulation process and removal of particles from the air (Colbeck et al., 1997). Structures such as thin disc flakes and thin fibers have exhibited high extinction coefficients (Appleyard and Davies, 2004b; Appleyard, 2006). The molecular structure of the material, primary particle size, and structure of the aggregate also affect the effectiveness of obscurants (Dobbins et al., 1994; Shi et al., 1998). In a study conducted by Appleyard (2006) using high-aspect ratio particles, the optimum particle dimensions were ~ 5 μm diameter and ~ 25 nm thickness for flakes and ~ 10-200 nm diameter and ~ 10 μm length for fibers.

The extinction property of an obscurant may be determined either theoretically or experimentally. Appleyard (2007) modeled the extinction properties of non-spherical particles as a function of particle orientation with respect to incident radiation. Comparison of theoretical and experimental results on extinction coefficients indicated good agreement for TiO_2 and SiO_2 (Appleyard and Davies, 2004a) but not for iron oxides (Owrutsky et al., 2000; Owrutsky et al.,

2001). Direct measurement is the preferred approach to determine the extinction coefficient of particles (Widmann et al., 2005). This approach, however, poses a challenge because of difficulty in measuring simultaneously the IR transmission through the obscurant and the mass concentration corresponding to that transmission value (Owrutsky et al., 2000). As such, direct measurement typically involves use of laboratory bench scale apparatus like the Fourier Transform Infrared (FTIR) spectrometer in which powders are entrained in a tube or chamber for mass concentration measurement (Ladouceur et al., 1997; Owrutsky et al., 2000; Owrutsky et al., 2001).

The U.S. Army has demonstrated that brass exhibits favorable obscuration properties; however, it is highly toxic (rated 9 by Environmental Protection Agency (EPA) on a scale of 0-9) and environmentally detrimental (Haley and Kurnas, 1993; Owrutsky et al., 2000). Graphite has a much lower toxicity (EPA toxicity rating of 4) and environmental impact than brass (Haley and Kurnas, 1993; Owrutsky et al., 2000); however, its packing density is much lower than that of brass (Ladouceur et al., 1997). Carbon black, another carbonaceous material like graphite, has been identified by Owrutsky et al. (2001) as one of the best obscurants. Like graphite, however, carbon black has a much lower packing density than brass.

This research was conducted to evaluate the extinction coefficients of nanostructured particles in the mid-IR range. The σ_m and σ_v values of the nanostructured particles were determined and compared with those of conventional particles and common obscurants.

4.3 Materials and Methods

4.3.1 Experimental apparatus

The experimental apparatus had three major components: FTIR spectrometer (Model 6700, Nicolet, Madison, WI), particle chamber, and powder disperser. The FTIR spectrometer

was configured to provide mid-IR radiation (i.e., 1.35 – 25 μm wavelength), and was calibrated using monodisperse polystyrene spheres. The OMNIC™ software was used to acquire, process, and analyze the spectral data (Thermo Electron, 2006). The particle chamber (Fig. 4.1) was set up on top of the sampling compartment of the FTIR spectrometer. The chamber was 40.6 cm. wide, 16.5 cm thick, and 63.5 cm high. Near the bottom part at each side of the chamber were two holes with PVC pipes (3.81 cm diameter and 2.54 cm long) for the passage of the IR beam produced by the FTIR spectrometer. Two filter samplers were placed directly above the two PVC pipes for time-averaged measurement of particle mass concentration. An Aerodynamic Particle Sizer® (APS) spectrometer (Model 3321, TSI Inc., Shoreview, MN) was used to monitor the aerodynamic diameter and number concentration of the airborne particles. The chamber was also equipped with a small fan for mixing, sliding doors to protect the KBr optical windows of the spectrometer, and a chamber extension for pressure release.

A powder disperser, made of a plastic container with eight holes (approximately 6 mm in diameter) on one side, was used to aerosolize and disperse the particles inside the chamber. A known mass (approximately 3 g) of particles was placed inside the powder disperser, which was connected to a compressed nitrogen gas tank through a hose and a nozzle. By manually pressing the nozzle, the nitrogen gas (tank pressure gauge was set at 30 psig) passes through the container, dispersing the particles into the chamber.

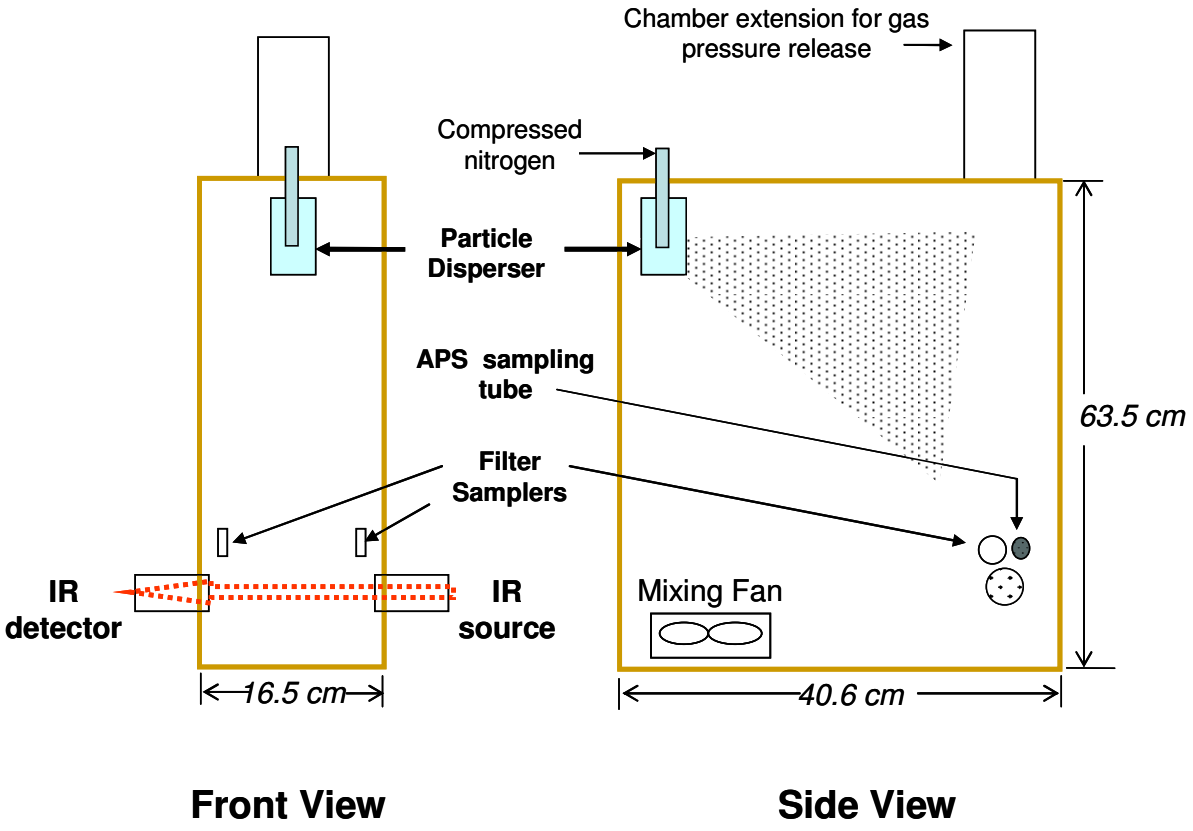

Figure 4.1. Schematic diagram of the experimental chamber showing the instruments (not drawn to scale).

4.3.2 Particulate obscurants

Four types of particles were considered in the study: (1) nanostructured metal oxide particles (i.e., NanoActive® MgO plus, NanoActive® MgO, and NanoActive® TiO_2); (2) conventional particles (i.e., $NaHCO_3$ and ISO fine test dust); (3) reference obscurants (i.e., brass flakes, graphite flakes, and carbon black); and (4) metal oxide nanorods (i.e., MgO nanorods and TiO_2 nanorods). Figures 4.2-4.5 show the scanning electron microscope images of the particles. Table 4.1 summarizes the surface area and chemical composition of the particles. The brass flakes (Premior 505, Wolsteinholme International Inc., West Chicago, IL) had a mean size of approximately 5.0 µm. The graphite flakes and carbon black (Asbury Graphite Mills, Inc.,

Asbury, NJ) had a mean size and primary particles size of 5.3 µm and 35 nm, respectively. These particles were chosen as reference particles because they are the most commonly studied obscurants (Owrutsky et al., 2000; 2001). Brass is one of the best predicted attenuators of IR radiation (Appleyard, 2007) and the most commonly used obscurant by the military. The NanoActive® metal oxide powders (NanoScale Corp., Manhattan, KS) were selected because of their unique morphology, large surface areas, and relatively non-toxic nature. Also, TiO_2 is a semi-conductor and is expected to have good values of extinction coefficient. It has an EPA toxicity rating of 0 (Haley and Kurnas, 1993; Owrutsky et al., 2000). ISO fine test dust was selected for its good conductivity and flaky structure; $NaHCO_3$ was selected because it is relatively non toxic and also is a salt. The nanorods (MgO nanorods and TiO_2 nanorods) were synthesized in the Department of Chemistry, Kansas State University and were considered because of their relatively high aspect ratio and non toxic nature.

For the extinction coefficient determination, there were three replicates for each type of particle. For the aerodynamic size characterization, there were also three replicates for all particles except the nanorod, which had only two replicates because of the malfunctioning of the APS spectrometer.

4.3.3 Experimental procedure

4.3.3.1 Measurement of extinction coefficients and particle size distribution

The particle chamber (Fig. 4.1) was first conditioned by flushing it with dry compressed air for at least 30 min to remove or reduce any water vapor inside the chamber. A background spectrum (i.e., without the obscurant) was collected before dispersion of the particles into the chamber. Then, the sliding door in front of the KBr optical window of the FTIR spectrometer was closed to protect the KBr optics from particles that might stick into it upon dispersion of

particles. The mixing fan inside the chamber was turned on and particles were dispersed into the chamber by manually pressing the nozzle of the powder disperser. Once particles were dispersed, the fan was turned off and the sliding doors were opened to let the passage of the IR beam through the two KBr windows.

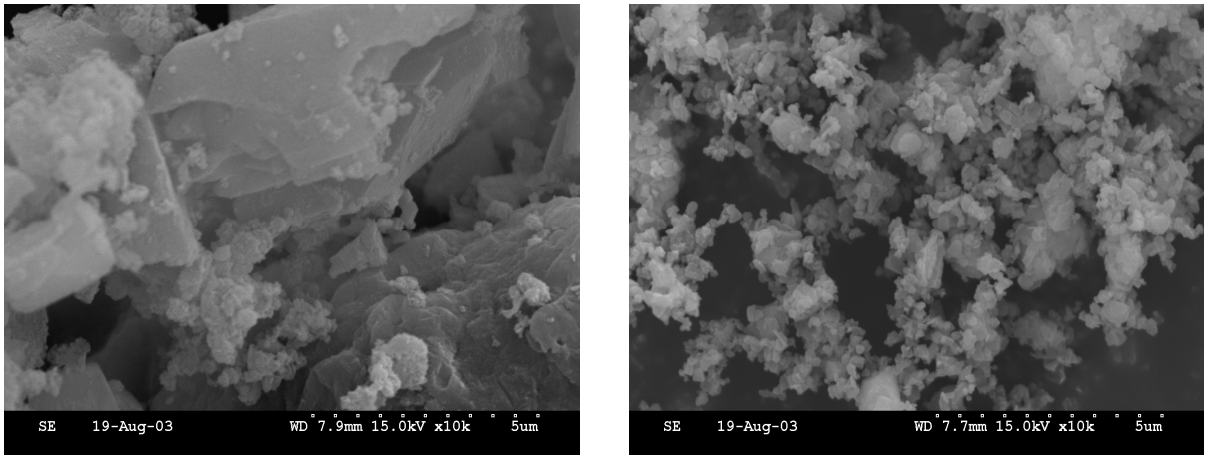

(a) (b)

Figure 4.2. Scanning electron microscope (SEM) images of the nanostructured metal oxide particles: (a) NanoActive® MgO plus and (b) NanoActive® MgO.

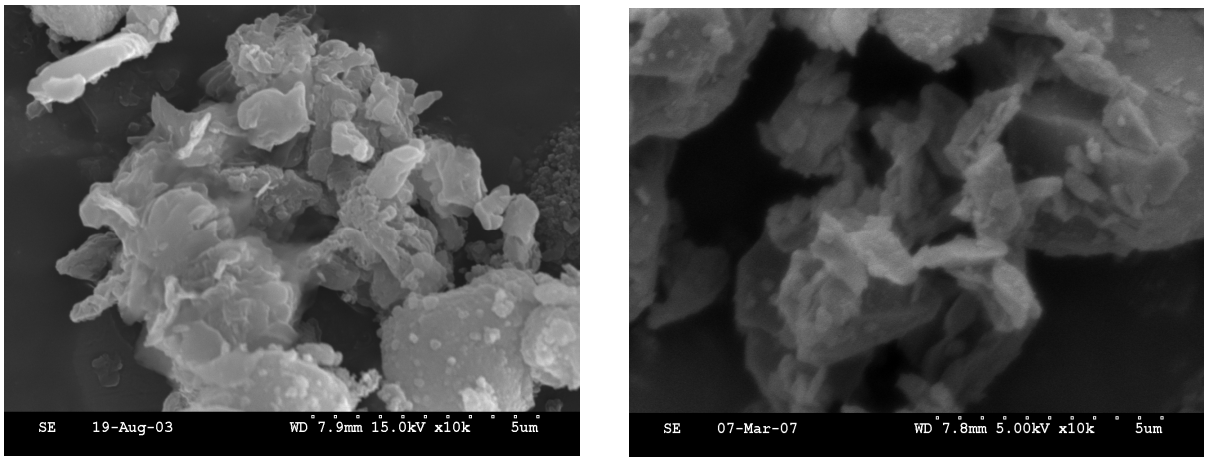

(a) (b)

Figure 4.3. SEM images of the conventional particles: (a) $NaHCO_3$ and (b) ISO fine test dust.

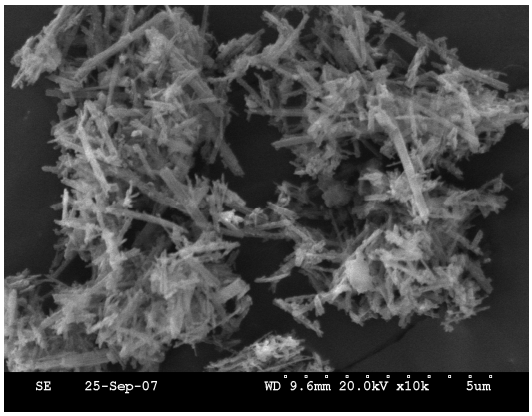

(a)

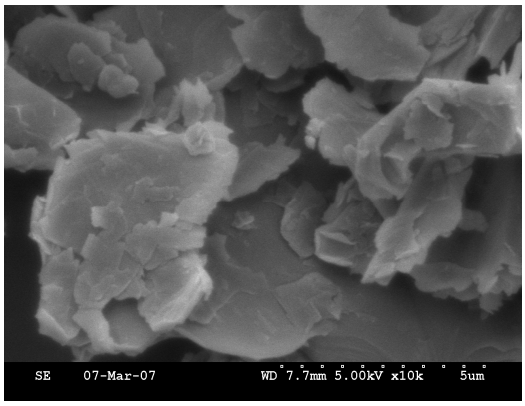

(b)

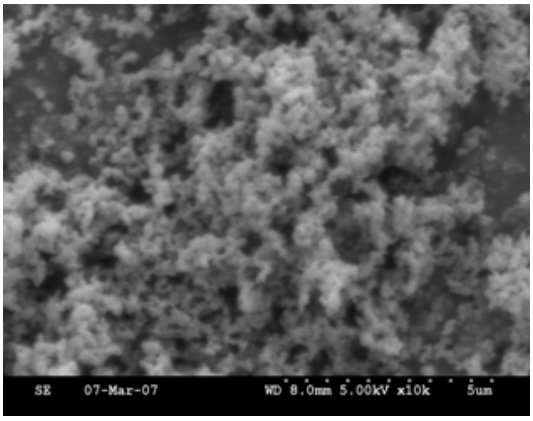

(c)

Figure 4.4. SEM images of the reference particles: (a) brass flakes, (b) graphite flakes, and (c) carbon black.

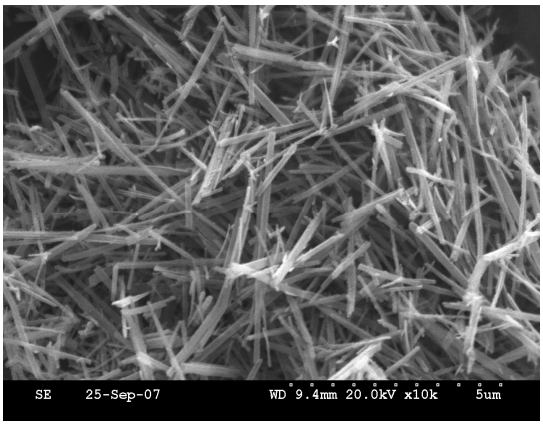

(a)

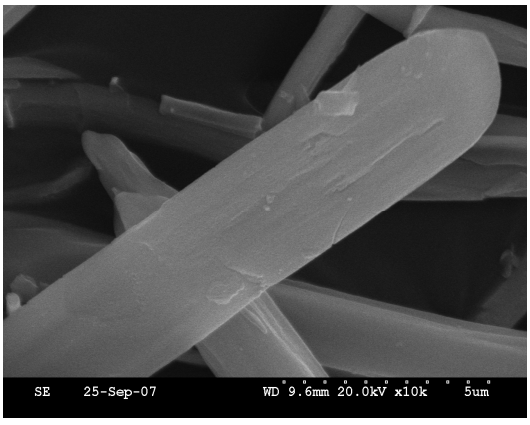

(b)

Figure 4.5. SEM images of the nanorods: (a) MgO nanorods and (b) TiO_2 nanorods.

Table 4.1. Physical and chemical properties of the particles.

Particle	Appearance/color	Surface area, m^2/g	Crystalline size, nm	Median aggregate size, μm	Major chemical composition (Percent by weight)	True density[f], g/cc
NanoActive® particles						
NanoActive® MgO plus[a]	white powder	≥ 600	≤ 4	12.00	99.62% Mg	2.46
NanoActive® MgO[a]	white powder	≥ 230	≤ 8	3.30	95% Mg	3.44
NanoActive® TiO_2[a]	white powder	≥ 500	Amorphous	5.00	99.99% Ti	3.64
Conventional particles						
$NaHCO_3$ (siliconized)[b]	white powder	-[h]	-	7.70	93% $NaHCO_3$	2.27
ISO Fine test dust[c]	reddish brown powder	-	-		68-76% SiO_2 10-15% Al_2O_3	2.76
Reference obscurants						
Brass flakes[d]	brass/bronze powder	1.20	-	5.00	69-91% Copper 29.5-7.5% Zinc	6.54
Graphite flakes[e]	dark gray powder	17.33	-	4.90	99.17% carbon	2.03
Carbon black[e]	black powder	36.26	-	-	99.73% carbon	1.80
Nanorods						
MgO nanorods[g]	white powder	-	-	7.2 (length) 0.5 (width)	-	2.66
TiO_2 nanorods[g]	white powder	-	-	15-25 (length) 1-3 (diameter)	-	4.80

[a]Source: NanoScale Materials, Inc., Manhattan, KS
[b]Source: Amerex Corp., Trussville, AL
[c]Source: PTI Powder Technology, Inc., Burnville, MN
[d]Source: Wolstenholme International Inc., Chicago, IL
[e]Source: Asbury Graphite Mills, Inc., Asbury, NJ
[f] Measured using multipycnometer
[g] Source: Dept. of Chemistry, KSU, Manhattan, KS
[h]No data

The sample spectrum was obtained through the OMNIC™ software. The software was configured to scan at 2 wavenumber resolution and 16 scans lasting for about 45-50 s per sampling. The software was also configured such that the sample spectrum was divided by the background spectrum (called "ratioing") to account for the spectral characteristics of the chamber and the instrument (i.e., IR absorption due to any atmospheric water vapor and CO_2) (Thermo Electron, 2006).

After the first sample spectrum was obtained, the sampling pump of the filter samplers was started and operated for 1 min at a sampling rate of 2 L/min. After particle sampling, another sample spectrum was obtained. The APS spectrometer was started from the time the first sample spectrum was obtained. It sampled aerosol once a minute for 20 min after dispersion.

4.3.3.2 Measurement of the tap density

The tap density of each particle was measured in accordance with ASTM Standard B 527-93 (ASTM Standards, 2006). The procedure involved tapping a 100 cc graduated cylinder, containing 50 g of powder, against a firm horizontal base. The tapping of the graduated cylinder was done manually at 3 mm stroke height and 110-150 taps/min. Tapping of cylinder was stopped when no further decrease in volume of the powder was observed. The tap density was calculated by dividing the mass of the powder by the volume of the tapped powder.

For the MgO and TiO_2 nanorods, the procedure used by Owrutsky et al. (2001) was adopted because of the limited mass of the nanorods. In the Owrutsky et al. (2001) procedure, 4-5 mL of the nanorods was placed in a 10 mL graduated cylinder. The cylinder was tapped until there was no more recognizable change in volume. The mass of the powder inside the cylinder was weighed and divided by the volume to obtain the tap density.

4.3.3.3 Data analysis

The IR transmittance (T^*) values measured by the FTIR spectrometer were converted to absorbance (A) values using the OMNIC software (Thermo Electron, 2006):

$$A_{(\lambda)} = \log\left(1 \Big/ T^*_{(\lambda)} \right) \tag{4.1}$$

These A values and the particle mass concentration, C_m, obtained from the filter samplers were then used to calculate the σ_m value based on Beer's law, which relates the optical measurement to the C_m of the obscurant (Smith, 1996):

$$\sigma_{m_{(\lambda)}} = \frac{2.303 A_{(\lambda)}}{C_m L} \tag{4.2}$$

where λ is wavelength and L is the path length.

The calculated σ_m values "after dispersion" (i.e., t = 1 min after dispersion) and "after particle sampling" (i.e., t = 3 min after dispersion) were averaged to get the "mean σ_m" value. This value was considered equivalent to time 2 min after dispersion when the C_m and aerodynamic diameter were measured simultaneously. The "mean σ_m" values for the 3 - 5 µm (433 readings) and for the 8 - 12 µm (1389 readings) wavebands were calculated. The σ_v value was obtained by multiplying the σ_m value and the tap density:

$$\sigma_{v(\lambda)} = \sigma_{m(\lambda)} \cdot (\text{tap density}) \tag{4.3}$$

In addition, the overall mean σ_m and σ_v values were obtained by averaging the "mean σ_m" and "mean σ_v" values for the 3 - 5 and 8-12 µm wavelengths.

Data were analyzed statistically using SAS (version 9.1, SAS Institute Inc., Cary, NC). The PROC GLM procedure and correlation analysis were used to determine the effect of the type of particles, concentration, and diameter on extinction coefficients. The means were also

compared at $\alpha = 0.05$ using the Tukey's Studentized Range and Scheffe's Test for equal and unequal number of replications.

4.4 Results and Discussion

4.4.1 Mass extinction coefficients

The σ_m values of the different particles are shown in Figures 4.6 and 4.7. The reference particles (i.e., brass flakes, graphite flakes, and carbon black) showed nearly constant values of σ_m throughout the 3-12 μm wavelength range (Fig. 4.6). This trend was similar to those in previous studies (Appleyard, 2006; Owrutsky et al., 2001; Wetmore and Ayres, 2000). In contrast, the σ_m values of the nanostructured and conventional particles varied considerably with wavelength. These trends were similar to those of many military obscurants, including red phosphorus and fog oil (Milham, 1976; Farmer, 1991). Within the 4.1-4.4 μm wavelength range, the IR absorption of CO_2 can be observed (Milham, 1976). In the wavelength range between 5 and 8 μm, the collective absorption of water vapor, CO_2, and other gases can be observed as indicated by fluctuations in σ_m with wavelength (Bailey et al., 2002). The σ_m values of the nanorods as compared to NanoActive® particles are shown in Figure 4.7. It was theoretically predicted that high aspect ratio particles such as nanorods would enhance the extinction coefficient of the materials. This was observed for MgO but not for TiO_2 nanorods. This is probably due to the higher aspect-ratio (length/width) of MgO nanorods (~14) than TiO_2 nanorods (~10) (Table 4.1).

Table 4.2 summarizes the mean values of the band-averaged σ_m, mass dispersed, and mass concentrations of the particles. The reference particles had the greatest band-averaged σ_m values. The mean σ_m values for the 3-5 μm waveband for brass flakes, graphite flakes, and carbon black were 1.44 (s.d. = 0.34), 3.03 (s.d. = 0.40), and 1.89 (s.d. = 0.31) m^2/g, respectively;

those for the 8-12 μm waveband were 1.62 (s.d. = 0.37), 3.31 (s.d. = 0.41), and 1.66 (s.d. = 0.45) m^2/g, respectively. Wetmore and Ayres (2000) cited a σ_m value of 2 m^2/g for both the 3-5 μm and 8-12 μm wavebands for graphite flakes. Owrutsky et al. (2000 and 2001) reported smaller σ_m values for brass flakes (0.34 m^2/g and 0.33 m^2/g for 3-5 μm and 8-12 μm waveband, respectively), graphite flakes (0.74 m^2/g and 0.73 m^2/g for 3-5 μm and 8-12 μm waveband, respectively), and carbon black (0.83 m^2/g and 0.62 m^2/g for 3-5 μm and 8-12 μm waveband, respectively). Differences between the measured values in this study and to other published values could be due to differences in the properties of particles used (i.e., mean particle size, shape, morphology) and measurement methods.

Of the nanostructured and conventional particles considered, NanoActive® TiO_2 had the greatest mean σ_m value for the 3-5 μm waveband (Table 4.2). The mean σ_m value of NanoActive® TiO_2 in the 3-5 μm range (1.10 m^2/g, s.d. = 0.23), however, did not significantly differ (α=0.05) from those of the other nanostructured and conventional particles. As mentioned earlier, TiO_2 is a semiconductor and was expected to exhibit good extinction performance. For the 8-12 μm wavelength region, the ISO fine test dust had the greatest mean σ_m value (0.75 m^2/g, s.d. = 0.03); however, the mean σ_m value was not significantly different from those of the other particles. ISO fine test dust consists of several semiconductive elements such as silicates, aluminum, and iron (Vlasenko et al., 2005), and also has a flaky structure (Fig. 4.3). The MgO nanorods had higher but not significantly different σ_m value compared to NanoActive® MgO and MgO plus (Table 4.2).

Table 4.2 also summarizes the overall σ_m (combined σ_m values for the 3-5 and 8-12 μm wavebands). Graphite flakes had the greatest overall mean σ_m value (3.22 m^2/g, s.d. = 0.40),

followed by carbon black (1.72 m^2/g, 0.41), brass flakes (1.57 m^2/g, 0.38), and ISO fine test dust (0.74 m^2/g, 0.03).

4.4.2 Volume extinction coefficients

Figures 4.8 and 4.9 show the σ_v values of the particles for the 3-12 μm wavelength range. Table 4.3 summarizes the mean values of the band-averaged σ_v and tap densities of the particles. $NaHCO_3$ (1.39 g/cc, s.d. = 0.001), ISO fine test dust (1.22 g/cc, s.d. = 0.00), and brass flakes (1.05 g/cc, s.d. = 0.006) had the largest tap densities.

The reference particles showed near constant σ_v values, however, both graphite flakes and carbon black showed marked decreases in σ_v values (~75 to 78% decrease compared with their corresponding σ_m values) due to their low tap densities (Fig. 4.8; Table 4.3). The brass flakes sample, on the other hand, maintained its extinction coefficient value because of its high tap density (1.05 g/cc). For both the MgO nanorods and TiO_2 nanorods, the values of σ_v were slightly smaller than those for similar materials in conventional nanostructured form; this may be due to their lower tap densities (Fig. 4.9; Table 4.3).

For the 3-5 μm wavelength region, brass flakes had the highest σ_v value (1.5 m^2/cc, s.d. = 0.36) (Table 4.3). This was followed by the two conventional particles, $NaHCO_3$ (1.01 m^2/cc, s.d. = 0.16) and ISO fine test dust (0.87 m^2/cc, s.d. = 0.02), and NanoActive® TiO_2 (0.88 m^2/cc, s.d. = 0.19). For 8-12 μm waveband, brass flakes also had the highest value (1.69 m^2/cc, s.d. = 0.40). The next highest σ_v values were those of ISO fine test dust (0.91 m^2/cc, s.d. = 0.04), $NaHCO_3$ (0.89 m^2/cc, s.d. = 0.13), and graphite flakes (0.82 m^2/cc, s.d. = 0.10). The nanostructured MgO particles had the smallest σ_v values for both wavebands. For the overall σ_v, brass flakes had the greatest overall mean σ_v values (1.64 m^2/cc, 0.39), followed by $NaHCO_3$ (0.93 m^2/cc, 0.12), ISO fine test dust (0.91 m^2/cc, 0.03), and graphite flakes (0.80 m^2/cc, 0.10).

The extinction coefficients of the nanorods (MgO and TiO_2) and the NanoActive® materials were generally significantly smaller than those of the reference and conventional particles.

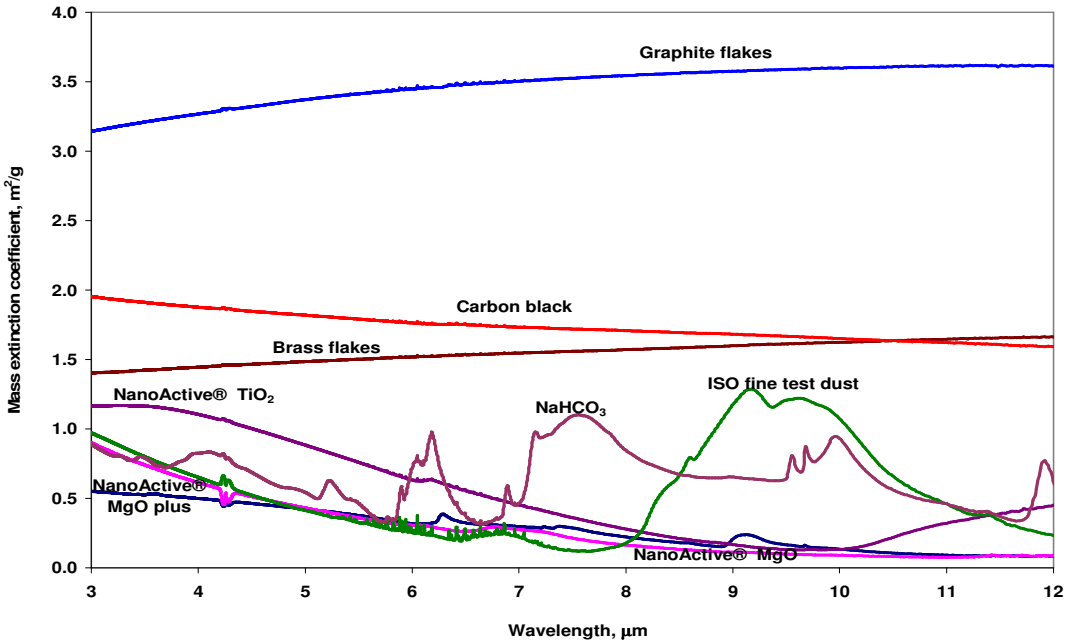

Figure 4.6. Mass extinction coefficients of the particles. Each spectrum represents the mean of three replicates.

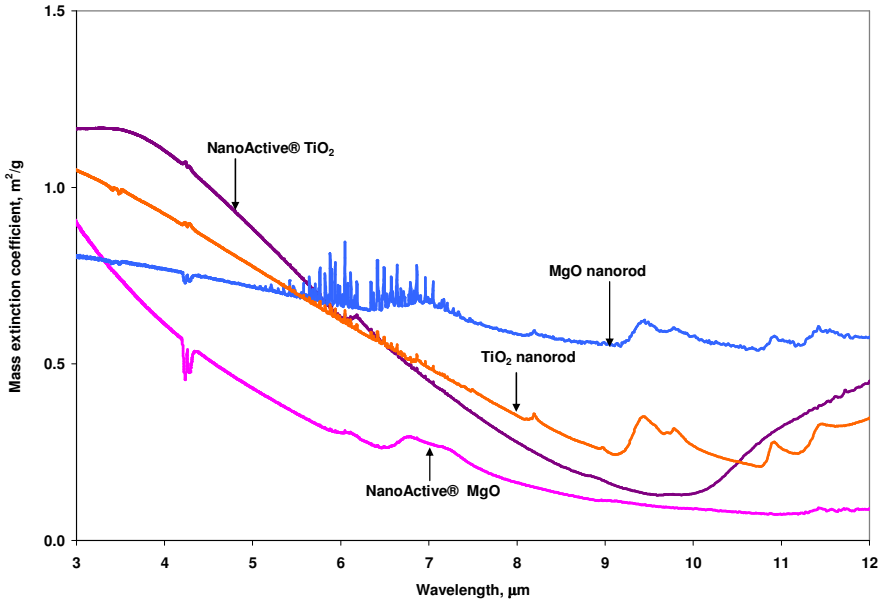

Figure 4.7. Comparison of the mass extinction coefficients of the NanoActive® particles and nanorods. Each nanorod spectrum represents the mean of two replicates.

Table 4.2. Band-averaged mass extinction coefficients, mass dispersed, and mass concentrations of particles. Each value represents the mean of three replicates.

Particle	Mass extinction coefficient, m^2/g						Mass dispersed, g		Mass concentration, g/m^3	
	3-5 µm		8-12 µm		Overall					
	Mean[a]	s.d.	Mean[a]	s.d.	Mean[a]	s.d.	Mean	s.d.	Mean	s.d.
NanoActive® particles										
NanoActive® MgO plus	0.50 (d)	0.05	0.15 (c)	0.01	0.23 (d)	0.01	3.04 (a)	0.01	1.7 (abc)	0.27
NanoActive® MgO	0.67 (cd)	0.02	0.10 (c)	0.10	0.24 (d)	0.02	2.39 (a)	0.25	0.96 (bc)	0.13
NanoActive® TiO_2	1.10 (bcd)	0.23	0.23 (c)	0.05	0.43 (d)	0.09	2.50 (a)	0.41	1.6 (abc)	0.41
Conventional particles										
$NaHCO_3$	0.76 (cd)	0.09	0.64 (c)	0.06	0.67 (d)	0.08	2.85 (a)	0.18	1.56 (abc)	0.42
ISO Fine test dust	0.71 (cd)	0.01	0.75 (bc)	0.03	0.74 (cd)	0.03	2.50 (a)	0.05	0.76 (bc)	0.08
Reference obscurants										
Brass flakes	1.44 (bc)	0.34	1.62 (b)	0.37	1.57 (bc)	0.38	3.01(a)	0.00	2.62 (a)	0.26
Graphite flakes	3.03 (a)	0.40	3.31 (a)	0.41	3.22 (a)	0.40	2.99 (a)	0.03	2.15 (ab)	0.38
Carbon black	1.89 (b)	0.31	1.66 (b)	0.45	1.72 (b)	0.41	2.85 (a)	0.08	2.04 (ab)	0.45
Nanorods										
MgO nanorods	0.78 (cd)	0.12	0.57 (c)	0.31	0.62 (d)	0.21	1.19 (b)	0.17	0.51 (c)	0.43
TiO2 nanorods	1.00 (cd)	0.14	0.23 (c)	0.05	0.41 (d)	0.06	2.63 (a)	0.07	2.57 (a)	0.62

[a] Column means followed by the same letter are not significantly different at the 5% level.

Table 4.3. Band-averaged volume extinction coefficients and tap densities of particles. Each value represents the mean of three replicates.

Particle	Volume extinction coefficient, m^2/cc						Tap density, g/cc	
	3-5 µm		8-12 µm		Overall			
	Mean[a]	s.d.	Mean[a]	s.d.	Mean[a]	s.d.	Mean[a]	s.d.
NanoActive® particles								
NanoActive® MgO plus	0.33 (cd)	0.04	0.10 (c)	0.01	0.16 (d)	0.01	0.65 (g)	0.00
NanoActive® MgO	0.47 (cd)	0.02	0.07 (c)	0.01	0.17 (d)	0.01	0.71 (e)	0.00
NanoActive® TiO_2	0.88 (bc)	0.19	0.18 (c)	0.04	0.35 (d)	0.07	0.80 (d)	0.00
Conventional particles								
$NaHCO_3$	1.01 (ab)	0.16	0.89 (b)	0.13	0.93 (b)	0.12	1.39 (a)	0.00
ISO Fine test dust	0.87 (bc)	0.02	0.91 (b)	0.04	0.91 (b)	0.03	1.22 (b)	0.00
Reference obscurants								
Brass flakes	1.50 (a)	0.360	1.69 (a)	0.40	1.64 (a)	0.39	1.05 (c)	0.01
Graphite flakes	0.75 (bc)	0.100	0.82 (b)	0.10	0.80 (bc)	0.10	0.25 (h)	0.00
Carbon black	0.42 (cd)	0.070	0.37 (bc)	0.10	0.38 (bcd)	0.09	0.22 (i)	0.00
Nanorods								
MgO nanorods	0.08 (d)	0.01	0.06 (c)	0.03	0.06 (d)	0.02	0.10 (j)	0.00
TiO_2 nanorods	0.68 (bc)	0.09	0.16 (c)	0.03	0.28 (d)	0.04	0.68 (f)	0.02

[a] Column means followed by the same letter are not significantly different at the 5% level.

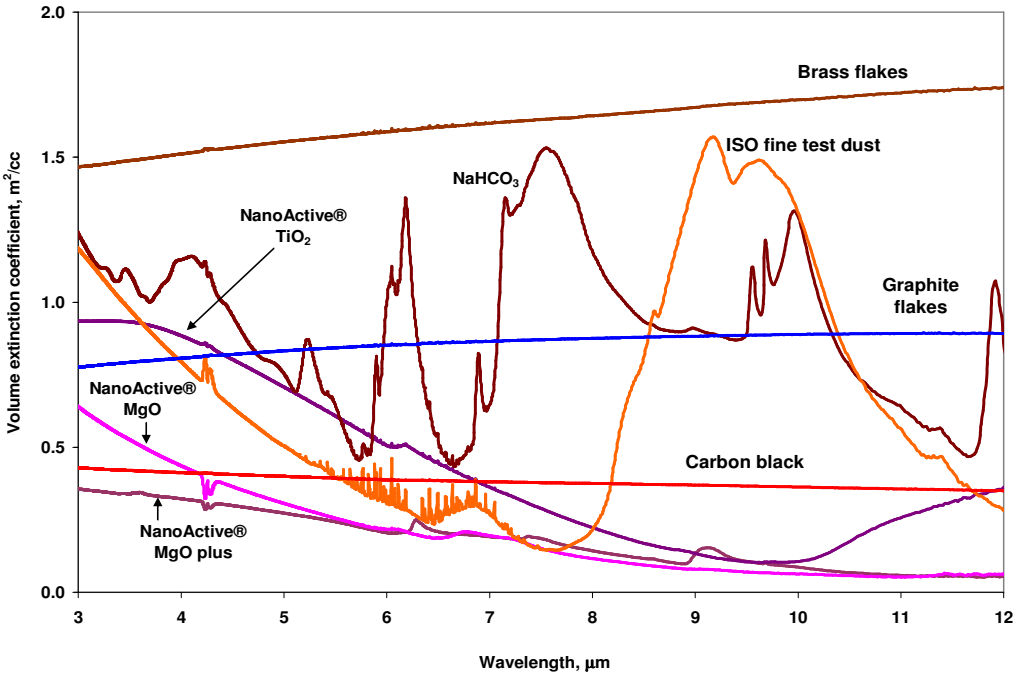

Figure 4.8. Volume extinction coefficients of the different particles. Each spectrum represents the mean of three replicates.

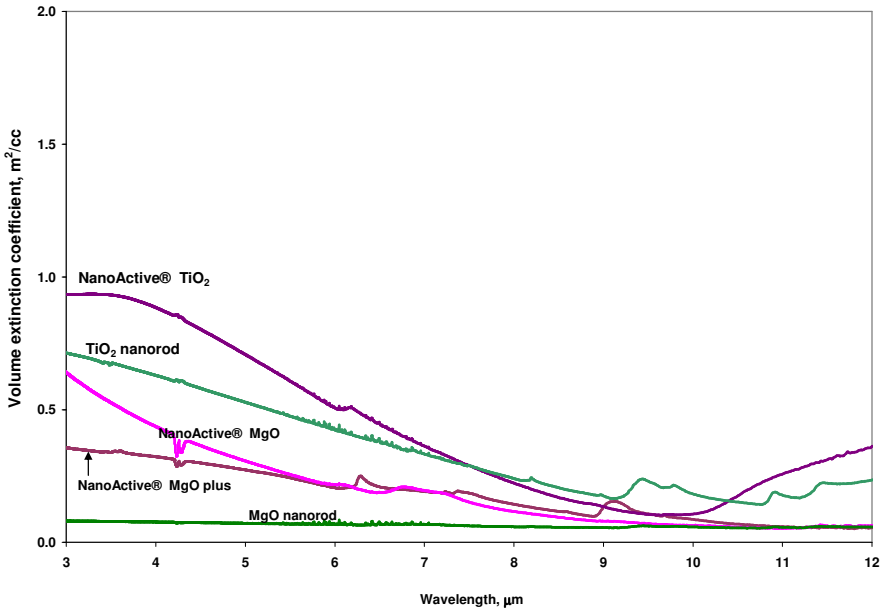

Figure 4.9. Comparison of the volume extinction coefficients of the NanoActive® particles and nanorods. Each nanorod spectrum represents the mean of two replicates.

4.4.3 Effect of particle size distribution and concentration

Figure 4.10 shows the particle size distributions at time 1 min after dispersion. The values of GMD, GSD, mass concentration, and number concentration are shown in Table 4.4. NanoActive® MgO plus had the highest GMD value of 8.32 μm (s.d. = 0.25). NanoActive® MgO had a wider size distribution (GSD=2.61, s.d. = 0.12) and the highest particle number concentration (403,333 particles/cc, s.d. = 13051). $NaHCO_3$ had the highest mass concentration (1,777 mg/m^3, s.d. = 298).Statistical analysis showed that the GMD, GSD, and particle concentration did not have any significant effect on values of σ_m and σ_v.

Figures 4.11a and 4.11b present the temporal change in particle number and mass concentrations, respectively. NanoActive® MgO and carbon black showed the greatest number concentrations (Fig. 11a). This might be due to their small individual particle size (Table 4.1). Brass showed the lowest number concentration probably due to the clumping of individual, thread-like particles that form its flaky morphology. For most of the particles, the concentrations decreased by up to 50% of their initial number concentrations at time between 3 and 5 min after dispersion. The extinction measurement in this study was between time 1 and 3 min after dispersion. In terms of mass concentration (Fig. 4.11b), $NaHCO_3$ and NanoActive® MgO plus had the highest mass concentration but at the same time had the fastest decrease in concentration. Brass flakes had the lowest mass concentration, but showed the slowest decay rate. The mass concentration of all particles was below 500 mg/m^3 at time 5 min after dispersion.

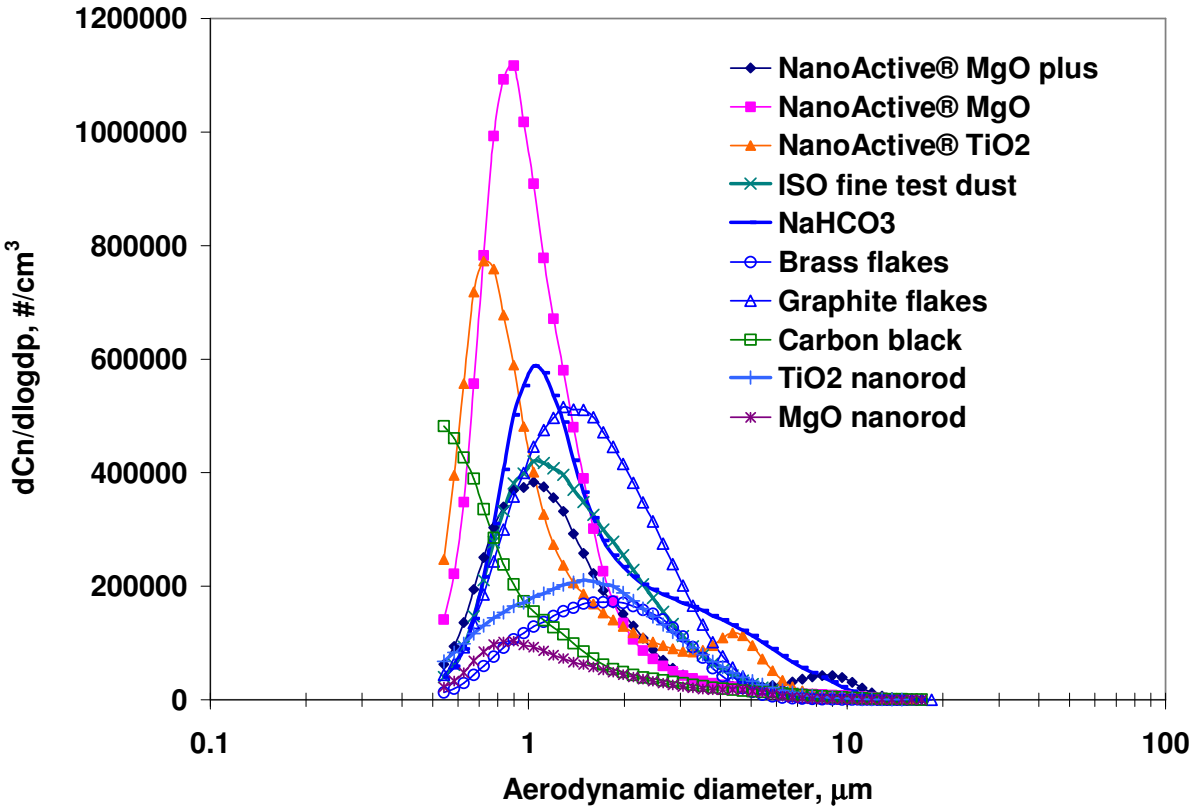

Figure 4.10. Particle size distribution of the particles at time 1 minute after dispersion. Each curve represents the mean of three replicates, except for the curves of the nanorods which represent two replicates.

Table 4.4. Overall mean values and standard deviations of extinction coefficients, GMD, GSD, and mass and number concentrations of the particles at time 2 minutes after dispersion. Each value represents the mean of three replicates.

Particles	Overall σ_m		Overall σ_v		GMD, µm		GSD		Mass Conc., mg/m^3		Number Conc., #/cc	
	Mean[a]	s.d.	Mean[a]	s.d.	Mean[a]	s.d.	Mean[a]	s.d.	Mean[a]	s.d.	Mean[a]	s.d.
NanoActive® particles												
NanoActive® MgO plus	**0.23 (d)**	0.01	**0.16 (d)**	0.01	**8.32 (a)**	0.25	**1.65 (c)**	0.05	**1453 (ab)**	185	**123667 (ab)**	19502
NanoActive® MgO	**0.24 (d)**	0.02	**0.17 (d)**	0.01	**4.86 (cd)**	0.49	**2.61 (a)**	0.12	**423 (bc)**	108	**403333 (a)**	13051
NanoActive® TiO_2	**0.43 (d)**	0.09	**0.35 (d)**	0.07	**4.87 (cd)**	0.68	**1.84 (bc)**	0.01	**639 (bc)**	304	**229667 (ab)**	24502
Conventional particles												
$NaHCO_3$	**0.67 (d)**	0.08	**0.93 (b)**	0.12	**5.89 (bc)**	0.13	**1.74 (c)**	0.03	**1777 (a)**	298	**234667 (ab)**	25697
ISO Fine test dust	**0.74 (cd)**	0.03	**0.91 (b)**	0.03	**3.73 (cd)**	0.58	**1.87 (bc)**	0.01	**403 (bc)**	56	**137000 (ab)**	21656
Reference obscurants												
Brass flakes	**1.57 (bc)**	0.38	**1.64 (a)**	0.39	**3.23 (d)**	0.28	**1.63 (c)**	0.05	**140 (c)**	74	**58067 (b)**	11686
Graphite flakes	**3.22 (a)**	0.40	**0.80 (bc)**	0.10	**3.87 (cd)**	0.35	**1.92 (bc)**	0.06	**810 (abc)**	669	**190367 (ab)**	158214
Carbon black	**1.72 (b)**	0.41	**0.38 (bcd)**	0.09	**7.47 (ab)**	0.73	**2.11 (b)**	0.14	**521 (bc)**	60	**354000 (ab)**	149171
Nanorods												
MgO nanorods	**0.62 (d)**	0.21	**0.06 (d)**	0.02	**2.43 (bcd)**	3.26	**0.94 (bc)**	1.28	**147 (c)**	129	**55750 (b)**	40234
TiO_2 nanorods	**0.41 (d)**	0.06	**0.28 (d)**	0.04	**4.56 (cd)**	0.92	**1.80 (c)**	0.13	**236 (c)**	144	**81050 (b)**	42356

[a] Column means followed by the same letter are not significantly different at the 5% level.

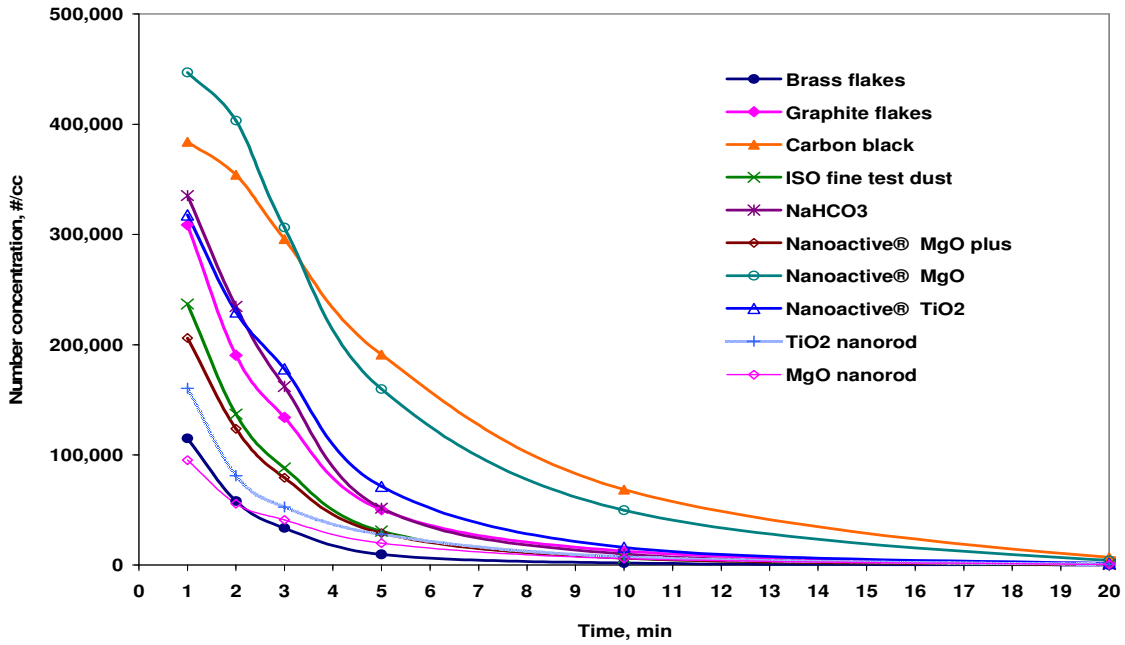

(a)

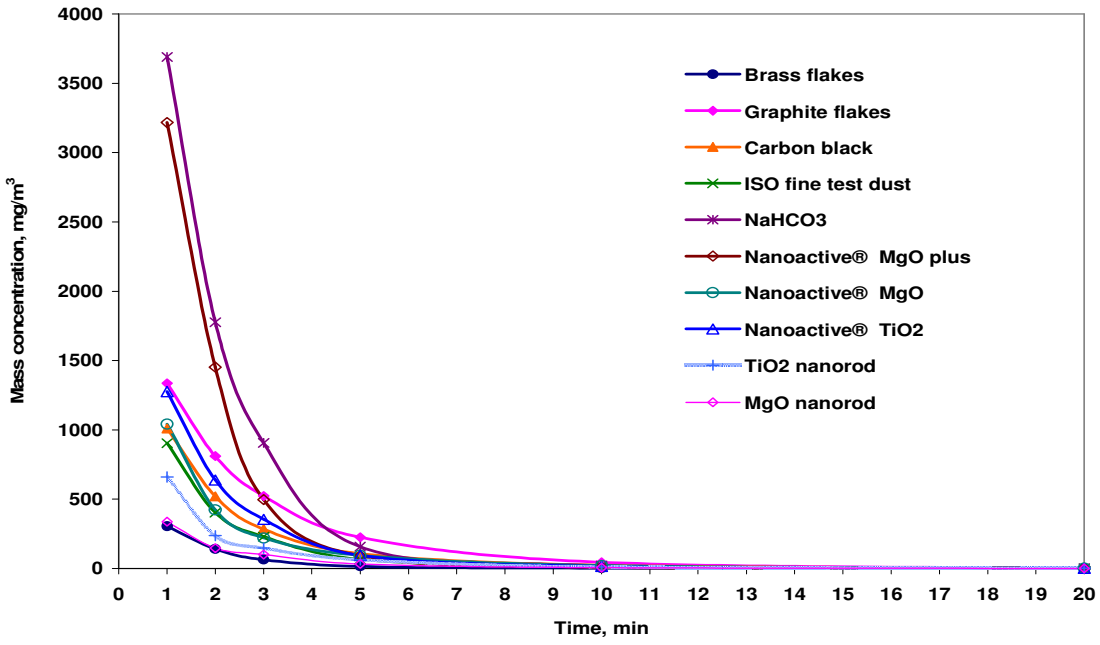

(b)

Figure 4.11. Number (a) and mass (b) concentrations of the particles. Each point in the curve represents the mean of three replicates, except for the nanorods which represent two replicates.

Results in this study generally agree with published data (Owrutsky et al., 2001; Appleyard and Davies, 2004b; Appleyard, 2006). Also, Appleyard and Davies (2004b) concluded that high-aspect ratio, highly conducting small particles (i.e., aluminum, brass) are excellent IR obscurants. In this study, brass flakes had the largest σ_v value and the third largest σ_m value (Table 4.4). The brass flake sample in this study has 69 – 91% copper and 29.5 – 7.5% zinc, which have electrical conductivity values of 100% IACS and 28% IACS, respectively. Aside from the high conductivity of brass flakes, the flake-like structure (~ 5 μm major diameter) with clumps of threadlike particles (thickness < 500 nm) (Fig. 4.4a) appears to be also important. These results agree with the theoretical results of Appleyard and Davies (2004b) and Appleyard (2006) that structures such as thin disk flakes and thin fibers have high extinction coefficients.

In this study, graphite flakes had the highest overall σ_m value (3.22 m^2/g), followed by carbon black (1.72 m^2/g), and brass flakes (1.57 m^2/g) (Table 4.4). Graphite and carbon black are composed of more than 99% carbon and have moderate to strong molecular vibrations in the IR region (Owrutsky et al., 2001; Stuart, 2004), but differ in morphology. Graphite has a flaky structure (Fig. 4.4a), while carbon black has a very small primary particle size (35 nm) and particles that seem to aggregate (Fig. 4.4c). Owrutsky et al. (2001) measured the σ_m and σ_v values for several powders as new obscurant candidate materials, including salts, semiconductors, and oxides. They reported that graphite had the largest value of σ_m but a lower value of σ_v than brass, similar to the findings in this study.

$NaHCO_3$ and ISO fine test dust have similar morphology consisting of smaller flat particles that are irregularly stacked upon each other (Fig. 4.3). The overall σ_m values of $NaHCO_3$ and ISO fine test dust were 0.67 m^2/g (s.d.=0.08) and 0.74 m^2/g (s.d.=0.03), respectively, which are smaller than those of the reference particles (Table 4.4). $NaHCO_3$ and

ISO fine test dust had larger packing densities and larger σ_v values than graphite and carbon black. Based on values of σ_v, ISO fine test dust and $NaHCO_3$ appear to be the most promising alternative to brass flakes. By manipulating the size and/or morphology of these two particles, it might be possible to enhance their IR extinction performance.

In general, the NanoActive® metal oxide particles (Fig. 4.2) had relatively poor IR extinction performance (Table 4.4). And with their relatively small packing density (<0.8 g/cm^3), the numerical values of σ_v were even smaller than that of σ_m. This agrees with the experimental results of Owrutsky et al. (2001); measured extinction coefficients of metal oxide particles, including titanium oxide, aluminum oxide, and manganese oxide were relatively small. It should be noted, however, that NanoActive® TiO_2 had relatively high value of σ_m in the 3-5 μm waveband. The nanorods (i.e., MgO and TiO_2 nanorods), similar to the nanostructured particles, had relatively poor IR extinction performance, even with their rod-like structure (Fig. 4.5). Appleyard and Davies (2004a) indicated that particles of insulating and semiconducting materials that are ionic and partially ionic possess extinction spectra that are particle size dependent, but relatively insensitive to particle geometry.

4.5 Conclusions

This research was conducted to identify effective obscurants in the mid-IR range in comparison to the common military IR obscurants such as brass flakes, graphite flakes, and carbon black. The following conclusions were drawn from this research:

1. Graphite flakes had the greatest overall mean mass extinction coefficient (3.22 m^2/g, s.d. = 0.40), followed by carbon black (1.72 m^2/g, 0.41), brass flakes (1.57 m^2/g, 0.38), and ISO fine test dust (0.74 m^2/g, 0.03). Brass flakes had the greatest overall mean volume extinction coefficient (1.64 m^2/cc, 0.39), followed by $NaHCO_3$ (0.93

m^2/cc, 0.12), ISO fine test dust (0.91 m^2/cc, 0.03), and graphite flakes (0.80 m^2/cc, 0.10). The geometric mean diameter, geometric standard deviation, and particle concentration did not have any significant effects on the values of σ_m and σ_v. It appears that high-aspect ratio (i.e., thin disk flakes, thin fibers) and high conductivity are the main contributing factors to high IR extinction coefficients.

2. The extinction coefficients of the nanorods (MgO and TiO_2) and the NanoActive® materials were generally significantly smaller than those of the reference and conventional particles. NanoActive® TiO_2 did have relatively high value of σ_m in the 3-5 μm waveband.
3. Based on the values of volume extinction coefficient ISO fine test dust and $NaHCO_3$ appeared to be the most promising alternative to brass flakes. By manipulating the size and/or morphology of these particles, it might be possible to enhance their IR extinction performance.

4.6 References

Appleyard, P. G. 2006. Infrared extinction performance of high aspect ratio carbon nanoparticles. *Journal of Optics A-Pure and Applied Optics* 8(2): 101-113.

Appleyard, P. G. 2007. Modelled infrared extinction and attenuation performance of atmospherically disseminated high aspect ratio metal nanoparticles. *Journal of Optics A-Pure and Applied Optics* 9: 278-300.

Appleyard, P. G. and N. Davies. 2004a. Calculation and measurement of infrared mass extinction coefficients of selected ionic and partially ionic insulators and semiconductors: a guide for infrared obscuration applications. *Optical Engineering* 43(2): 376-386.

Appleyard, P. G. and N. Davies. 2004b. Modelling infrared extinction of high aspect ratio, highly conducting small particles. *Journal of Optics A-Pure and Applied Optics* 6(10): 977-990.

ASTM Standards. 2006. B 527-93: Standard test method for determination of tap density of metallic powders and compounds. Philadelphia, PA: ASTM.

Bailey, R. A., H. M. Clark, S. Krause, J. P. Ferris and R. L. Strong. 2002. *Chemistry of the environment.* 2nd ed. New York, NY: Elsevier.

Butler, B.A. 1998. Smoke and obscurant operations in adjoint environments. Unpublished Thesis. Maxwell Air Force Base, AL.

Colbeck, I., B. Atkinson, and Y. Johar. 1997. The morphology and optical properties of soot produced by different fuels. *Journal of Aerosol Science* 28(5): 715-723.

Dobbins, R. A., G. W. Mulholland, and N. P. Bryner. 1994. Comparison of a fractal smoke optics model with light extinction measurements. *Atmospheric Environment* 28(5):889-897.

Farmer, W. M. 1991. Prediction of broad-band attenuation computed using band-averaged mass extinction coefficients and band-averaged transmittance. *Optical Engineering* 30(9): 1255-1261.

Farmer, W. M. and K. L. Krist. 1981. Comparison of methods used to determine the mass extinction coefficient for phosphorous smokes. *Proceedings of the Society of Photo-Optical Instrumentation Engineers* 305: 7-16.

Farmer, W. M., F. A. Schwartz, R. D. Morris, M. A. Binkley, and L. M. Boyd. 1982. Optical characteristics at 3.4-um wavelength of munition-produced phosphorus smoke as a function of relative humidity. *Aerosol Science and Technology* 1(4): 409-425.

Haley, M.V. and Kurnas, C.W. 1993. Toxicity and fate comparison between several brass and titanium oxide powders. ERDEC-TR-094, Edgewood, MD: Edgewood Research and Development and Engineering Center.

Hutchison, K. D. and A. P. Cracknell. 2005. *Visible infrared imager radiometer suite: A new operational cloud imager.* New York, NY: Taylor & Francis.

Jacobson, M. Z. 1999. *Fundamentals of atmospheric modeling.* UK: Cambridge University Press.

Ladouceur, H. D., A. P. Baronavski, and H. H. Nelson. 1997. Obscurants for infrared countermeasures. Washington, DC: Naval Research Lab.

Milham, M. 1976. A catalog of optical extinction data for various aerosols/smokes. ED-8P-770022-85. Edgewood, MD: Edgewood Arsenal, Aberdeen Proving Ground.

Owrutsky, J. C., H. H. Nelson, H. D. Ladouceur, and A. P. Baronavski. 2000. Obscurants for infrared countermeasures II. Washington, DC: Naval Research Lab.

Owrutsky, J. C., D. A. Steinhurst, H. D. Ladouceur, H. H. Nelson, and A. P. Baronavski. 2001. Obscurants for infrared countermeasures III. Washington, DC: Naval Research Lab.

Shi, J. M., L. L. Chen, Y. S. Ling, and Y. Lu. 1998. Infrared extinction of artificial aerosols and the effects of size distributions. *International Journal of Infrared and Millimeter Waves* 19(12):1671-1679.

Shi, J. M., J. Y. Wang, B. Xu, J. C. Wang, and Z. C. Yuan. 2003. Calculation and optimization of the effective extinction cross section of the spherical cold obscuring smoke. *International Journal of Infrared and Millimeter Waves* 24(11): 2007-2013.

Singh, A., S. G. Avachat, and H. Singh. 1994. Infrared screening smokes - a review. *Journal of Scientific & Industrial Research* 53(9): 667-673.

Smith, B.C. 1996. *Fundamentals of fourier transform infrared spectroscopy*. Baton Roca, FL: CRC Press.

Stuart, B. 2004. *Infrared spectroscopy: Fundamentals and applications*. Chichester, England: J. Wiley and Sons, Ltd.

Thermo Electron Corporation. 2006. Nicolet^{TM} FT-IR User's Guide. Madison, WI.

Vlasenko, A., S. Sjogren, E. Weingartner, H.W. Gaggeler, and M. Ammann. 2005. Generation of submicron Arizona dust aerosol: chemical and hygroscopic properties. *Aerosol Science and Technology* 39:452-460.

Wang, J. Y., J. M. Shi, B. Xu, J. C. Wang, and Z. C. Yuan. 2004. Calculation of overall effective extinction cross section of several cold smoke infrared ammunitions. *Defense Science Journal* 54(3): 329-334.

Wetmore, A. and S. D. Ayres. 2000. Combined obscuration model for battlefield induced contaminants. ARL-TR-1831-2 Vol. 2. Adelphi, MD: Army Research Laboratory.

Widmann, J. F., J. C. Yang, T. J. Smith, S. L. Manzello, and G. W. Mulholland. 2005. Measurement of the optical extinction coefficients of post-flame soot in the infrared. *Combustion and Flame* 134(1-2):119-129.

5. Relative Chargeability of Nanostructured and Conventional Particles by Tribocharging

5.1 Abstract

The relative chargeability of nanostructured particles by tribocharging was measured and compared with that of conventional particles. Particles were dispersed through a Teflon® tribocharger into an experimental room. The net charge-to-mass ratios of the dispersed particles were measured with a dynamic Faraday-cup sampler. Tribocharging with a Teflon® charger was able to charge the particles positively. NanoActive® TiO_2 gained the highest net charge-to-mass ratio (1.21 mC/kg, s.d. = 0.07) followed by NanoActive® MgO (0.81 mC/kg, s.d.=0.12) and ISO fine test dust (0.66 mC/kg, s.d.= 0.13). These net charge-to-mass ratios, however, were small compared to the Gaussian limit (<8%). Results suggest that tribocharging may not a feasible method of imparting significant charge to the nanostructured particles.

5.2 Introduction

Nanostructured particles, because of their high surface area and unique morphology, have several potential uses. Metal oxide nanostructured particles, for example, have been shown to be effective in inactivating chemical warfare and biological agents, detoxifying industrial chemicals, and decontaminating indoor spaces (Stoimenov et al., 2002; Richards et al., 2000). By manipulating and controlling the electrostatic charge of nanostructured particles, their effectiveness might be enhanced.

Tribocharging is a method that can be used to charge particles and is employed in the powder coating industry. In this method, electrostatic charge is transferred from one material to

another when they touch or rub together (Lowell and Rose-Innes, 1980). In general, materials that are able to lose electrons have lower work functions than materials that gain electrons. A work function is defined as the energy required for moving an electron from Fermi level (the highest occupied energy level at 0 K) to the free state (Tianxiang, 1999). Work functions depend not only on the internal structure of materials, but also on their surface contamination. The drawback is that for most materials, work function values are not available (Tianxiang, 1999). However, relative work functions can be predicted qualitatively if charge polarities and magnitudes of contact materials are known.

Surface contact is a major contributing factor in tribocharging. The greater the surface contact, the greater is the resulting net charge. On the surface of a dielectric material, the positions of the static charges are fixed and therefore, the charge separation between either a metal and a dielectric or two dielectrics must depend upon the actual area of contact (Schnurmann, 1941). Surface chemistry (e.g., surface composition, contamination, and oxidation) was also determined to control partly the amount and polarity of charge transferred between two dissimilar materials, such as metals and polymer powder (Mazumder et al., 2006; Trigwell, 2003; Trigwell et al. 2003; Sharma et al., 2004).

Powders having a low bulk density resistivity, 10^7-10^9 Ohm-m, can be used successfully with electrostatic guns only for small particles (~5 μm) due to charge and particle loss while resistivities > 10^{12} Ohm-m are desirable for use with larger particles. One rule of significant charging is that at least one of the materials should have a bulk resistivity > 10^7 Ohm-m (Colver, 1999). Permittivity is another parameter influencing the charging process between two solid materials. It is a measure of the ability of the material to become polarized. Coehn's law states

that when two materials are in contact with each other, the one with the highest permittivity becomes positive (Tianxiang, 1999).

Charge backflow is another phenomenon that happens when, upon separation in tribocharging, some electrons will drive back under the action of a potential difference between the materials. Fast separation or longer charge relaxation time results in lower charge backflow. A material of high conductivity or low permittivity has a short charge relaxation time, resulting in high charge backflow (Tianxiang, 1999). Another factor is the gas breakdown or gaseous discharge during separation and it can be in the form of sparks. Ambient conditions, especially humidity, can decrease the surface and volume resistivities of materials, and therefore affect the characteristics of tribocharging (Banerjee and Law, 1995).

Trigwell et al. (2003) performed experiments on different powders of different size distributions tribocharged by milling with stainless steel beads. Results showed that the charge acquired by the powder could be correlated with the actual work function difference between the powder and the stainless steel. Using ultraviolet and x-ray photoelectron spectroscopy, experiments performed on various materials showed that work functions increased with surface contamination and oxidation. Moreover, their results showed that while charge acquired increased with particle size, the charge distribution was generally bipolar.

Tianxiang (1999) investigated the particle charge and charge exchange related to triboelectric beneficiation of physical mixtures of fine particles (i.e., silica beads). The magnitude of charge and charge exchanged were measured by the Faraday cup and laser Phase Doppler Particle Analyzer. In the experiment, charging velocity and charging duration were the most important factors affecting tribocharging. Tianxiang (1999) also observed that the charge on the particle surface could become saturated well below a theoretical maximum charge limit

due to charge backflow. Tianxiang (1999) predicted qualitatively the relative work functions of lunar minerals based on charge polarity and magnitude.

Banerjee and Law (1995) studied the triboelectric chargeability of pecan pollen and lycopodium using commercial Teflon® and nylon chargers. The pecan pollen and lycopodium have bimodal size distributions with diameters of 0-15 µm or 40-50 µm and 5-10 µm or 20-30 µm, respectively. Their results indicated that tribocharging is a feasible method of imparting charge to pollen in electrostatic pollination technology.

One challenge in charging nanoparticles is their small size. Flagan (2001) mentioned that the probability of charging decreases with decreasing particle size and that large particles frequently acquire multiple charges. He also added that particles in aerosolized form usually carry only a small number of elementary charges.

This study was conducted to measure the relative chargeability by tribocharging of nanostructured particles and compare them to conventional particles. By manipulating the charge of particles (e.g., by tribocharging), their effectiveness in such applications as smoke clearing may be enhanced.

5.3 Materials and Methods

5.3.1 Test particles

The particles tested included three nanostructured metal oxide particles (i.e., NanoActive® MgO plus, NanoActive® MgO, and NanoActive® TiO_2), two conventional particles (i.e., $NAHCO_3$ and ISO fine test dust), and an electrostatic-grade nylon powder. The nylon powder (Thermoclad Company PC, Erie, PA) was used as the reference. The size of the nylon particles, however, was large compared to the test particles. Table 5.1 shows the properties of the particles used in the study.

Table 5.1. Properties of particles.

Particles types	Equivalent aerodynamic diameter[a], µm	Actual particle diameter, µm	True density[c], kg/m^3	Surface area[d], m^2/g	Major metal component
Nanostructured particles					
NanoActive® MgO plus	8.6	5.5	2420	≥600	Magnesium
NanoActive® MgO	6.4	3.5	3440	≥230	Magnesium
NanoActive® TiO_2	5.2	2.7	3640	≥500	Titanium
Conventinal fine particles					
$NaHCO_3$	6.3	3.8	2760	--	Sodium
ISO fine test dust	4.4	2.9	2270	--	Silicon Aluminum
Reference particle					
Nylon powder (Nylon 11)	--	63[b]	--	--	--

[a]Source: Measured using Aerodynamic Particle Sizer® (APS)

[b]Source: Thermoclad Co., Erie, PA

[c]Source: Measured using multipycnometer.

[d]Source: Nanoscale Corp., Manhatan, KS

5.3.2 Tribocharger

The tribocharger (Fig. 5.1) is the charge tube module of the commercially-available Nordson® tribomatic/tribogun system (Nordson Corporation, Westlake, OH). Particles pass though the annulus of the charge tube module and come in contact to its corrugated surface. The charging tube is made of Teflon®, which is a preferred material by the powder coating industry since it has very low friction, wears well, and strongly resists being coated by the powder material (Liberto, 1994).

5.3.3 Charge measurement

Two charge measurement devices were developed based on the classical Faraday cup principle and the guidelines of ASTM Standard D4470-97 (ASTM Standards, 1997). The first charge measurement device (Fig A.6) provided only qualitative data and cannot be used to

measure mass of particles, which is necessary to obtain the net charge-to-mass (q/m) ratio. The second charge measurement device, the dynamic Faraday-cage sampler (Figs. 5.2 and 5.3), was used in this research. The calibration of the device is described in Appendix B.

The design of the dynamic Faraday-cage sampler is similar to previous designs (John, 1980; Greaves and Makin, 1980; Tardos et al., 1984; Tucholski and Colver, 1993; Hinds and Kennedy, 2000; Mutomaa, 2002). The sampler consists of an outer metal shield and an inner conducting metal that has a back-up metal screen at the bottom for holding the particulate collection filter. The outer enclosure is connected to an electrometer (Model 6514, Keithley Instruments Inc., Cleveland, OH) and serves to shield the filter holder from external fields. The inner metal and the back-up metal screen are electrically connected to the electrometer Hi input. The device is connected to a low-volume sampling pump that draws air and particles into the device. Particles are collected on the filter, which is weighed before and after sampling. The electrometer is controlled using the Excelinx software (Keithley Instruments Inc., Cleveland, OH).

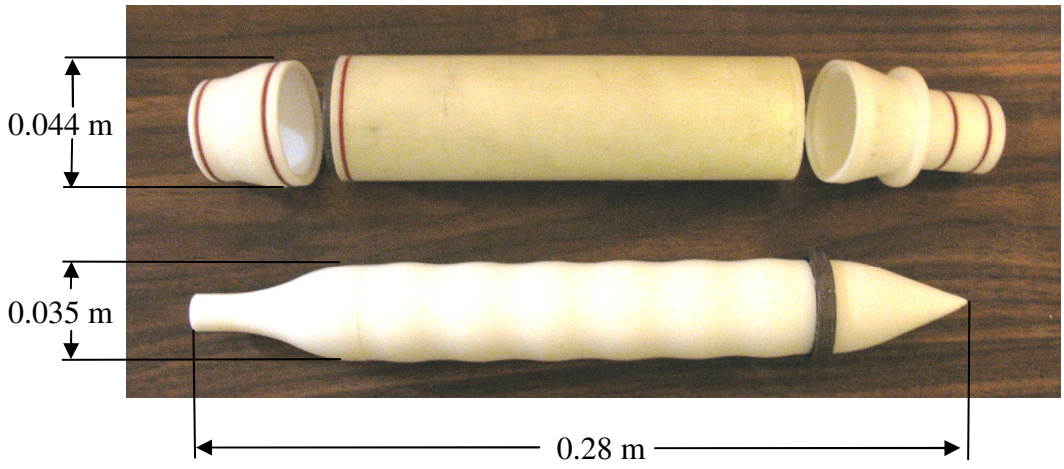

Figure 5.1 Photograph of the Teflon® charging tube.

5.3.4 Experimental procedure

Experiments were conducted in a test room 3.6 m long, 2.4 m wide, and 2.4 m high. The tribocharger was located at one side of the chamber). A powder disperser with copper tube nozzle was used. The tribocharger was connected to the copper tube nozzle (Fig. 5.5). The powder disperser was also connected to the compressed nitrogen gas (40 psig), which was used to disperse the particles into the room. The dynamic Faraday-cage sampler was positioned near the center of the room or about 1.0 m to 1.5 m from the particle injection point (Fig. 5.4), depending on how far the particle cloud was dispersed especially during the first minute after dispersion. The electrometer and the sampling pump that were connected to the dynamic Faraday-cage sampler were started simultaneously approximately 10 sec before the dispersion of particles. Charged particles were collected on the filter for 60 sec. The temperature and the relative humidity inside the room were maintained at 25-26 °C and 50-51%, respectively.

Two sets of experiments were conducted for each particle. The first set involved the determination of the charge of the particles without the tribocharger. The charge measured is herein referred to as background charge, which represents the charge acquired by the particles as they are dispersed through the copper tube. The second set of experiments involved measurement of the charge of the particles with the Teflon® tribocharger in use. For each set of experiments, there were three replicates.

5.3.5 Data analysis

The (q/m) value was calculated by dividing the maximum charge measured by the electrometer after sampling by the mass of particles collected on the filter. The net q/m, $(q/m)_{net}$, value of the particles was obtained by subtracting the background (q/m) values (i.e., without tribocharger), $(q/m)_o$, from the (q/m) value of the tribocharged particles, $(q/m)_c$.

The maximum (q/m) value, $(q/m)_{max}$, attainable by solid particles charged by triboelectrification or the Gaussian limit was calculated using the following equation (Banerjee and Law, 1995; Tianxiang, 1999):

$$\left(\frac{q}{m}\right)_{max} = \frac{6\varepsilon_0 E_a}{\rho_p d_p} \tag{5.1}$$

where ε_o is the permittivity of free space (8.85×10^{-12} C/V-m), E_a is the maximum electric field strength (or the breakdown field strength) of air, which is approximately equal to 3 MV/m, ρ_p is the particle density, and d_p is the particle diameter.

The (q/m) data were analyzed statistically using the GLM procedure of SAS (version 9.1, SAS Institute Inc., Cary, NC) to determine the difference in charge acquired of the particles. To compare means, the Tukey's test at $\alpha = 0.05$ was used.

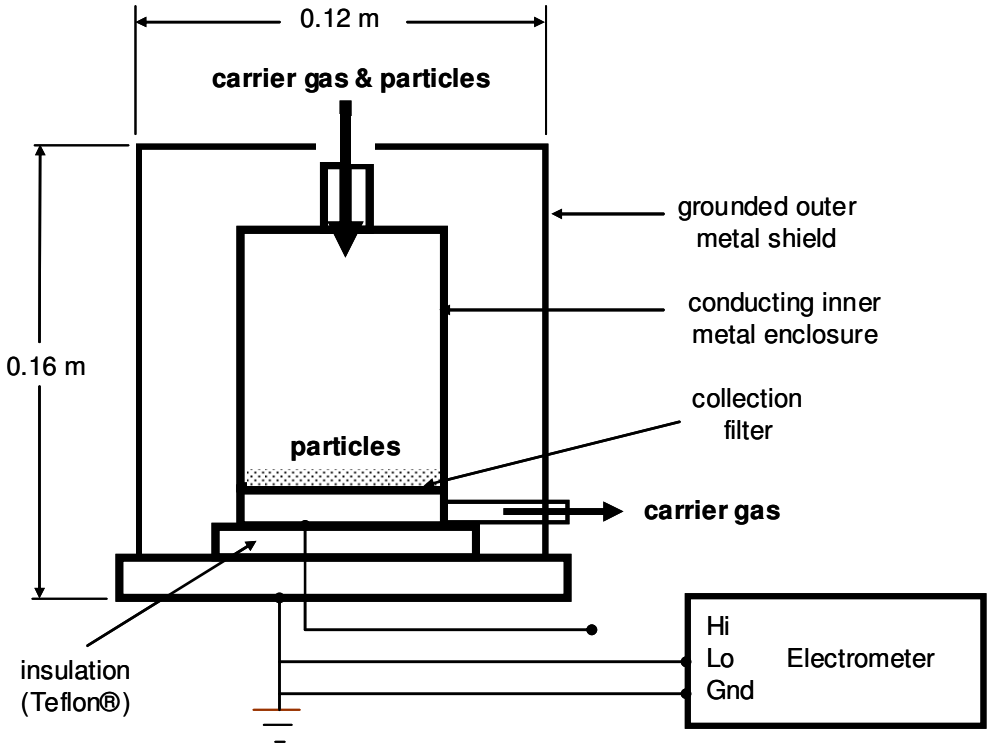

Figure 5.2. Schematic diagram of the dynamic Faraday-cage sampler for measuring the net charge-to-mass ratio of airborne particles.

Figure 5.3. Photograph of the dynamic Faraday-cage sampler. The top cover of outer metal shield was removed to show the inner conducting metal enclosure.

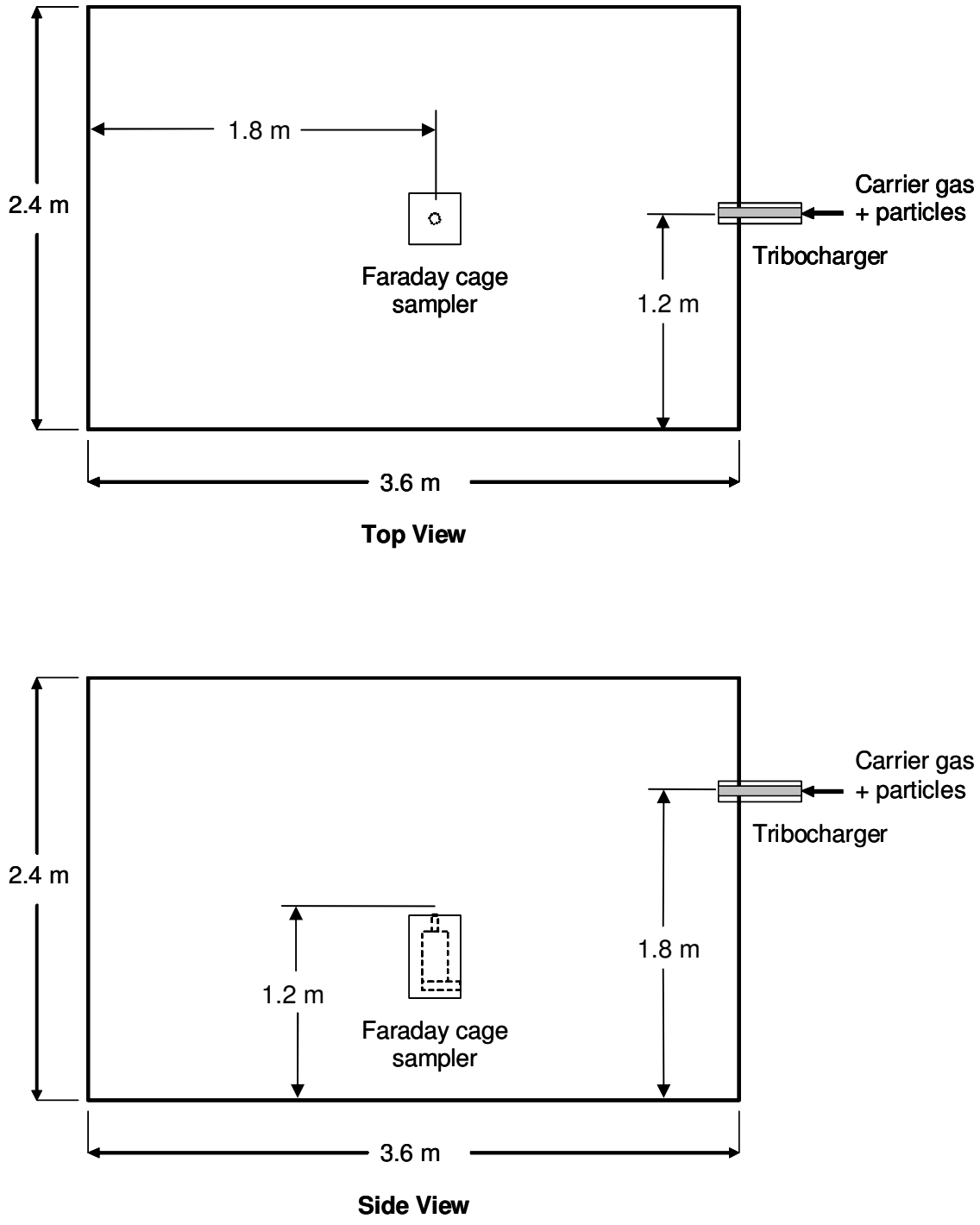

Figure 5.4. Schematic diagram of the experimental set-up (not drawn to scale).

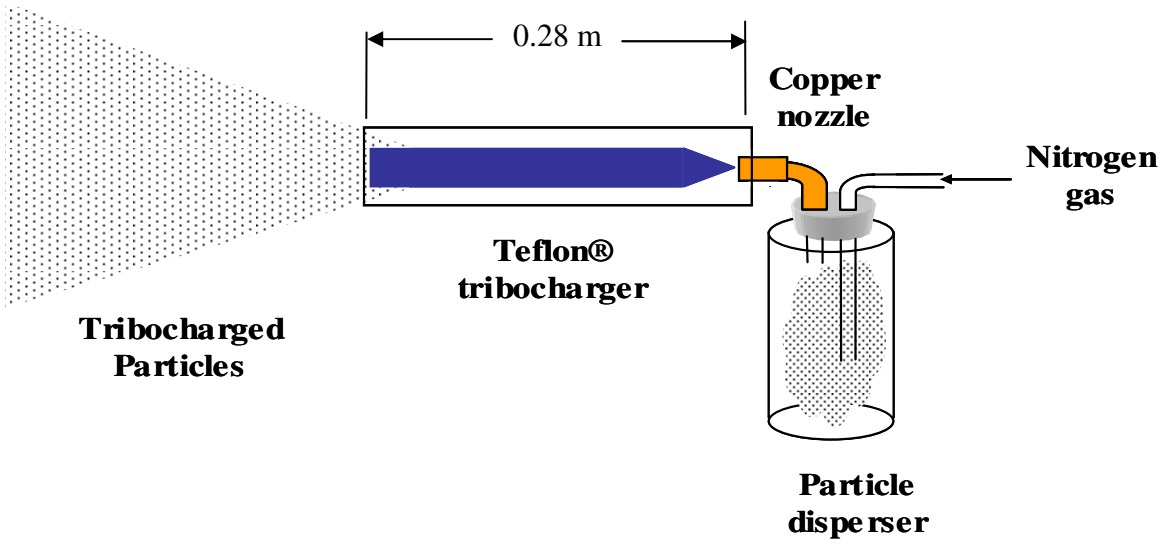

Figure 5.5. Schematic diagram of the powder disperser system and the tribocharger.

5.4 Results and Discussion

The measured background charges of the particles are shown in Figure 5.6. The ISO fine test dust showed positive background charge, while NanoActive® TiO_2 showed negative background charge. The other particles (i.e., nylon powder, NanoActive® MgO plus, NanoActive® MgO, and $NaHCO_3$) showed almost zero (neutral) background charge.

Figure 5.7 shows the charges as the tribocharged particles were being collected in the filter. Increasing charge values during sampling indicates that the particles are being collected in the filter. For the nylon powder, the measured charge was relatively small compared to the other particles. This could be due to the small amount of particles (<1.2 mg) collected on the filter as a result of the large diameter (63 µm), and consequently, large settling velocities of the particles. Table 5.2 summarizes the (q/m) values of the tribocharged particles in comparison to the background (q/m) values. Also shown are the $(q/m)_{net}$ and $(q/m)_{max}$ for each particle. Nylon powder and ISO fine test dust had the highest positive $(q/m)_o$ values compared to the other

particles. Nylon powder had a mean $(q/m)_o$ value of 0.30 (s.d. = 0.03) mC/kg while ISO fine test dust had a mean $(q/m)_o$ value of 0.20 (s.d. = 0.04) mC/kg. NanoActive® MgO plus, NanoActive® MgO, and $NaHCO_3$ had almost the same $(q/m)_o$ values, which were not significantly different. Only NanoActive® TiO_2 showed negative (q/m) value (-0.31 mC/kg, s.d.= 0.05). NanoActive® TiO_2 (1.21 mC/kg, s.d. = 0.07) also gained the greatest $(q/m)_{net}$ after tribocharging. NanoActive® MgO was next with a $(q/m)_{net}$ value of 0.81 mC/kg (s.d. = 0.12). NanoActive® TiO_2, which had the highest $(q/m)_{net}$, was charged to only about 7.5% of its Gaussian limit. NanoActive® MgO and ISO fine test dust had the next highest charge values, but they are equivalent to only about 6.0% and 2.8% of their Gaussian limits, respectively. In the study conducted by Banerjee and Law (1995) on pollens, charging levels of up to 52-55% of the Gaussian limits were achieved. Note that the diameters of those particulates were as large as 50 µm. The pecan pollen for example, had an average (q/m) value of +7.6 mC/kg using a Teflon® tribocharger. Banerjee and Law (1995) noted that it is the actual charge acquired by the particulates that is important in particle trajectory control in electrostatic-assisted deposition processes and not the ratio of the imparted charge to the maximum charge.

The results in Table 5.2 relatively showed small $(q/m)_{net}$ probably due to the small size of the particles considered. This confirmed the conclusion given by Flagan (2001) that the probability of charging particles decreases with their size. Tianxiang (1999) also noted that the charge on the particle surface could become saturated much below its theoretical maximum charge limit (Gaussian limit) for reason that maybe related to the charge backflow. The (q/m) values obtained in this research had no correlation with the size of particles used.

5.5 Conclusions

This study was conducted to measure the relative chargeability of nanostructured particles and compare them to conventional particles. The following conclusions were drawn from this research:

1. Tribocharging using a Teflon® tribocharger was able to charge the aerosolized nanostructured particles positively. NanoActive® TiO_2 had the highest net charge gained (1.21 mC/kg, s.d.=0.07), followed by NanoActive® MgO (0.81 mC/kg, s.d.=0.12) and ISO fine test dust (0.66 mC/kg, s.d.= 0.13)
2. The net charges gained by the particles, however, were small compared to the Gaussian limit (below 8%). It appears that tribocharging may not be a feasible method of imparting large charge to the nanostructured particles.

.

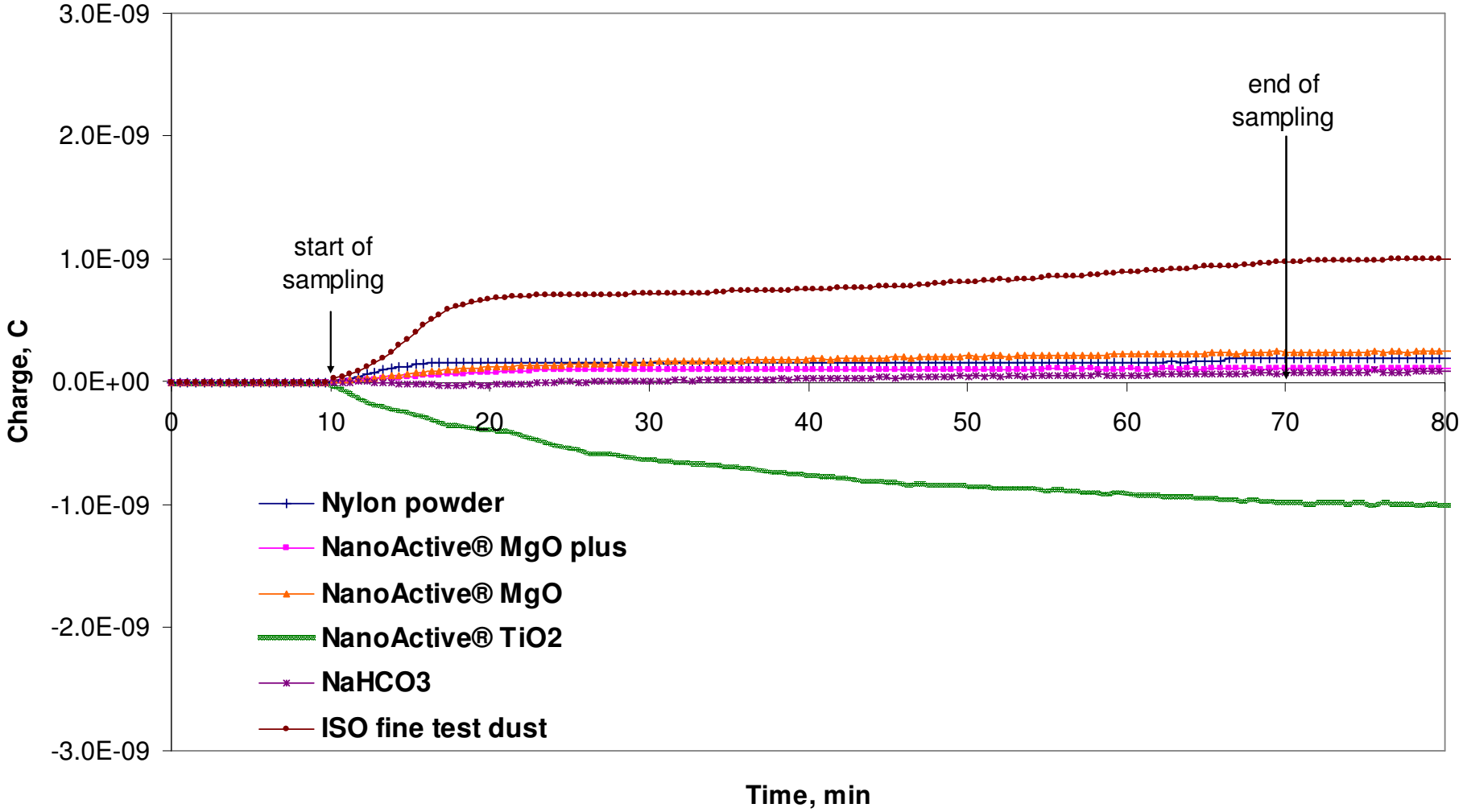

Figure 5.6. Background charges of the particles, that is, the Teflon® tribocharger was not in use.

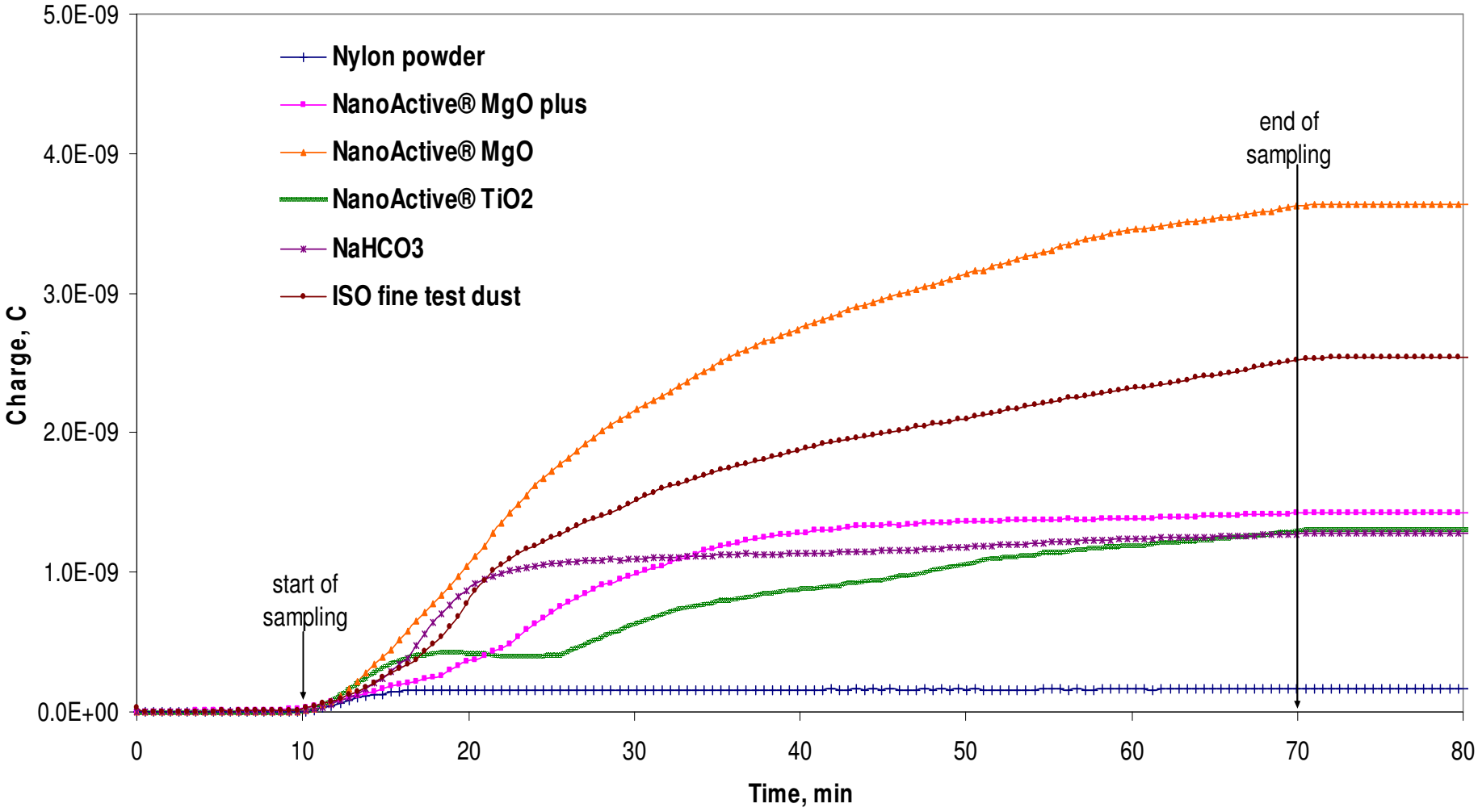

Figure 5.7. Charges of the particles after passing through a Teflon® tribocharger.

Table 5.2. Charge-to-mass ratios of the particles.

Particles	Mass collected on filter (mg)		Charge-to-mass ratios[a], mC/kg							
			Background, $(q/m)_o$		Tribocharged, $(q/m)_c$		Net, $(q/m)_{net}$		Gaussian limit, $(q/m)_{max}$	$(q/m)_{net}/(q/m)_{max}$ x 100
	Mean	s.d.	Mean	s.d.	Mean	s.d.	Mean	s.d.		
Nanostructured particles										
NanoActive® MgO plus	5.57	1.93	0.02 (c)	0.01	0.25 (b)	0.05	0.24 (d)	0.05	11.91	2.02
NanoActive® MgO	4.27	0.84	0.05 (c)	0.02	0.86 (a)	0.11	0.81 (b)	0.12	13.42	6.04
NanoActive® TiO_2	1.45	0.60	-0.31(d)	0.05	0.90 (a)	0.05	1.21 (a)	0.07	16.06	7.54
Conventional particles										
$NaHCO_3$	5.46	3.20	0.02 (c)	0.01	0.24 (b)	0.03	0.21 (d)	0.03	15.22	1.38
ISO fine test dust	2.91	0.57	0.20 (b)	0.04	0.85 (a)	0.10	0.66 (bc)	0.13	24.03	2.75
Reference particle										
Nylon powder[b]	1.17	0.03	0.30 (a)	0.03	0.78 (a)	0.05	0.46 (c)	0.03	--	--

[a]Average of three replicates.

[b]Aerodynamic diameter needed in Gaussian limit calculation was not measured because of malfunction in the instrument.

5.6 References

ASTM Standards. 1997. D 4470 – 97: Standard test methods for static electrification. Philadelphia, PA: ASTM.

Banerjee, S. and S. Law. 1995. Characterization of chargeability of biological particulates by triboelectrification. *IEEE Transactions on Industry Applications* 34(6):1201-1205.

Colver, G. M. 1999. Chapter 3: Electrostatic measurements. In *Instrumentation for fluid-particle flow*, 47-83. S. L. Soo, ed. Norwich, NY: William Andrew Inc.

Flagan, R.C. 2001. Electrical techniques. In *Aerosol measurement: principles, techniques and applications*. P.A. Baron and K. Willeke, eds. New York, NY: John Wiley.

Greaves, J.R. and B. Makin. 1980. Measurement of the electrostatic charge from aerosol cans. In *IAS Annual Meeting*, 1075-1080. Cincinnati, OH: IEEE.

Hinds, W.C. and N.J. Kennedy. 2000. An ion generator for neutralizing concentrated aerosol. *Aerosol Science and Technology* 32:214-220.

John, W. 1980. Particle charge effects. In *Generation of aerosols*, K. Willeke, ed. Ann Arbor, MI: Ann Arbor Science.

Liberto, N. P. 1994. *Powder coating: The complete finisher's handbook*. Alexandria, VA: The Powder Coating Institute.

Lowell, J. and A.C. Rose-Innes. 1980. Contact electrification. *Advanced Physics* 29(6): 947-1023.

Mazumder, M. K., R. A. Sims, A. S. Biris, P. K. Srirama, D. Saini, C. U. Yurteri, S. Trigwell, S. De, and R. Sharma. 2006. Twenty-first century research needs in electrostatic processes applied to industry and medicine. *Chemical Engineering Science* 61:2192-2211

Murtomaa, M. 2002. Electrostatic studies on pharmaceutical powders and aerosols. Thesis. Turku, Finland: University of Turku.

Richards, R, W.F. Li, S. Decker, C., C. Davidson, O. Koper, V. Zaikovski, A. Volodin, T. Rieker, and K.J. Klabunde. 2000. Consolidation of metal oxide nanocrystals. Reactive pellets with controllable pore structure that represent a new family of porous, inorganic materials. *Journal of the American Chemical Society* 122(20):4921-4925.

Sharma, R., S. Trigwell, S., R.A. Sims, and M.K. Mazumder. 2004. Modification of electrostatic properties of polymer powders using atmospheric plasma reactor. In *Polymer Surface Modification: Relevance to Adhesion*, Vol. 3, 25. Mittal, K.L. ed. VSP, AH. Zeist, The Netherlands.

Schnurmann, R. 1941. Friction between solid bodies. *Report on Progress in Physics* 8:71-89.

Stoimenov, P.K., R.L. Klinger, G.L. Marchin and K.J. Klabunde. 2002. Metal oxide nanoparticles as bacterial agents. *Langmuir* 18(17):6679-6686.

Tardos, G.I., R.W.L., Snaddon, P.W. Dietz. 1984. Electric charge measurement on fine airborne particles. *IEEE Transactions on Industry Applications* IA-20(6):1578-1583.

Tianxiang, L. 1999. An experiment study of particle charge and charge exchange related to triboelectric benefiaciation. PhD dissertation. Lexington, KY: University of Kentucky.

Trigwell, S. 2003. Correlations between surface structure and tribocharging of powders. PhD dissertation. Little Rock, AR: University of Arkansas.

Trigwell, S., N. Grable, C.U. Yurteri, R. Sharma, and M.K. Mazumder. 2003. Effects of surface properties on the tribocharging characteristics of polymer powder as applied to industrial processes. *IEEE Transactions of Industry Applications* 39(1):79-86.

Tucholski, D. and G.M. Colver. 1993. Triboelectric charging in a circulating fluidized bed. In *Proceedings of the 2nd International Conference on Applied Electrostatics*, 287-296. Beijing, China: Chinese Physical Society.

6. Numerical Simulation of Particle Transport in an Enclosed Room

6.1 Abstract

Understanding particle transport in rooms is important in solving indoor air quality problems and in controlling particle dispersion. In this study, the transport of aerosolized particles inside an enclosed experimental chamber (3.6 m x 2.4 m x 2.4 m) was simulated by a computational fluid dynamics (CFD) program, FLUENT. Two different types of particles were considered: hollow glass spheres and NanoActive® MgO plus, a nanostructured material. Experiments were also conducted to validate predicted results. In terms of mass concentrations, there was reasonable agreement between predicted and measured values for hollow glass spheres but not for NanoActive® MgO plus. In terms of number concentration, there was large discrepancy between predicted and measured values for both particles. The lack of agreement between predicted and measured values can be due the invalid assumptions in the numerical model (e.g., initial number of particles, constant particle size).

6.2 Introduction

Prediction of particle transport in turbulent flow is essential in various fields, including dispersion of passive or reactive particles in turbulent media and in air pollution (Domgin et al., 1997). For example, in workplaces, residential buildings, and other indoor environments, people are exposed to particulate contaminants (Holmberg and Li, 1998). Fate and deposition of these particulate contaminants in indoor environments has significant implications for human health, clean rooms, and decontamination (Lai, 2004; Zhang, 2005). Gao and Niu (2007) noted that a good understanding of the particle-laden turbulent flow is important in solving indoor air quality

problems and in controlling particle dispersion. Limited data, however, are available on dispersion and deposition of particles in indoor environments (Lai, 2004).

The two major approaches that can be used to study the dispersion of particles in indoor environments are physical modeling and numerical simulation with computational fluid dynamics (CFD). In recent years, CFD has been widely employed in predicting air flow patterns in buildings and has been proven to offer a flexible alternative to physical models (Liddament 1991; Jones and Whittle, 1992; Haghighat et al., 1992). Zhang and Chen (2007) noted that CFD is the most suitable modeling approach to study the spatial distribution of particles in enclosed spaces, because the transport and distribution of airborne particles are highly associated with airflow motion and turbulence.

There are two methods of modeling particle transport in CFD: the Eulerian-Eulerian and Eulerian-Lagrangian. In the Eulerian-Eulerian approach, the particulate phase is treated as another flow and calculated in the fixed coordinate system. In the Eulerian-Lagrangian approach, on the other hand, the fluid or carrier gas is considered as the continuum phase and the particles are considered as the discrete phase. Given the complete fluid flow field, particles are tracked by solving the particle force balance. Chang et al. (2007) cited that most previous CFD works on indoor particle transport are mainly based on the Eulerian-Eulerian approach that takes less computing resources. However, this approach neglects the particulate nature of the particles, and appears to be adequate only for simulating gaseous pollutants or small, neutrally buoyant particles that exactly follow the fluid flow (Chang et al., 2007). Zhang and Chen (2007) compared the Eulerian-Eulerian and Eulerian-Lagrangian methods in predicting particle concentration distribution in ventilated spaces. Their results showed that both methods can predict well the steady-state particle concentration distribution. For the unsteady state condition,

however, their results showed that the Eulerian-Lagrangian method performed better than the Eulerian-Eulerian method. Riddle et al. (2004) also concluded that the Eulerian-Lagrangian method gave better results than the Eulerian-Eulerian approach in predicting the dispersion of gaseous pollutants around buildings.

The major objective of this study was to predict the transport of aerosolized hollow glass spheres and NanoActive® MgO plus in an enclosed room using the Eulerian-Lagrangian approach. Specific objectives were to:

1. predict the mass concentrations (C_m) of particles at various locations inside the chamber;
2. predict the number concentration (C_n) of aerosolized particles at the center of the chamber at various times; and
3. compare predicted results with experimental data.

6.3 Materials and Methods

6.3.1 Theoretical background

The Eulerian-Lagrangian approach was directly implemented by using the discrete phase model (DPM) of FLUENT (Ver. 6.3, Fluent, Inc., Lebanon, NH). In this approach, the fluid phase is treated as a continuum by solving the time-averaged Navier-Stokes equations, while the dispersed phase is solved by tracking a large number of particles through the calculated flow field (Fluent, 2006). The governing equations used in the simulation are summarized in the following sections.

6.3.1.1 Governing equations for the continuous phase

The continuous gas-flow phase is governed by the following equations for unsteady compressible flow (Kleinstreuer, 2003; Zhang, 2005):

continuity

$$\frac{\partial \rho}{\partial t} + \nabla \cdot (\rho \vec{u}) = 0 \tag{6.1}$$

momentum

$$\frac{D(\rho \vec{u})}{Dt} = -\vec{\nabla} p + \vec{\nabla} \cdot \tau \tag{6.2}$$

energy

$$\frac{\partial (\rho E)}{\partial t} + \nabla \cdot (\vec{u}(\rho E + p)) = \nabla \cdot \left(k_{eff} \nabla T + \left(\vec{\vec{\tau}}_{eff} \cdot \vec{u} \right) \right) \tag{6.3}$$

where ρ, t, $\vec{u}$, p, τ, E,T, k_{eff}, and τ_{eff} are fluid density, time, fluid phase velocity, thermodynamic pressure, stress tensor, energy, temperature, effective conductivity, and effective stress tensor, respectively.

The most common turbulence model, the standard k-ε turbulence model, has been used over three decades as the basis for turbulence flow computation (Crowe et al., 1996). The turbulence kinetic energy, k, and its rate of dissipation, ε, are obtained from the following transport equations (Fluent, 2006):

$$\frac{\partial}{\partial t}(\rho k) + \frac{\partial}{\partial x_i}(\rho k u_i) = \frac{\partial}{\partial x_j}\left[\left(\mu + \frac{\mu_t}{\sigma_k} \right) \frac{\partial k}{\partial x_j} \right] + G_k + G_b - \rho \varepsilon - Y_M + S_k \tag{6.4}$$

$$\frac{\partial}{\partial t}(\rho \varepsilon) + \frac{\partial}{\partial x_i}(\rho \varepsilon u_i) = \frac{\partial}{\partial x_j}\left[\left(\mu + \frac{\mu_t}{\sigma_\varepsilon} \right) \frac{\partial \varepsilon}{\partial x_j} \right] + C_{1\varepsilon} \frac{\varepsilon}{k}(G_k + C_{3\varepsilon} G_b) - C_{2\varepsilon} \rho \frac{\varepsilon^2}{k} + S_\varepsilon \tag{6.5}$$

where G_k and G_b represent the generation of k due to the mean velocity gradients and buoyancy, respectively; Y_M represents the contribution of the fluctuating dilatation in compressible turbulence to the overall dissipation rate; σ_k and σ_ε are the turbulent Prandtl numbers for k and ε, respectively; and S_k and S_ε are user-defined source terms for k and ε, respectively. The turbulent (or eddy) viscosity, μ_t, is computed by combining k and ε as follows (Fluent, 2006):

$$\mu_t = \rho C_\mu \frac{k^2}{\varepsilon} \tag{6.6}$$

The model constants $C_{1\varepsilon}$, $C_{2\varepsilon}$, C_μ, σ_k and σ_ε have the following default values in FLUENT:

$$C_{1\varepsilon} = 1.44;\ C_{2\varepsilon} = 1.92;\ C_\mu = 0.09;\ \sigma_k = 1.0;\ \sigma_\varepsilon = 1.3$$

6.3.1.2 Governing equations for the discrete phase

The trajectory of discrete phase is determined by integrating the force balance on the particle. This force balance equates the particle inertia with forces acting on the particle, and can be written as (Fluent, 2006):

$$\frac{du_p}{dt} = F_D(u - u_p) + \frac{g_x(\rho_p - \rho)}{\rho_p} + F_x \tag{6.7}$$

where u, u_p, g_x, ρ_p, ρ, and F_x are the fluid phase velocity, particle velocity, gravitational acceleration, particle density, fluid density, and an additional acceleration (force per unit particle mass), respectively. F_D is the drag force per unit particle mass equal to:

$$F_D = \frac{18\mu}{\rho_p d_p^2} \frac{C_D Re}{24} \tag{6.8}$$

$$Re \equiv \frac{\rho d_p |u_p - u|}{\mu} \tag{6.9}$$

where μ, d_p, C_D, and Re are the molecular viscosity of the fluid, particle diameter, drag coefficient, and Reynolds number, respectively. The location of each particle, x, is tracked with the following equation:

$$\frac{dx}{dt} = u_p \tag{6.10}$$

The air velocity, u, in equation 6.7 consists of the time averaged component, $\bar{u}$, and the instantaneous or fluctuating velocity component, $u'(t)$ (Zhang, 2005; Fluent, 2006; Zhang and Chen, 2007):

$$u = \bar{u} + u'(t) \tag{6.11}$$

The $\bar{u}$ component is computed using the Reynolds-averaged Navier-Stokes (RANS) equations with the standard k-ε turbulence model. The $u'(t)$ component is computed using a stochastic approach, such as the discrete random walk (DRW) model or eddy lifetime model. Its value prevails during the lifetime of the turbulent eddy influencing the particle and is assumed to obey the Gaussian probability distribution (Zhang, 2005; Predicala, 2003; Graham and James, 1996). Using the DRW model to calculate $u'(t)$, the particle turbulent dispersion is correlated to the flow k (Zhang, 2005; Zhang and Chen, 2007):

$$u'(t) = \zeta \sqrt{\frac{2k}{3}} \tag{6.12}$$

where the variable ζ is a Gaussian random number.

6.3.2 Case description

This study simulated the dispersion of aerosolized particles inside an enclosed experimental chamber with dimensions of x = 3.6 m long, z = 2.4 m wide, and y = 2.4 m high (Fig. 6.1). A known mass of particles was injected into the chamber through a small hole (x = 0, y = 1.778 m, z = 1.1027 m) with a diameter of 0.0127 m. The injection lasted for approximately 3 s at 40 psig.

6.3.3 Test particles

Two different types of particles were considered: hollow glass spheres and NanoActive® MgO plus. The hollow glass sphere was selected as the reference particle because of its relative

sphericity (Fig. 6.2a) and narrower size distribution (geometric standard deviation, GSD = 1.56, s.d. = 0.01). The NanoActive® MgO plus was selected as the representative particle for nano-agglomerates; it was irregular in shape (Fig. 6.2b) and had a wider size distribution (GSD = 1.89, s.d. = 0.06) than the hollow glass sphere.

Preliminary measurements with the Aerodynamic Particle Sizer™ (APS) spectrometer (Model 3321, TSI, Inc., Shoreview, MN) showed that the two particles have a geometric mean diameter (GMD) of approximately 10 μm aerodynamic diameter. The actual particle diameter, d_p, was calculated using the following formula (Hinds, 1999):

$$d_p = \sqrt{\frac{\rho_o}{\rho_p}} d_a \tag{6.13}$$

where d_a and ρ_o is the aerodynamic diameter and standard density (1000 kg/m^3), respectively. The calculated d_p's were 9.17 μm and 6.43 μm for the hollow glass spheres and NanoActive® MgO plus, respectively, assuming d_a = 10 μm and ρ_p values of 1190 kg/m^3 and 2420 kg/m^3 for hollow glass spheres and NanoActive® MgO plus, respectively.

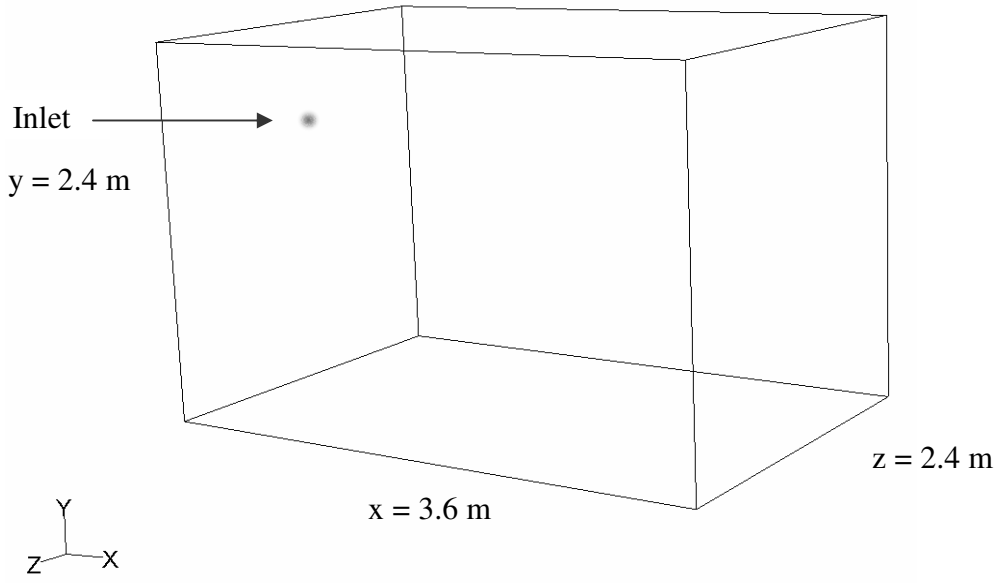

Figure 6.1. Schematic diagram of the experimental chamber used in the simulation.

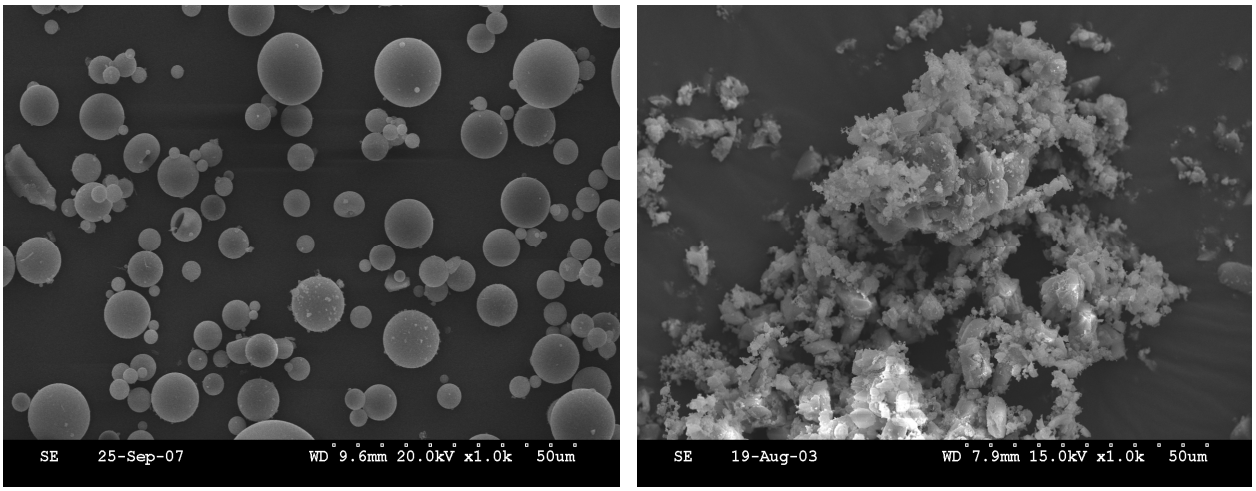

(a) (b)

Figure 6.2. Scanning electron micrographs of the particles: (a) hollow glass spheres and (b) NanoActive® MgO plus.

6.3.4 Geometry and mesh generation

A single, integrated pre-processor for CFD analysis (Gambit 2.3.16, Fluent Inc., Lebanon, NH) was used to construct the geometry and to examine the quality of the mesh of the domain. For hollow glass spheres, in determining the C_m at t=60 s, three meshing schemes were compared: fine, coarse, and very fine (Table 6.1). The "fine mesh" scheme was used for the simulation of the velocity profile and for tracking the transport of the particles. The "coarse mesh" and a "very fine mesh" schemes were considered to check the effect of mesh size on predicted results. For NanoActive® MgO plus, only the coarse meshing scheme was used to minimize computational time.

Table 6.1. Description of the three meshing schemes of the geometry of chamber and its inlet for hollow glass spheres. The coarse mesh scheme was used for NanoActive® MgO plus.

Mesh	Chamber		Inlet	
	Meshing scheme	Number of mesh volumes	Meshing scheme	Number of mesh faces
coarse	tetrahedral/hybrid	137,424	triangular	12
fine	tetrahedral/hybrid	400,432	triangular	36
very fine	tetrahedral/hybrid	1,122,336	triangular	302

6.3.5 Implementation of the CFD model

More detailed instructions and definitions about the implementation of the DPM can be found in FLUENT User's Guide (Fluent, 2006). The reference particle (i.e., hollow glass spheres) was first considered. Once satisfactory results were obtained, NanoActive® MgO plus was then simulated using the same general procedure and assumptions, except for the ρ_p and d_p values.

The dilute particle flow assumption was justified by the low volume fraction of the particulate phase (i.e., 0.53 % and 0.04 % for hollow glass spheres and NanoActive® MgO plus, respectively). The assumption of one-way interaction was also satisfied by having a light (< 1) particulate loading (i.e., 0.25 and 0.04 for hollow glass spheres and NanoActive® MgO plus, respectively). Table 6.2 shows the major assumptions for the simulation of the continuous phase. A velocity magnitude of 12 m/s was specified for the inlet boundary condition. This value came from the measurement of nitrogen gas flow at the inlet (without the presence of particles) using a hot-wire anemometer (Model 8347, TSI Inc., Shoreview, MN). At time 4 s, when the injection was stopped, the inlet boundary condition was changed from velocity inlet to wall.

Table 6.3 shows the major assumptions used in the simulation of the transport of hollow glass spheres (discrete phase) in the chamber. Solid cone injection type and 100 particles streams or parcels were specified in the model. FLUENT had a general guideline of 5-20 parcels to simulate non evaporative sprays (Fluent, 2006). Zhang (2005) assumed 200 parcels to simulate nano-agglomerates using the Eulerian-Lagrangian approach in a steady-state, incompressible flow. He also used a chamber geometry that has both inlet and outlet. This research considered an unsteady, three dimensional, compressible flow; as such, a smaller parcel number (100) was used. Larger parcel number will result in very long computational time (Fluent, 2006), especially with the flow assumptions (transient, three dimensional, and compressible) used in this study.

The calculated d_p (9.17 μm) and measured ρ_p (1190 kg/m^3) were used for hollow glass spheres. The stop and start time of injection were assumed to be 0 and 3 s, respectively. Particle boundary conditions such as escape and trap were used. The DRW model was used to predict the dispersion of particles due to turbulence in the fluid phase.

In simulating the transport of NanoActive® MgO plus particles in the chamber, general assumptions shown in Table 6.3 were used except for the d_p and ρ_p values. Also, as mentioned earlier, the coarse meshing scheme was used to minimize computational time. Because of uncertainties in the values of d_p and ρ_p associated with the irregular shape and porous nature of the NanoActive® MgO plus particles, four cases were considered. Table 6.4 shows the different cases and the comparison of the total flow rates used in the simulation and those obtained from the experiments. In case 1, d_p and ρ_p values of 6.43 μm and 2420 kg/m^3, respectively, were assumed. Case 2 considered the combination d_p = 10 μm and and ρ_p = 400 kg/m^3. The density of 400 kg/m^3 was considered since the NanoActive® MgO plus particles are porous (Zhang,

2005) (Fig. 6.2b). Case 3 had d_p and ρ_p values of 50 µm and 400 kg/m^3, respectively. In this case, the diameter was made 5 times bigger than its assumed d_a (10 µm) to account for particle agglomeration. Case 4 was similar to case 2, except that it considered other forces (i.e., Saffman lift force, Brownian motion) in addition to the gravitational and drag forces. However, by looking at post-processed particle trajectories of all the cases, the predicted results did not show agreement with experimental data. In the experiments, right after injection of particles, the measured concentration was highest at the location farthest from the injection point (3.0 m). Predicted concentration was highest at location nearest the injection point (0.6 m). In order to show a sample result from the simulation of NanoActive® MgO plus, although there were no promising results, one case (case 2) was run for up to 600 s.

Table 6.2. Major assumptions used in the simulation of the continuous phase.

FLUENT parameters		Assumptions
Model	Solver	Pressure based
	Space	3D
	Time	Unsteady
	Energy Equation	Activated
	Viscous Model	k-ε (standard)
Operating conditions	Operating pressure	101325 Pa
	Operating temperature	293.15 °K
	Gravitational acceleration	Activated (y direction = - 9.8 m/s^2)
Material	Air	
	Density	ideal-gas
Boundary condition	Inlet	velocity inlet
	Velocity magnitude	12 m/s
	Turbulence	
	Turbulent intensity	10%
	Hydraulic diameter	0.0127 m
	Chamber	interior
	Chamber walls	walls
	Control volumes	interior
	Control surfaces	walls

Table 6.3. Major assumptions used in the simulation of the discrete phase (hollow glass spheres).

FLUENT parameters		Assumptions
Model	DPM	Activated
Injection	Injection type	solid cone
	Number of particle streams	100
	Point properties	
	Diameter	9.17×10^{-6} m
	Start time	0
	Stop time	3 sec
	Velocity magnitude	12 m/s
	Cone angle	5°
	Radius	0.00635 m
	Total flow	0.01 kg/s
	Turbulent dispersion	
	Stochastic tracking	Enabled
Material	Inert particle	
	Density	1190 kg/m^3
Boundary condition	Inlet	set as "wall" after injection
	Discrete phase boundary type	
	Inlet	escape
	Chamber walls (except the floor)	escape
	Chamber floor	trap

Table 6.4. Simulation cases and experimental parameters for NanoActive® MgO plus.

Methods	**Particle diameter, µm**	**Particle density, kg/m^3**	**Total flow rate, kg/s**	**Forces considered**
CFD (case 1)	6.73 (actual)	2420 (true)	0.004	gravitational force, drag force
CFD (case 2)	10 (aerodynamic)	400 (bulk)	0.004	gravitational force, drag force
CFD (case 3)	50 (aerodynamic)	400 (bulk)	0.004	gravitational force, drag force
CFD (case 4)	10 (aerodynamic)	400 (bulk)	0.004	drag force, Saffman lift force, Brownian motion
Experiment 1 (Filter samplers)			0.004	
Experiment 2 (APS® spectrometer)	5.78[a], 3.59[b], 2.75[c]		0.004	

[a]at t=60 s; [b]at t=300 s; [c]at t=600 s

6.3.4.1 Calculation of number of particles dispersed in the chamber

The total number of particles, N, dispersed inside the chamber was estimated by dividing the total mass, M, of particles injected into the chamber by the individual mass, m, of the particles:

$$N = \frac{M}{m} \tag{6.14}$$

$$m = \rho_p \times \frac{\pi}{6} d_p{}^3 \tag{6.15}$$

The measured M during the 3 s injection of hollow glass spheres and NanoActive® MgO plus were 0.03 kg and 0.012 kg, respectively. The calculated N for hollow glass spheres (9.17 µm, 1190 kg/m^3) and NanoActive® MgO plus (10 µm, 400 kg/m^3) were 6.24x10^{10} particles and 5.73x10^{10} particles, respectively (Table 6.5). Table 6.5 summarizes the N values for the other cases.

Table 6.5. Number of particles dispersed inside the chamber calculated using different particle size and density.

Particles	Total mass injected, kg	Number of particles dispersed inside the chamber
Hollow glass spheres (9.17 µm, 1190 kg/m^3)	0.030	6.24 x 10^{10}
NanoActive® MgO plus (6.73 µm, 2420 kg/m^3)	0.012	3.11 x 10^{10}
NanoActive® MgO plus (10 µm, 400 kg/m^3)	0.012	5.73 x 10^{10}
NanoActive® MgO plus (50 µm, 400 kg/m^3)	0.012	4.58 x 10^8

6.3.4.2 Calculation of number of particles in a parcel

Since it is impossible to track each particle in the Eulerian-Lagrangian method, the particulate phase was calculated based on particle parcels (Zhang, 2005). Each parcel contained a certain large number of particles with the same properties and moving together in the flow field (Zhang, 2005).

To calculate the number of particles in a parcel, parameters defined in the DPM simulation (i.e., d_p and ρ_p, mass flow rate of injection, and time step size) were used. For

unsteady, solid cone injection, the number of particles in a parcel was calculated using the following relationship (Fluent, 2006):

$$\text{Particle number per parcel} = \text{Flow rate per parcel} * (\text{Time step} / m) \quad (6.16)$$

$$\text{Flow rate per parcel} = (\text{Total flow rate} / \text{Number of parcels}) \quad (6.17)$$

An example of calculated number of particles per parcel of hollow glass spheres with its corresponding time constant and time step size is shown in Table 6.6. The time constant is the time being modeled in the system, while the time step size is the magnitude of Δt to get the number of time steps. For example, if the time constant is 1 s and the time step size is 0.05 s, the number of time steps is 20. For each time step, a maximum iteration of 100 was set in this study which was above the FLUENT recommendation of 20 maximum iterations per time step for better convergence. More detailed instructions about the transient flow simulation can be found in FLUENT User's Guide (Fluent, 2006).

A time-dependent problem frequently has a very fast start-up transient that decays rapidly. Therefore, it is often advisable to choose a conservatively small magnitude of Δt, which may then be gradually increased as calculation proceeds (Fluent, 2006). In this simulation, a time step size of 0.05 s was first used to simulate the system at times 1, 2, 3, 4, 5, 6, 7, 8, 9, and 10 s. The time step size was then increased to 0.5 s to simulate the system at times 20, 30, 40, 50, and 60 s. And last, a time step size of 2 s was used to simulate the system at times 120, 180, 240, 300, 360, 420, 480, 540, and 600 s. The result of simulation for the period at 60 s was compared with experiment data, which were obtained with filter samplers. The results of simulation at 60 - 600 s were compared with measured data from the Aerodynamic Particle Sizer (APS®) spectrometer.

Table 6.6. Calculated number of particles per parcel of hollow glass spheres using 100 parcels.

Particle	Time constant, s	Total flow rate (based on experiments), kg/s	Time step size, s	Mass of each particle, kg	No. of particles per parcel
Hollow glass spheres (9.17 μm, 1190 kg/m^3)	1	0.01	0.05	4.8×10^{-13}	1×10^7
	10	0.01	0.5	4.8×10^{-13}	1×10^8
	60	0.01	2	4.8×10^{-13}	4×10^8

6.3.4.3 Post-processing of the simulation results

The FLUENT software provides post-processing options for displaying, plotting, and reporting the continuous and discrete phase parameters. Using the fine mesh, contour plots and pathlines of the magnitude of velocity of the continuous phase were displayed at different times. The particle trajectories were also tracked at different times after the injection of particles.

The nature of the Eulerian-Lagrangian simulation leads to track every particle parcel in the flow field. As a result, every particle parcel has its location calculated at any time (Zhang, 2005). Each parcel that contains large number of particles is mathematically symbolized as a point in the Eulerian-Lagrangian simulation and is commonly represented as a dot in the post-processed results (Zhang, 2005).

In predicting the C_m values at t=60 s at three different locations (0.6 m, 1.8 m, and 3.0 m away from injection point) inside the chamber, a control volume size of 0.4 m x 0.4 m x 0.4 m was used. In predicting the C_n values at the center of the chamber at 60-600 s, three different control volume sizes or sub-domains were tried to count the particle parcels within the chamber to account for the changes with time. The three control volume sizes were: (1) 0.2 m x 0.2 m x 0.4 m (0.016 m^3), (2) 0.3 m x 0.3 m x 0.4 (0.036 m^3), and (3) 0.4 m x 0.4 m x 0.4 m (0.064 m^3). Zhang (2005) used a C-based program that located and counted the parcels and then calculated

the number and mass concentrations. In this study, the number of parcels within the control volume was counted manually. Then, based on the number of parcels, the particle concentrations (number and mass) were determined.

6.3.5 Experimental validation

Two sets of experiments were conducted to validate the CFD simulation results. The first set of experiments was conducted to validate predicted C_m values at three different locations inside the chamber (Fig. 6.3), namely, sampling locations 1, 2, and 3, which were located 0.6 m, 1.8 m, and 3.0 m away from the injection point, respectively. Each sampling location had a filter sampler that collected airborne particles during the first 60 s after particle dispersion (Fig. 6.3). The three filter samplers were connected to a sampling pump that supplies a sampling flow rate of approximately 2 L/min. The particle C_m value was obtained by dividing the mass collected by the volume of air sampled for 60 s.

In the second set of experiments, the APS® spectrometer was used to continuously measure the C_n value of particles at the center of the chamber (Fig. 6.4) every 60 s for a period up to 600 s. The APS measures the size distribution of particles from 0.5 to 20 µm equivalent aerodynamic diameter.

For both sets of experiments, a nominal mass of 50 g was used for hollow glass spheres and NanoActive® MgO plus. The particles were placed in a powder disperser that was connected to a compressed nitrogen gas cylinder. At a set pressure of 40 psig, the particles were aerosolized and injected for about 3 s inside an enclosed chamber where the particle measuring instruments were located. Three replications were conducted for each type of particle per experiment.

Table 6.7 shows the total mass flow rates of the particles used in the experiments. Table 6.8 shows the particle properties (i.e., d_p and ρ_p) assumed in simulation of hollow glass spheres and the comparison of the total flow rates used in the simulation and those obtained from experiments. From experiment 2 with APS, the change in particle diameter with time was measured. Table 6.4 shows the different cases used for predicting the transport of NanoActive® MgO plus and comparison of the total flow rates used in the simulation and those obtained from the experiments.

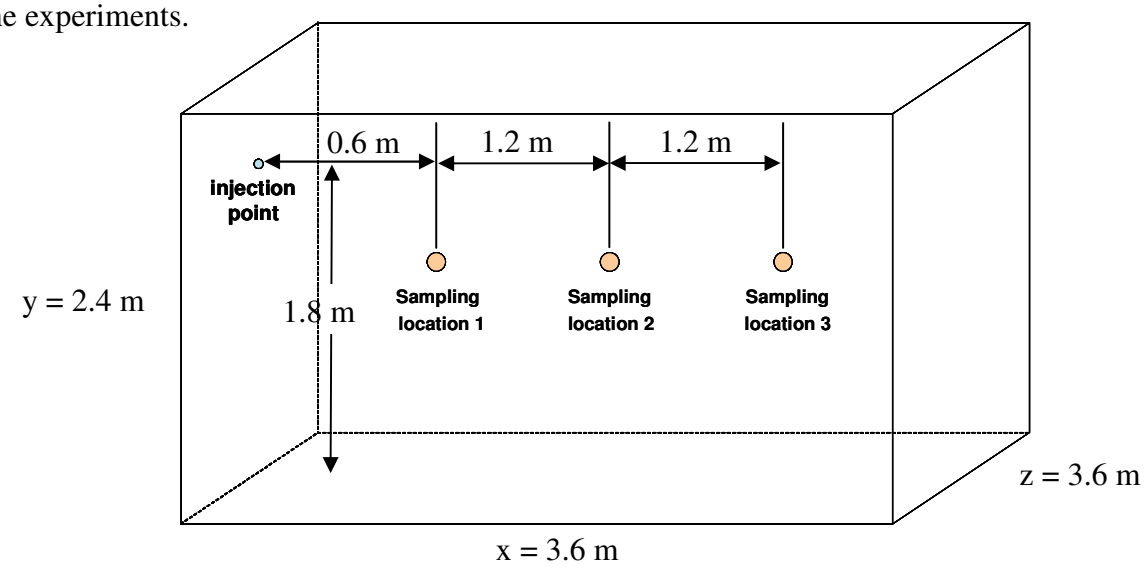

Figure 6.3. The experimental set-up with three filter samplers.

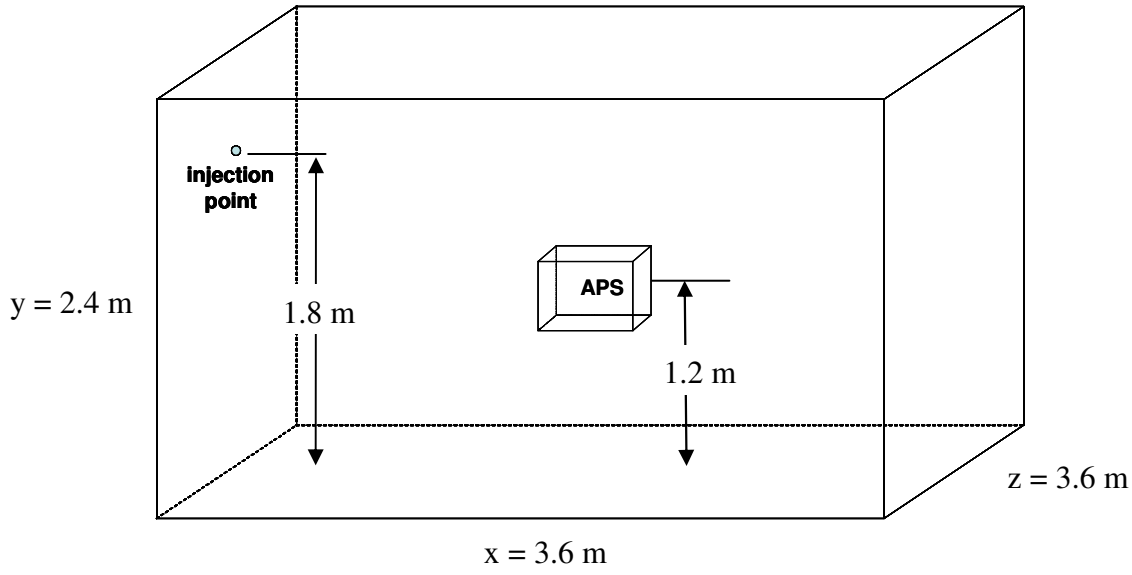

Figure 6.4. The experimental set-up with the Aerodynamic Particle Sizer® (APS) spectrometer.

Table 6.7. Total mass flow rates of particles obtained from the experiments. Each value represents the mean of three replicates.

Experiment	Total flow rate, kg/s			
	Hollow glass spheres		NanoActive® MgO plus	
	Mean	s.d.	Mean	s.d.
Experiment 1 (Filter samplers)	0.013	0.002	0.004	0.001
Experiment 2 (APS® spectrometer)	0.011	0.001	0.004	0.001

Table 6.8. Simulation and experimental parameters for hollow glass spheres.

Methods	Particle diameter (actual), µm	Particle density (true), kg/m^3	Total flow rate, kg/s	Forces considered
CFD	9.17	1190	0.010	gravitational force, drag force
Experiment 1 (Filter samplers)	--	--	0.013	
Experiment 2 (APS® spectrometer)	8.23[a], 6.49[b], 5.82[c]	--	0.011	

[a]at t=60 s; [b]at t=300 s; [c]at t=600 s

6.3.5.1 Data analysis

The ASTM standard guide for statistical evaluation of indoor air quality models (ASTM, 2003) was used to assess the general agreement between predicted concentration (C_p) and observed (or measured) concentration (C_o). ASTM (2003) defined the normalized mean square error (NMSE) as a measure of the magnitude of prediction error relative to C_p and C_o. The formula for calculating NMSE is as follows (ASTM, 2003):

$$\text{NMSE} = \overline{(C_p - C_o)^2} \Big/ \left[(\overline{C}_o)(\overline{C}_p)\right] \tag{6.18}$$

In equation 6.18, $\overline{C}_o$ and $\overline{C}_p$ are average values for the measured and predicated concentrations, respectively, that is,

$$\overline{C}_o = \sum_{i=1}^{n} C_{oi} \Big/ n \tag{6.19}$$

$$\overline{C}_p = \sum_{i=1}^{n} C_{pi} \Big/ n \tag{6.20}$$

where n is the number of observed or predicted values. The parameter $\overline{(C_p - C_o)^2}$ is given by:

$$\overline{(C_p - C_o)^2} = \sum_{i=1}^{n} (C_{pi} - C_{oi})^2 \Big/ n \tag{6.21}$$

Based on ASTM standard guide, a NMSE value of 0.25 or lower is the general indication of adequate model performance (ASTM, 2003).

6.4 Results and Discussion

6.4.1 Predicted gas velocities

Figure 6.5 shows the contour plots of velocities of nitrogen gas for the periods t = 1 to 3 s and at t = 4 s when the injection was stopped. The red color represents the highest velocity magnitude (V_{max} = 12 m/s) for t = 1, 2, and 3 s (Figs. 6.5a-6.5c). At t = 4 s, the gas velocities had decreased considerably, with V_{max} dropping to 0.078 m/s (Fig. 6.5d).

The pathlines of the continuous phase inside the chamber after injection are shown in Figure 6.6. Several circular motions or vortices can be observed. At t = 10 s, distinct circular motions of gas were formed at the sides/periphery of the injection area (Fig. 6.6a). At t = 60, 300, and 600 s after injection (Figs. 6.6b-6.6d), several circular motions can also be observed inside the chamber and V_{max} (0.060 m/sec) can be observed near the boundaries (walls and corners) of the chamber. The slowest movement of air can be observed at the center of the chamber, but it continuously changed with time.

6.4.2 Predicted particle trajectories

The particle trajectories of the hollow glass spheres are shown in Figures 6.7a-6.7d. The particle trajectories at t = 3 s (Fig. 6.7a) seemed to follow the gas flow as shown in Figure

6.5d. Also, the particles appeared to move from the direction of injection point to the other side of the chamber as shown at t = 60 s (Fig. 6.7b). At t = 300 s, the particles were more evenly distributed inside the chamber (Fig. 6.7c), and at t=600 s, there was a great decrease in number of parcels (Fig. 6.7d).

6.4.3 Comparison of predicted results with experimental data

6.4.3.1 Hollow glass spheres

Table 6.9 shows the predicted and measured mass concentrations of hollow glass spheres at three different sampling locations inside the chamber at t=60 s. The simulation results were based on the control volume dimensions of 0.4 m x 0.4 m x 0. 4 m. All meshing schemes showed good agreement with experimental data in terms of the decreasing trend in mass concentration with increasing distance from the injection point of the particles (Table 6.9). The predicted C_m value from the very fine mesh scheme was closest to the measured mean C_m value at sampling location 1 (0.6 m from the injection point). However, the fine mesh scheme had the closest C_m values to the measured mean C_m values at sampling location 2 (1.8 m from the injection point) and 3 (3.0 m from the injection point). The use of very fine mesh gave the smallest NMSE value, indicating that its results had the best agreement with measured C_m values. This value was lower than the 0.25 limit set by ASTM standards (ASTM, 2003). The use of coarse mesh, on the other hand, gave a NMSE value of 0.27. Depending on cost of computation and time required to obtain the predicted results, the use of coarse meshing scheme will give relatively the most cost-effective computation and less simulation time, although the NMSE value was above the level set by ASTM.

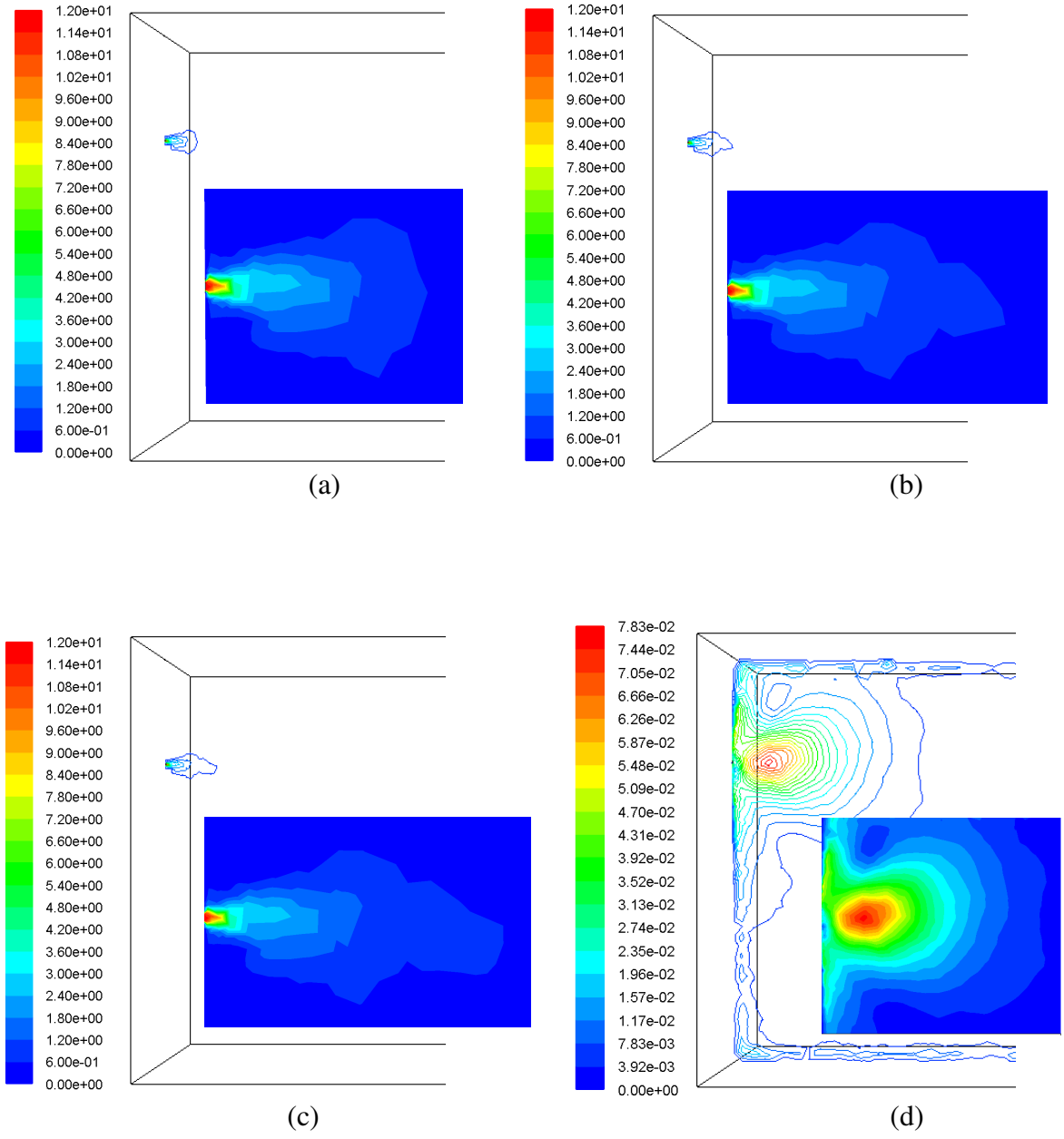

Figure 6.5. Contour plots of the velocities of the gas at various times: (a) 1 s , (b) 2 s, (c) 3 s, and (d) 4 s using fine mesh. Number scale on the left represents the velocity magnitude in m/s. Inserts are the more detailed picture of the injection.

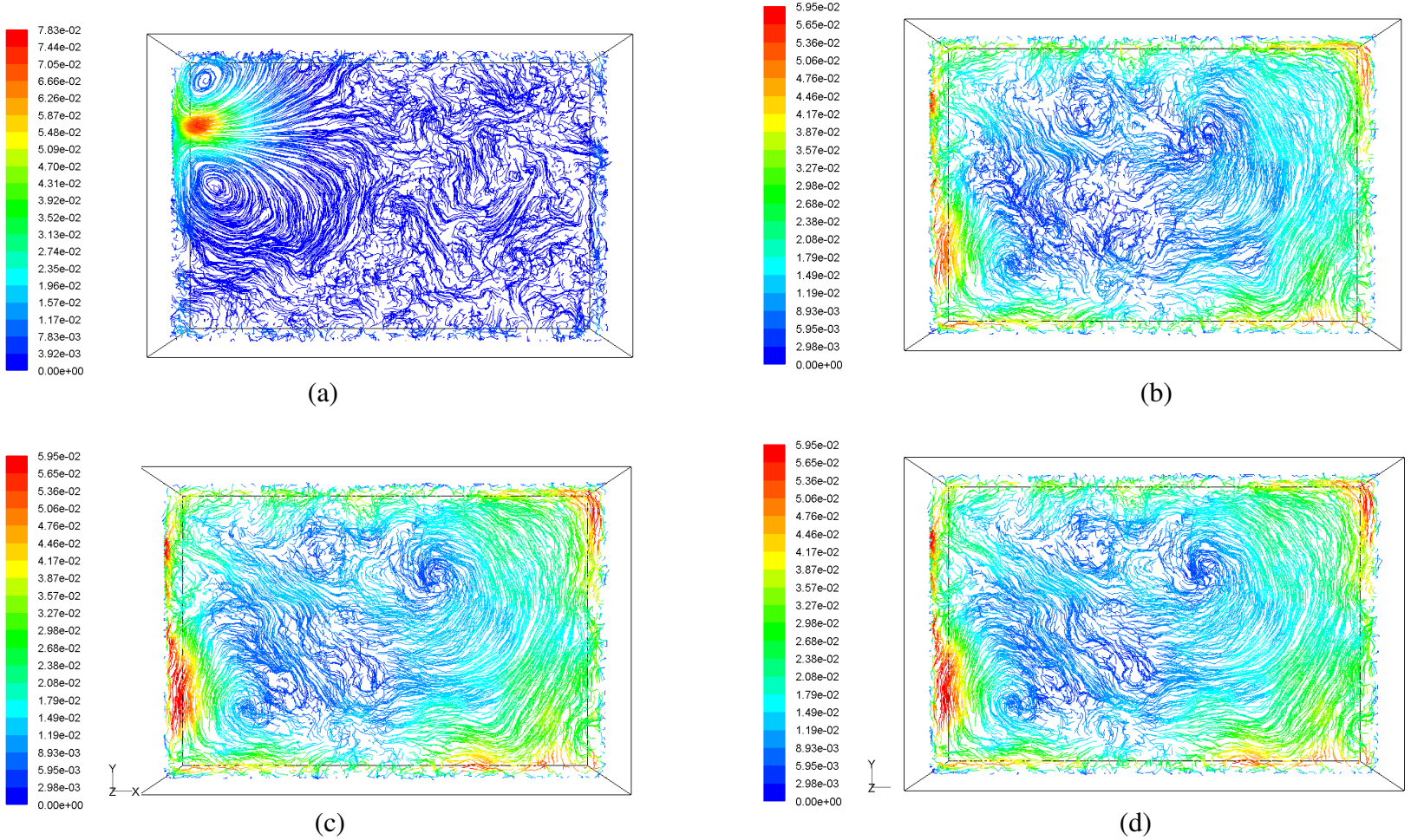

Figure 6.6. Pathlines of the velocity of the gas inside the chamber at various times: (a) 10 s, (b) 60 s, (c),300 s, and (c) 600 s using fine mesh. The plots are in the x-y plane and at the center of the injection port (z = 1.1 cutting plane). Number scale on the left represents the velocity magnitude in m/sec.

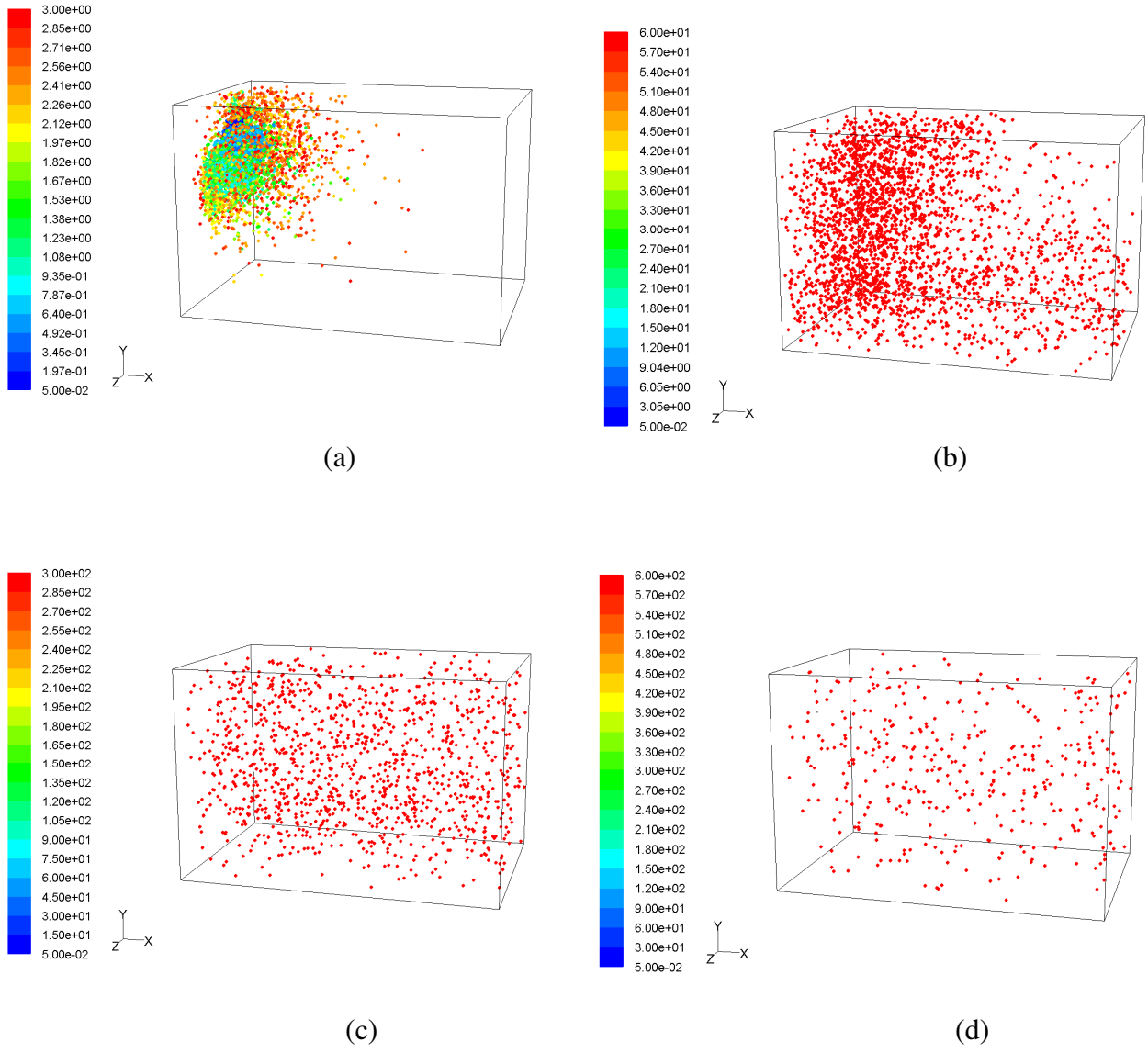

Figure 6.7. Particle trajectories of hollow glass spheres at various times: (a) 3 s, (b) 60 s, (c) 300 s, and (d) 600 s using fine mesh and 100 parcels. The dots in the plots represent the parcels that contain a large number of particles with the same properties. Number scale on the left represents the particle residence time in s.

Predicted and measured C_n values for hollow glass spheres at the center of the chamber are listed in Table 6.10. In general, there were large discrepancies between the predicted and measured C_n values. Predicted values were up to two orders of magnitude larger than measured values. The lack of agreement between predicted and measured values could be due to the changing particle size distribution with time. This was not accounted for in the CFD simulation in which particle size was assumed constant. There also could be considerable error in the estimated numbers of particles at the inlet (Tables 6.5 and 6.6).

Table 6.9. Predicted and measured mass concentrations, C_m, of the hollow glass spheres at t = 60 s after injection at three different sampling locations.

	C_m, mg/m^3			**NMSE**
	Distance from injection point, m			
	0.6 (location 1)	1.8 (location 2)	3.0 (location 3)	
Predicted (coarse mesh)	348	136	91	0.27
Predicted (fine mesh)	386	96	45	0.33
Predicted (very fine mesh)	290	156	111	0.24
Measured (filter samplers)	247 (s.d.=132)	84 (s.d.=35)	19 (s.d.=9)	

Table 6.10. Comparison of predicted and measured number concentrations, C_n, of hollow glass spheres at the center of the chamber. Predicted data started at 60 s for comparison to the first measured data which was obtained at 60 s.

Time, s	**C_n, #/cm^3**				
	Predicted (0.4m x 0.4m x 0.4m)	**Predicted** (0.3m x 0.3m x 0.4m)	**Predicted** (0.2 m x 0.2m x 0.4m)	**Measured (APS® spectrometer) Mean[a]**	**s.d.**
60	199,841	64,175	71,546	14,200	2,946
120	598,385	289,075	182,117	2,257	486
180	526,839	173,445	234,151	3,443	2,105
240	331,713	196,571	312,201	2,440	645
300	351,226	115,630	26,017	2,647	928
360	188,621	23,126	52,033	3,067	965
420	331,713	127,193	182,117	3,910	871
480	188,621	46,252	104,067	5,430	1,104
540	260,167	92,504	130,084	5,143	1,282
600	240,655	69,378	52,033	4,893	1,279
NMSE	78	34	39		

[a]Mean of three replicates

6.4.3.2 NanoActive® MgO plus

Predicted results for NanoActive® MgO plus did not agree with measured data. Table 6.11 shows the predicted and measured C_m values. The measured C_m was highest at the location farthest from the injection point (3.0 m). Predicted results, on the other hand, showed that concentration was highest at location nearest the injection point (0.6 m). The disagreement in values is probably due to the irregular and polydisperse nature of NanoActive® MgO plus. The NMSE value was also higher than the ASTM guideline value of 0.25. With this type of particles (i.e., nano-aggregates), it appears that direct implementation of the DPM of FLUENT that uses the Eulerian-Lagrangian approach appeared to be not applicable. Zhang and Zheng (2007), however, were able to simulate C_m of nano-aggregates at the center of a room-scale chamber. They achieved this by developing a collision model for a large number of particles with significantly different sizes and incorporate the model to the Eulerian-Eulerian approach. They also used user-defined functions to account for factors such as diffusivity and source terms.

Predicted and measured C_n values for NanoActive® MgO plus are summarized in Table 6.12. Similar to hollow glass spheres, large discrepancies between the predicted and measured C_n values were observed. Again, this can be due to possible error in estimating the number of particles at the inlet (Tables 6.5 and 6.6). In addition, this could be accounted for by the changing particle size distribution. In the simulation, it was assumed that the NanoActive® MgO plus was spherical and monodisperse and that the size did not change with time.

Table 6.11. Comparison of the predicted and measured mass concentrations, C_m, of NanoActive® MgO plus (10 µm, 400 kg/m^3) at t=60 s. Each experimental data point represents the mean of three replicates.

	C_m, mg/m^3			**NMSE**
	Distance from injection point, m			
	0.6 (location 1)	1.8 (location 2)	3.0 (location 3)	
Predicted (coarse mesh)	216	135	37	3.34
Measured (filter samplers)	153 (s.d.=107)	505 (s.d.=292)	707 (s.d.=307)	

Table 6.12. Comparison of predicted and measured number concentrations, C_n, of NanoActive® MgO plus at the center of the chamber. Predicted data started at 60 s for comparison to the first measured data which was obtained at 60 s.

Time, s	**C_n, #/cm^3**				
	Predicted (0.4m x 0.4m x 0.4m)	**Predicted** (0.3m x 0.3m x 0.4m)	**Predicted** (0.2 m x 0.2m x 0.4m)	**Measured (APS® spectrometer)**	
				Mean[a]	**s.d.**
60	644,576	336,877	190,985	22,533	2,574
120	531,178	190,985	190,985	7,440	400
180	483,432	159,155	95,493	6,543	1,762
240	483,432	201,596	167,112	6,437	1,855
300	346,161	53,052	119,366	6,677	1,682
360	376,003	159,155	143,239	6,510	1,762
420	483,432	169,765	143,239	6,293	1,626
480	358,098	116,713	47,746	6,147	1,635
540	298,415	137,934	143,239	5,813	1,993
600	370,034	190,985	119,366	5,700	1,613
NMSE	55	23	16		

[a]Mean of three replicates

6.5 Conclusions

This study was conducted to predict the transport of aerosolized hollow glass spheres and NanoActive® MgO plus in an enclosed chamber using the Eulerian-Lagrangian approach. The following conclusions were drawn from this research:

1. For hollow glass spheres, the predicted mass concentrations at three different locations inside the chamber, at t = 60 s, had relatively good agreement with measured values. The very fine mesh scheme showed the smallest NMSE value that was within the limit set by ASTM standards. Predicted number concentrations, however, did not show good agreement with measured data.
2. For NanoActive® MgO plus, there were large discrepancies between predicted and measured mass and number concentrations. Direct implementation of discrete phase model of FLUENT appeared to be not applicable with the irregularly-shaped and polydisperse nature of nano-agglomerates. Incorporation of other models (i.e., collision model) and other user-defined functions might work with nano-agglomerates.

6.6 References

ASTM. 2003. Standard guide for statistical evaluation of indoor air quality models (D5157 – 97, Reapproved 2003). In: Annual Book of American Society for Testing Materials Standards. Philadelphia, PA: American Society for Testing Materials.

Chang, T.J., H. Kao, and Y. Hsieh. 2007. Numerical simulation of the effect of ventilation pattern on coarse, fine, and very fine particulate matter removal in partitioned indoor environment. *Journal of Air and Waste Management Association* 57:179-189.

Crowe, C.T., T.R. Troutt, and J.N. Chung. 1996. Numerical models for two-phase turbulent flows. *Annual Review of Fluid Mechanics* 28:11-43.

Domgin, J.F., D. Huilier, H. Burnage, and P. Gardin. 1997. Coupling of a Lagrangian model with a CFD code: Application to numerical modeling of the turbulent dispersion of droplets in a turbulent pipe flow. *Journal of Hydraulic Research* 35(4): 473-490.

Fluent. 2006. User's Guide. Lebanon, NH: Fluent, Inc.

Gao, N.P. and J.L. Niu. 2007. Modeling particle dispersion and deposition in indoor environments. *Atmospheric Environment* 41(18): 3862-3876.

Graham, D. I. and P.W. James. 1996. Turbulent dispersion of particles using eddy interaction models. *International Journal of Multiphase Flow* 22(1):157-175.

Haghighat, F., Z. Jiang, J.C. Y. Wang, and F. Allard. 1992. Air movement in buildings using computational fluid dynamics. *Transactions of ASME* 114:84-92.

Hinds, W. C. 1999. *Aerosol technology: Properties, behavior, and measurement of airborne particles*. 2nd ed. New York, N.Y.: John Wiley & Sons.

Holmberg, S and Y. Li. 1998. Modeling of the indoor environment – particle dispersion and deposition. *Indoor Air* 8:113-122.

Jones, P.J. and G.E. Whittle. 1992. Computational fluid dynamics for building airflow for building air flow predictions – current status and capabilities. *Building and Environment* 27(30):321-338.

Kleinstreuer, C. 2003. *Two-phase flows: Theory and applications.* New York, N.Y.: Taylor and Francis.

Lai, A.C.K. 2004. Particle deposition indoors: A review. *Indoor Air* 12(4): 211-224.

Liddament, M. W. 1991. A review of building air flow simulation. Technical Note AIVC33. Air Infiltration and Ventilation Center. Coventry, Great Britain: University of Warwick Science Park.

Predicala, B. 2003. Characterization and modeling of concentrations and emissions of particulate matter in swine buildings. PhD dissertation. Manhattan, KS: Kansas State University.

Riddle, A., D. Carruthers, A. Sharpe, C. McHugh, and J. Stocker. 2004. Comparisons between FLUENT and ADMS for atmospheric dispersion modeling. *Atmospheric Environment* 38:1029-1038.

Zhang, N. 2005. Motion and distribution of micro-sized solid particles in turbulent gas flow. PhD dissertation. Manhattan, KS: Kansas State University.

Zhang, N. and Z.C. Zheng. 2007. A collision model for a large number of particles with significantly different sizes. *Journal of Physics D: Applied Physics* 40:2603-2612.

Zhang, Z. and Q. Chen. 2007. Comparison of the Eulerian and Lagrangian methods for predicting particle transport in enclosed spaces. *Atmospheric Environment* 41(25):5236-5248.

7. Conclusions and Recommendations

7.1 Conclusions

The aerodynamic, infrared (IR) extinction, and charging properties of nanostructured metal oxide particles were investigated in this research. The following conclusions were drawn:

1. The two particles (i.e., NanoActive® MgO and MgO plus) differed significantly in particle size distribution and concentration. For example, NanoActive® MgO had a geometric mean diameter (GMD) of 3.12 μm (s.d. = 1.30 μm) while the NanoActive® MgO plus had a mean GMD of 11.1 μm (s.d. = 0.49 μm).
2. Brass flakes had the greatest overall mean volume extinction coefficient, σ_v (1.64 m^2/cc, s.d.=0.39), followed by $NaHCO_3$ (0.93 m^2/cc, s.d.=0.12) and ISO fine test dust (0.91 m^2/cc, s.d.=0.03). Based on the σ_v values, ISO fine test dust and $NaHCO_3$ appeared to be the most promising alternative to brass flakes.
3. Tribocharging using Teflon® was able to charge the particles positively; however, the resulting charge was generally small compared with their Gaussian limits. NanoActive® TiO_2 gained the highest net charge-to-mass ratio (1.21 mC/kg, s.d.=0.07) followed by NanoActive® MgO (0.81 mC/kg, s.d.=0.12), and ISO fine test dust (0.66 mC/kg, s.d.= 0.13).
4. Comparison of predicted and measured mass concentrations showed good agreement for hollow glass spheres, but not for NanoActive® MgO plus. Comparison of predicted and measured number concentrations showed large discrepancies for both particles.

7.2 Suggestions for Further Research

The following are recommended for future studies:

1. Investigate the effect of manipulating the size and/or morphology of ISO fine test dust and $NaHCO_3$ to enhance their IR extinction performance;
2. Measure the extinction properties of the materials using field tests.
3. Predict the extinction properties of the materials.
4. Increase or optimize the contact area between particles and tribocharger surface to increase the charge through triboelectrification.
5. Employ a more intensive simulation using user-defined functions (UDF), different modeling approach (i.e., Eulerian-Eulerian), collision model and different turbulence models (i.e., realizable k-ε) for nano-agglomerates.

Appendix A - Photos of instruments and experimental set-ups

Figure A.1. The Aerodynamic Particle Sizer® (APS) spectrometer (Model 3321, TSI Inc., Shoreview, MN) with a dilution unit (Model 3302A, TSI, Inc., Shoreview, MN), for measuring the equivalent aerodynamic diameter of particles from 0.5 µm to 20 µm.

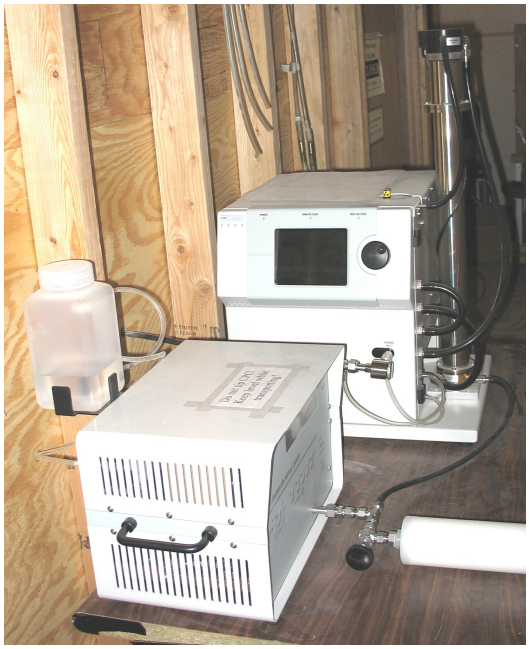

Figure A.2. The Scanning Mobility Particle Sizer® (SMPS) spectrometer (Model 3936, TSI Inc., Shoreview, MN) for measuring the equivalent mobility diameter of particles from ~ 10 nm to 1000 nm.

Figure A.3 The Tapered Element Oscillating Microbalance (TEOM®) (Model 1400a, Thermo-Fisher Scientific, Inc., Waltham, MA), for measuring the mass concentration of particles.

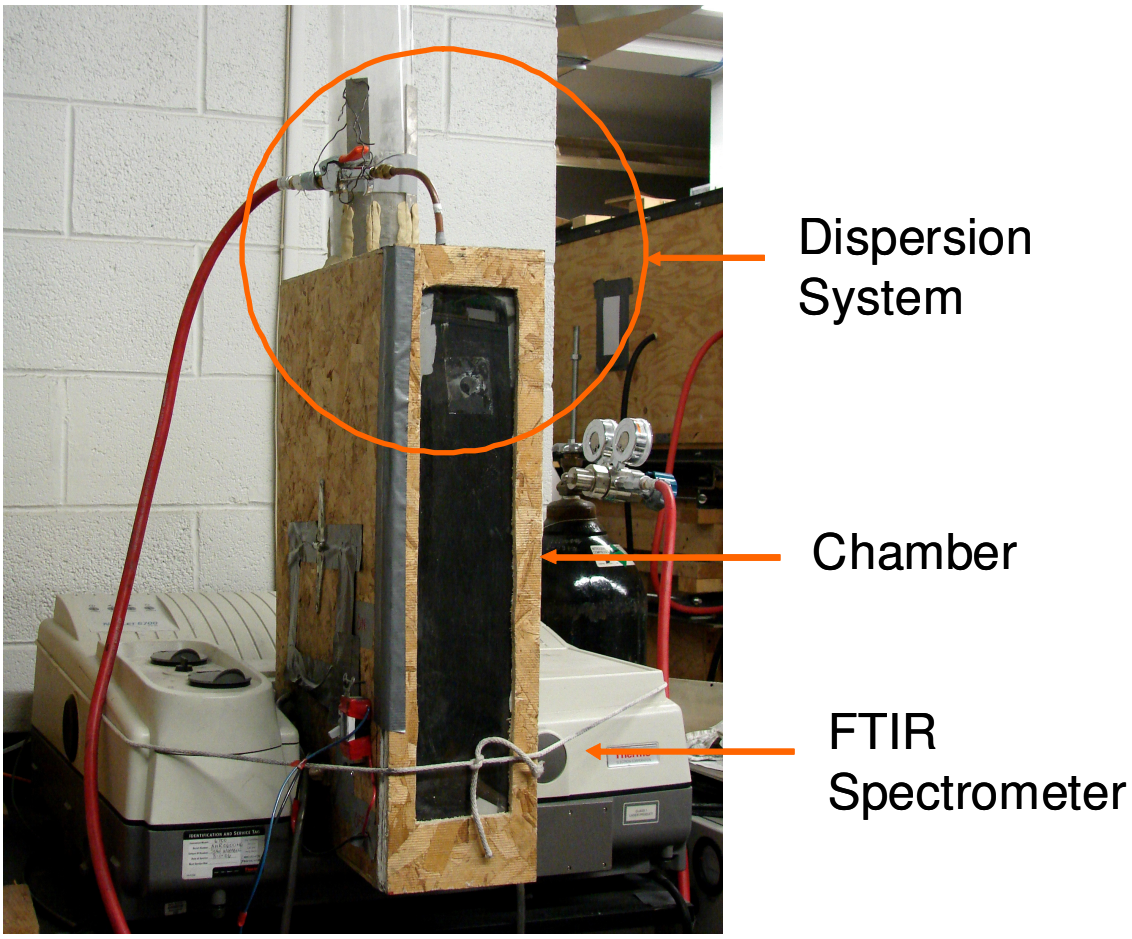

Figure A.4. Experimental set-up for measuring the extinction coefficient of particles.

Figure A.5. The powder disperser used to disperse particles in the chamber.

(a)

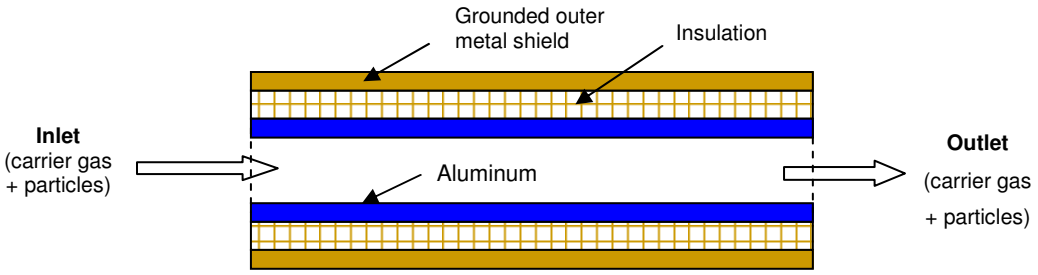

(b)

Figure A.6. A faraday-cage device for determining the charge of deployed particles. The device consists of two concentric metal cylinders. The inner cylinder, which is insulated from the outer cylinder, is electrically connected to the electrometer input. The outer cylinder is connected to ground and serves to shield the inner cylinder from external fields. The device is placed directly in front of the particle deployment location, allowing deployed particles to pass through the inner cylinder.

Figure A.7. The Keithley 6514 Electrometer for measuring electrostatic charge.

Appendix B - Calibration of the dynamic Faraday cup sampler

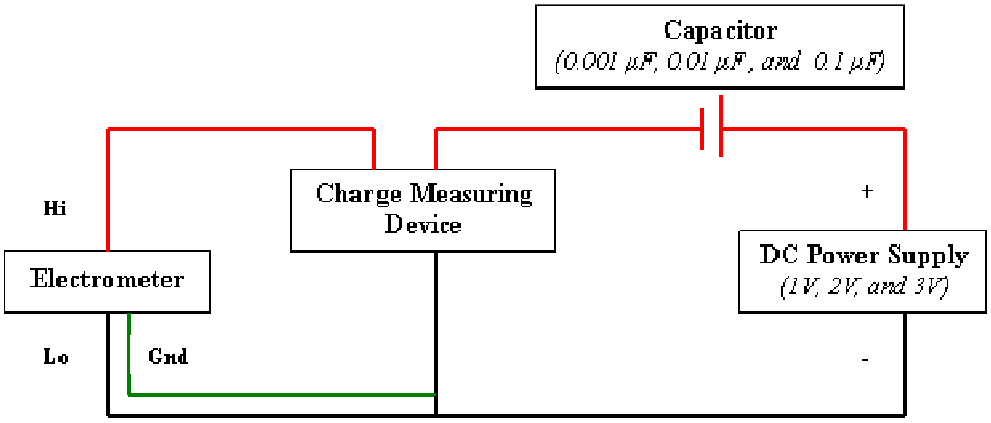

Figure B.1. Schematic diagram of the circuit for calibrating the Faraday cup sampler.

Table B.1. Calibration data for the Faraday cup sampler.

Voltage, V	Capacitor, μF	Calculated charge, nC	Measured charge (Faraday cage sampler), nC
1	0.001	1	1
	0.01	10	10.3
	0.1	100	101.3
2	0.001	2	2.1
	0.01	20	20.8
	0.1	200	200.9
3	0.001	3	3.1
	0.01	30	31.1
	0.1	300	306.2

Appendix C - Experimental data

Data for Chapter 3

Table C.1. Normalized particle number concentrations of NanoActive® MgO (11 g, 80 psig) measured with SMPS.

Diameter, nm	dCn/dlogdp, #/cm^3		
	R1	R2	R3
45.1	18037.9	665.2	3992.0
48.3	14887.9	0.0	3833.9
51.7	7464.9	0.0	1716.2
55.2	5979.1	531.3	3785.9
59.1	2028.7	489.5	1060.4
63.1	1376.0	2037.0	2681.2
67.4	892.6	3231.7	2052.4
72.0	1178.4	1695.1	3448.7
76.8	1054.9	2432.0	4284.2
82.0	2058.7	4578.4	3343.4
87.5	4306.3	5383.0	7581.5
93.3	2694.5	7064.3	6589.5
99.5	2942.9	10969.4	12004.7
106.0	4025.6	17757.3	21821.9
113.0	5503.4	17546.1	21730.5
120.3	4836.0	23525.1	36468.0
128.1	5708.6	25631.0	25833.9
136.4	7329.0	33421.2	32411.2
145.2	8870.4	35097.8	21018.3
154.5	6758.3	49017.0	26954.1
164.4	17058.6	66569.0	22618.7
175.0	23494.7	100405.0	29957.9
186.1	28338.5	100680.0	54971.4
197.9	35818.0	112140.0	98721.7
210.6	64308.3	133606.0	133109.0
224.1	67192.4	130121.0	176712.0
238.5	69890.0	127171.0	202291.0
253.8	68011.0	138882.0	235054.0
270.2	67028.5	170492.0	231121.0
287.6	84006.1	221184.0	273332.0
306.2	76595.2	207088.0	300997.0
326.3	82426.9	280827.0	324278.0
347.7	93070.7	364543.0	368861.0
370.8	117061.0	430418.0	415141.0
395.5	158436.0	404089.0	399084.0
422.0	167713.0	461699.0	446445.0
450.4	217058.0	549697.0	503263.0
481.0	217558.0	583608.0	505194.0

Table C.1. Cont…

Diameter, nm	dCn/dlogdp, #/cm^3		
	R1	R2	R3
513.5	250561.0	555151.0	496416.0
548.6	243085.0	537187.0	543296.0
586.6	263152.0	547527.0	555546.0
627.4	266805.0	676772.0	646838.0
671.3	271495.0	643051.0	660924.0
718.5	216391.0	599367.0	648128.0
769.2	231052.0	593678.0	669137.0
823.8	252108.0	680464.0	738298.0
882.4	240366.0	743057.0	757545.0
945.5	226283.0	675423.0	668811.0
1013.2	219455.0	582882.0	624563.0
1086.1	188258.0	549689.0	556931.0
1164.3	184631.0	472115.0	513593.0
1248.5	161468.0	435534.0	435283.0
1338.8	143647.0	379923.0	384760.0

Table C.2. Normalized particle number concentrations of NanoActive® MgO (11 g, 80 psig) measured with APS.

Diameter, nm	dCn/dlogdp, #/cm^3		
	R1	R2	R3
542.0	140334.0	101319.0	127096.0
583.0	187447.0	137247.0	169139.0
626.0	231655.0	170783.0	204067.0
673.0	272162.0	201258.0	234390.0
723.0	277348.0	205394.0	230008.0
777.0	254779.0	189945.0	205655.0
835.0	209670.0	157161.0	164844.0
898.0	167374.0	125448.0	128850.0
965.0	125301.0	92589.4	93772.0
1037.0	96947.0	70187.7	70731.0
1114.0	72119.4	52823.8	51992.8
1197.0	55056.7	39514.9	38873.7
1286.0	43590.8	30463.2	29994.6
1382.0	33716.5	23198.1	22800.4
1486.0	27040.4	18108.2	18004.4
1596.0	21795.3	14274.8	14686.0
1715.0	17028.6	11239.7	11810.3
1843.0	13817.6	9105.0	9658.5
1981.0	11291.9	7390.2	7739.3
2129.0	8892.8	5747.0	6264.3
2288.0	7005.3	4641.2	5152.6
2458.0	5450.9	3773.8	4310.8
2642.0	4403.1	2957.5	3519.5
2839.0	3371.0	2460.0	2845.5
3051.0	2792.8	1955.7	2471.4
3278.0	2362.4	1542.7	1952.0
3523.0	2046.1	1216.7	1631.7
3786.0	1664.3	984.9	1367.6
4068.0	1361.8	877.8	1144.2
4371.0	1125.8	696.8	921.6
4698.0	989.6	587.5	772.4
5048.0	829.0	466.7	645.2
5425.0	704.5	349.3	525.7
5829.0	585.9	275.5	449.9
6264.0	494.0	229.6	374.6
6732.0	392.1	186.7	308.7
7234.0	367.4	140.4	275.0
7774.0	343.8	112.0	211.9

Table C.2. Cont….

Diameter, nm	dCn/dlogdp, #/cm^3		
	R1	R2	R3
8354.0	260.9	90.3	183.8
8977.0	197.2	73.5	176.7
9647.0	137.1	70.3	132.5
10370.0	133.5	48.7	101.8
11140.0	119.4	24.1	105.5
11970.0	101.4	17.6	58.5
12860.0	89.7	10.9	63.1
13820.0	56.5	8.3	60.1
14860.0	62.8	5.5	28.6
15960.0	12.8	0.0	17.0

Table C.3. Normalized particle number concentrations of NanoActive® MgO (11 g, 80 psig) - merged SMPS and APS data.

Diameter, nm	dCn/dlogdp, #/cm^3		
	R1	R2	R3
44.6	18016.1	665.2	3990.9
62.5	14806.7	--	3804.6
66.7	7441.2	--	1759.1
71.2	5841.2	531.0	3707.4
75.9	2006.1	512.9	1119.6
81.0	1355.9	2064.0	2646.2
86.3	906.4	3174.8	2128.9
91.9	1171.5	1715.7	3494.9
97.9	1117.4	2546.7	4204.4
104.2	2214.2	4573.3	3657.7
110.9	4183.7	5465.9	7455.6
118.0	2715.1	7289.0	7089.3
125.5	3040.3	11587.6	12887.3
133.4	4168.7	17565.8	21813.1
141.6	5434.2	18029.9	23259.3
150.4	4932.6	23715.8	35291.3
159.8	5768.0	26387.5	26607.2
169.7	7489.6	33923.5	30993.0
180.1	8755.3	36349.0	21798.3
191.2	7866.4	51131.1	26354.5
203.0	17882.1	71724.7	23684.7
215.2	24167.7	99614.2	33763.7
228.5	29454.9	102301.4	60558.1
242.6	41111.9	116476.1	105801.7
257.5	64163.7	131856.7	140647.6
273.5	67965.2	129578.1	181311.9
290.4	69807.7	129115.9	208408.7
308.5	67826.2	144459.5	231293.6
327.5	69988.9	179846.5	239292.2
348.2	82100.9	220654.8	279115.1
370.3	77638.8	219671.3	306245.8
394.0	85882.6	298331.3	334405.6
419.4	97143.6	378937.0	379874.8
446.6	126447.2	424754.3	412131.7
475.8	160751.0	417768.3	410831.6
507.2	179740.5	483271.5	460401.0
540.5	263691.5	390514.7	392420.7
575.9	318282.1	437591.7	437704.2
613.3	392763.4	471991.3	494946.2
654.2	456292.0	514748.0	567948.4
698.1	498712.2	556337.8	604565.6
745.3	440967.1	563277.4	585455.4
795.9	329620.1	465447.5	492470.5
850.3	248578.9	403571.0	437611.7

Table C.3. Cont…

Diameter, nm	dCn/dlogdp, #/cm^3		
	R1	R2	R3
908.7	218922.2	378810.1	419024.4
971.5	203070.0	401850.9	430083.3
1038.9	180365.1	413599.7	420584.6
1111.3	159418.6	367795.6	366836.9
1189.0	144680.5	316760.9	336221.0
1272.4	122269.1	293477.8	297527.8
1361.9	114394.1	251263.1	271083.3
1458.1	98586.1	229754.3	229220.6
1561.3	85996.1	199748.8	202210.5
1674.2	24267.8	15726.8	15902.1
1797.9	19391.3	12677.3	12381.8
1931.1	15323.5	10141.1	10735.3
2072.4	12607.8	8286.7	8815.8
2226.8	9937.2	6473.2	7139.6
2392.9	8383.5	5425.2	5882.5
2571.6	6670.4	4386.4	4876.1
2763.9	5304.0	3636.4	4124.1
2970.9	4299.4	2921.4	3480.1
3193.7	3401.5	2399.1	2823.5
3433.4	2788.5	1991.5	2441.5
3691.4	2373.2	1600.2	2021.9
3969.1	2069.6	1280.6	1612.3
4268.0	1766.0	1034.3	1428.6
4589.7	1463.2	911.4	1218.2
4935.9	1201.4	762.8	1006.8
5308.5	1059.8	639.8	841.1
5709.6	930.1	552.6	734.1
6141.3	794.8	421.2	604.5
6605.9	692.5	339.6	518.0
7106.0	557.1	255.0	434.3
7644.3	500.4	236.4	371.8
8223.7	380.6	179.5	310.0
8847.3	396.2	142.6	286.9
9518.5	354.2	114.2	211.6
10240.9	269.3	93.8	195.9
11018.5	210.1	78.5	191.8
11855.5	145.9	77.6	142.7
12756.5	152.9	53.6	114.2
13726.2	134.5	26.6	119.2
14769.9	116.2	20.2	67.7
15893.4	101.8	12.5	71.6
17102.6	69.1	10.0	72.5
18404.2	78.9	7.1	36.9
19795.8	18.4	--	23.2

Table C.4. Normalized particle number concentrations of NanoActive® MgO plus (13 g, 80 psig) measured with SMPS.

Diameter, nm	dCn/dlogdp, #/cm^3		
	R1	R2	R3
45.1	9500.9	0.0	26375.3
48.3	4405.9	0.0	13678.5
51.7	4202.8	582.5	14427.6
55.2	4356.1	545.5	11141.7
59.1	1561.5	0.0	10596.2
63.1	475.3	497.2	4782.8
67.4	2788.3	0.0	1434.6
72.0	430.0	0.0	3527.2
76.8	1259.4	0.0	7005.7
82.0	0.0	0.0	4148.9
87.5	307.5	358.7	5235.2
93.3	279.6	0.0	11189.6
99.5	142.4	0.0	10100.1
106.0	1255.5	0.0	13054.0
113.0	743.4	224.5	17982.6
120.3	2138.1	654.4	20979.1
128.1	2612.8	440.7	20991.8
136.4	6635.3	762.7	25887.9
145.2	3709.0	1889.6	28786.6
154.5	5737.7	1686.5	42807.3
164.4	5451.2	3087.0	41997.4
175.0	7963.7	4281.0	61902.1
186.1	10357.5	7018.7	67042.5
197.9	9406.1	10704.3	72601.4
210.6	15112.6	10541.2	86607.7
224.1	21996.7	11887.6	91767.7
238.5	10513.0	17095.9	99358.9
253.8	14804.3	18643.1	107800.0
270.2	16900.1	15683.7	100640.0
287.6	21702.3	13116.3	99595.3
306.2	19437.7	16383.3	97607.9
326.3	14102.7	18813.1	102432.0
347.7	19418.6	20395.9	105447.0
370.8	15936.1	19679.3	103105.0
395.5	14302.5	16632.3	98126.7
422.0	13691.1	15087.7	94877.2
450.4	13471.3	17141.3	84407.2
481.0	15915.0	13700.2	91951.1

Table C.4. Cont…

Diameter, nm	dCn/dlogdp, #/cm^3		
	R1	R2	R3
513.5	14449.6	14844.4	81875.6
548.6	9438.9	13543.8	70035.1
586.6	13327.3	18164.1	80015.8
627.4	14302.9	14591.9	77971.4
671.3	11589.3	13620.0	69157.8
718.5	12891.2	10195.3	75028.6
769.2	10814.5	11174.8	59356.7
823.8	12791.7	9109.7	65491.1
882.4	13650.2	14612.6	71338.5
945.5	15457.9	10239.2	58386.4
1013.2	9419.3	12151.9	63978.1
1086.1	9190.5	13849.0	55145.6
1164.3	10001.3	12201.5	43235.8
1248.5	8182.7	10511.7	34790.6
1338.8	9383.0	6130.1	35762.2

Table C.5. Normalized particle number concentrations of NanoActive® MgO plus (13 g, 80 psig) measured with APS.

Diameter, nm	dCn/dlogdp, #/cm^3		
	R1	R2	R3
542.0	6534.2	6514.0	11707.6
583.0	8074.0	8180.3	15332.2
626.0	9464.1	9889.2	19247.7
673.0	11026.1	11572.9	23408.8
723.0	12186.9	12442.6	25998.7
777.0	12611.1	12902.2	27592.8
835.0	12359.5	12530.8	27726.2
898.0	12473.2	12370.5	27467.1
965.0	11919.0	11862.3	25715.3
1037.0	11658.5	11260.9	24819.0
1114.0	10957.9	10579.8	23081.8
1197.0	10144.8	9852.9	21836.5
1286.0	8788.7	9142.8	20081.7
1382.0	7908.2	7797.4	17496.6
1486.0	6680.4	6928.0	15493.6
1596.0	5748.9	6039.3	13191.3
1715.0	4888.2	5218.7	11329.3
1843.0	4187.3	4596.6	9555.9
1981.0	3461.7	3949.0	8465.7
2129.0	3013.6	3301.5	7240.5
2288.0	2486.4	2702.1	5842.8
2458.0	1887.3	2084.7	4615.3
2642.0	1534.5	1606.9	3590.1
2839.0	1221.9	1220.7	2924.4
3051.0	969.9	956.7	2265.3
3278.0	781.5	761.1	1749.8
3523.0	632.9	601.0	1371.9
3786.0	584.4	553.2	1075.1
4068.0	541.7	492.4	951.6
4371.0	537.0	428.9	833.3
4698.0	550.7	437.2	781.6
5048.0	496.6	443.2	726.8
5425.0	529.5	412.4	725.6
5829.0	529.5	437.0	749.3
6264.0	513.9	426.7	746.6
6732.0	648.9	536.0	808.7
7234.0	612.2	589.2	825.8
7774.0	777.1	619.0	899.8

Table C.5. Cont…

Diameter, nm	dCn/dlogdp, #/cm^3		
	R1	R2	R3
8354.0	678.1	674.6	994.0
8977.0	768.4	736.0	1170.9
9647.0	749.8	755.6	1182.3
10370.0	699.2	578.2	1041.4
11140.0	553.1	477.5	955.2
11970.0	364.6	360.9	768.9
12860.0	369.5	240.0	557.3
13820.0	300.4	189.2	399.8
14860.0	175.8	132.9	311.7
15960.0	168.0	99.7	196.1
17150.0	68.4	67.8	86.6

Table C.6. Normalized number concentrations of NanoActive® MgO plus (13 g, 80 psig) - merged SMPS and APS data.

Diameter, nm	dCn/dlogdp, #/cm^3		
	R1	R2	R3
45.1	9500.9	--	26375.3
48.3	4405.9	--	13749.7
51.6	4202.8	582.5	14453.9
55.2	4356.1	545.5	11210.2
59.0	1561.5	--	10560.4
63.1	475.3	497.2	4972.2
67.4	2788.3	--	1520.8
72.0	430.0	--	3435.1
76.7	1259.4	--	6859.6
81.9	--	--	4268.9
87.4	307.5	358.7	5163.3
93.2	279.0	--	10857.5
99.3	145.3	--	10090.4
105.8	1230.2	--	12807.0
112.7	758.8	224.5	17710.4
120.0	2085.4	650.6	20529.0
127.6	2591.2	444.4	20988.8
135.8	6422.5	754.2	25376.4
144.5	3852.7	1833.6	28738.8
153.8	5582.0	1711.9	40933.3
163.6	5476.8	2982.7	42115.4
174.0	7736.7	4195.2	59427.3
184.9	10127.0	6800.1	66414.2
196.6	9513.7	10482.5	71901.1
209.1	14483.3	10462.9	84707.4
222.4	21306.5	11756.6	91099.6
236.6	11901.2	16641.2	98312.7
251.7	14213.1	18466.6	106598.4
267.8	16629.6	15982.9	101883.4
285.0	21038.3	13518.5	99866.1
303.2	19796.7	15907.1	98036.2
322.9	14932.4	18476.0	101685.0
344.0	18588.8	20174.3	104991.6
366.6	16541.3	19819.9	103600.2
390.8	14597.5	17171.8	99109.9
416.7	13803.7	15372.9	95532.4
444.5	13508.6	16753.2	86493.2
474.4	15372.7	14374.9	90403.9
506.5	14786.2	14597.7	83969.6
540.9	13956.1	15454.1	51088.5
579.0	16785.7	19157.3	58286.6
619.9	17388.9	18118.7	58936.5
663.9	13990.7	15245.2	51593.1
711.3	13175.0	12517.9	51583.0

Table C.6. Cont…

Diameter, nm	dCn/dlogdp, #/cm^3		
	R1	R2	R3
762.3	12061.3	12173.0	44635.9
817.2	12493.6	11030.2	45954.8
876.3	12726.6	13050.4	48675.1
939.9	13447.0	11111.4	42635.5
1008.3	10617.3	11635.0	44070.1
1082.0	10073.7	12202.9	39521.9
1161.2	10203.7	11173.1	32911.1
1246.4	9029.5	10045.8	27983.4
1338.1	9072.8	7526.7	27629.3
1437.1	7845.6	7930.2	17612.0
1543.9	6910.9	6977.0	15656.1
1657.3	5902.1	6151.3	13609.8
1781.2	5095.8	5383.7	11782.0
1914.5	4378.0	4704.5	10013.3
2057.9	3685.5	4122.1	8638.4
2212.3	3146.3	3547.8	7697.7
2378.4	2762.0	3006.5	6535.4
2557.1	2221.0	2433.7	5310.2
2749.5	1723.6	1892.6	4172.1
2956.6	1416.1	1464.4	3302.8
3179.4	1114.0	1089.5	2694.6
3419.3	912.9	923.1	2098.2
3677.4	725.6	691.4	1635.5
3955.2	600.2	586.0	1293.0
4254.2	564.2	535.4	1036.6
4576.0	522.2	475.5	918.0
4922.3	518.1	416.9	813.3
5295.1	543.7	426.3	768.9
5696.3	500.8	444.5	730.8
6128.2	529.3	418.5	732.6
6593.0	537.8	435.6	752.4
7093.3	528.8	441.6	757.1
7631.7	634.6	522.5	818.1
8211.3	646.5	602.0	853.5
8835.1	775.9	640.4	921.2
9506.5	730.5	694.1	1014.0
10229.2	794.8	762.9	1198.1
11007.0	816.0	825.2	1288.0
11844.2	782.4	679.8	1171.2
12745.3	672.0	557.9	1091.8
13715.3	427.4	443.3	923.2
14759.2	416.7	286.3	678.3
15882.8	382.4	232.1	478.3
17092.3	201.7	167.8	395.9
18394.0	230.0	121.8	269.4
19795.2	114.6	111.0	143.1

Table C.7. Geometric mean diameters of NanoActive® MgO and NanoActive® MgO plus based on the SMPS and APS data.

Geometric mean diameter, nm						
Time, min	NanoActive® MgO Plus (13 g, 80 psig)					
	SMPS			APS		
	R1	R2	R3	R1	R2	R3
2	895	917	870	11598	11034	11255
6	880	870	873	9356	9822	7898
10	865	891	887	7090	7198	5285
20	875	929	875	3994	4233	3786
30	940	900	897	2824	3410	2816
60	913	866	910	2196	2326	2029
Time, min	NanoActive® MgO (11 g, 80 psig)					
	SMPS			APS		
	R1	R2	R3	R1	R2	R3
2	1082	1089	1091	3057	4833	4677
6	1104	1124	1118	2233	3057	2692
10	1114	1136	1153	1892	2366	1911
20	1140	1150	1131	1582	2119	1576
30	1128	1148	1144	1411	1720	1391
60	1170	1161	1183	1238	1536	1187

Table C.8. Number concentrations of NanoActive® MgO plus and NanoActive® MgO measured with SMPS and APS.

Number concentration, #/cm^3						
Time, min	NanoActive® MgO Plus (13 g, 80 psig)					
	SMPS			APS		
	R1	R2	R3	R1	R2	R3
2	14000	13600	87700	8470	7990	16800
6	12500	12500	73100	9370	8720	13600
10	7880	7700	57200	8220	7510	11400
20	4170	6070	43200	7040	6220	9490
30	2830	5690	36500	6150	5500	8180
60	1480	3690	22900	4480	3770	5200
Time, min	NanoActive® MgO (11 g, 80 psig)					
	SMPS			APS		
	R1	R2	R3	R1	R2	R3
2	156000	410000	421000	110000	110000	134000
6	109000	236000	266000	105000	93700	107000
10	60500	208000	155000	100000	85600	102000
20	38400	143000	105000	87400	78500	91700
30	23700	124000	88700	77900	70200	90400
60	7960	27700	32400	59600	54300	69500

Table C.9. Mass concentrations of NanoActive® MgO plus and NanoActive® MgO measured with SMPS and APS.

Mass concentration, mg/m^3						
Time, min	NA MgO Plus (13 g, 80 psig)					
	SMPS			APS		
	R1	R2	R3	R1	R2	R3
2	1.1	1.2	5.4	85.7	124.0	137.0
6	0.9	0.8	4.8	67.7	80.0	68.2
10	0.5	0.5	4.0	29.0	26.6	24.7
20	0.3	0.5	3.0	11.1	10.1	10.7
30	0.3	0.4	2.8	6.6	6.8	8.0
60	0.2	0.3	1.9	3.5	3.0	3.5
Time, min	NA MgO (11 g, 80 psig)					
	SMPS			APS		
	R1	R2	R3	R1	R2	R3
2	26.1	70.6	73.0	28.9	33.4	37.5
6	19.9	49.6	48.4	23.8	38.7	27.5
10	12.1	46.5	32.3	20.8	26.3	20.3
20	8.4	35.3	22.3	16.4	20.9	15.9
30	5.5	29.0	20.7	13.6	16.3	14.5
60	2.2	7.1	9.3	9.1	11.1	9.7

Table C.10. Mass concentrations of NanoActive® MgO plus and NanoActive® MgO measured with TEOM.

Time, min	NanoActive® MgO (11 g, 80 psig)			NanoActive® MgO plus (13 g, 80 psig)		(40 g, 80 psig)			(37 g, 40 psig)	
	R1	R2	R3	R1	R2	R1	R2	R3	R1	R2
0	59.9	0.1	0.4	0.2	0.0	0.0	0.4	6.0	3.3	0.2
1	363.2	266.5	298.3	518.8	342.3	487.4	830.2	624.9	310.2	644.1
2	234.9	202.0	237.6	283.2	316.0	260.5	539.6	549.0	330.9	476.4
3	204.0	185.6	210.3	186.9	244.2	264.0	453.5	472.3	251.9	335.4
4	193.4	158.6	206.5	168.2	161.4	257.0	309.5	425.0	204.3	230.6
5	196.8	157.8	182.8	120.9	158.6	215.2	301.7	347.2	158.9	167.2
6	185.5	146.6	172.0	100.9	128.3	185.6	253.2	301.9	153.6	147.4
7	156.6	138.4	149.8	87.7	115.6	157.7	200.3	266.8	125.0	131.8
8	152.4	140.1	143.1	81.9	90.5	142.1	174.7	224.0	111.5	116.7
9	145.8	135.3	137.2	69.3	79.2	122.5	157.7	194.9	96.8	107.5
10	141.7	128.7	128.1	63.4	67.9	110.9	138.0	182.7	86.4	98.2
11	131.2	116.6	118.6	58.6	60.4	95.0	123.7	165.4	73.7	81.1
12	120.4	111.7	120.0	57.1	53.3	92.2	118.9	151.3	69.4	79.3
13	120.3	108.7	115.2	51.8	48.7	83.0	108.3	134.5	62.5	69.5
14	115.0	101.8	111.8	47.6	46.0	72.3	97.6	124.6	56.8	66.3
15	110.7	99.5	107.6	45.6	43.1	71.8	91.0	118.9	52.0	65.6
16	107.8	94.3	98.7	43.9	39.6	68.0	86.0	109.5	50.8	60.7
17	98.2	89.9	97.7	41.4	36.6	61.3	80.2	100.5	45.5	55.2
18	99.1	89.6	95.9	39.3	36.2	57.4	74.7	99.0	44.8	51.6
19	96.7	89.5	96.2	36.2	35.0	54.9	70.3	92.9	42.2	51.0
20	95.1	85.5	90.4	35.4	33.8	52.7	64.6	88.1	40.3	48.0
21	94.2	81.7	89.7	34.5	31.9	50.4	62.8	85.9	38.3	45.8
22	91.6	81.1	88.2	33.3	29.7	48.4	60.8	80.6	36.0	43.0
23	91.6	--	83.0	30.7	29.5	46.4	58.0	76.3	33.4	42.0
24	91.6	--	84.3	30.2	28.7	45.2	55.1	73.5	33.1	41.0
25	91.6	--	82.6	29.7	28.2	42.9	52.2	70.6	31.5	37.2
26	91.6	--	80.1	28.0	26.6	40.0	51.4	66.8	29.9	36.3
27	91.6	--	78.7	27.9	25.0	39.7	48.8	64.7	29.3	34.8
28	91.6	--	75.2	27.0	25.1	38.3	48.1	62.8	27.0	33.5
29	91.6	--	74.5	26.4	23.7	37.1	46.3	59.4	26.8	32.6
30	91.6	--	70.4	25.1	23.7	36.8	45.3	57.2	26.4	31.9

Data for Chapter 4

Table C.11. Mass extinction coefficients of the particles.

Particle	Rep	Mass extinction coefficent, m^2/g		
		3-5 µm	8-12 µm	Overall
NanoActive® MgO plus	1	0.49	0.15	0.23
	2	0.46	0.14	0.22
	3	0.55	0.15	0.25
NanoActive® MgO	1	0.69	0.12	0.26
	2	0.64	0.10	0.23
	3	0.67	0.10	0.23
NanoActive® TiO_2	1	1.32	0.28	0.52
	2	0.86	0.18	0.34
	3	1.12	0.23	0.44
$NaHCO_3$	1	0.82	0.70	0.72
	2	0.65	0.55	0.57
	3	0.81	0.68	0.71
ISO fine test dust	1	0.73	0.78	0.77
	2	0.71	0.74	0.73
	3	0.71	0.72	0.72
Brass flakes	1	1.29	1.46	1.42
	2	1.19	1.33	1.30
	3	1.83	2.06	2.00
Graphite flakes	1	2.57	2.84	2.78
	2	3.32	3.55	3.50
	3	3.21	3.55	3.44
Carbon black	1	2.24	2.15	2.17
	2	1.74	1.28	1.39
	3	1.70	1.55	1.60
MgO nanorods	1	0.69	0.79	0.77
	2	0.86	0.35	0.47
TiO_2 nanorods	1	0.92	0.17	0.35
	2	0.92	0.25	0.41
	3	1.16	0.26	0.48

Table C.12. Masses dispersed and mass concentrations of particles measured using filter samplers.

Particle	Rep	Mass dispersed, g	Mass concentration, g/m^3
NanoActive® MgO plus	1	3.05	1.40
	2	3.04	1.93
	3	3.03	1.76
NanoActive® MgO	1	2.66	1.10
	2	2.35	0.96
	3	2.16	0.84
NanoActive® TiO_2	1	2.03	1.14
	2	2.77	1.91
	3	2.71	1.76
$NaHCO_3$	1	3.06	1.39
	2	2.98	1.98
	3	2.72	1.40
ISO fine test dust	1	2.53	0.72
	2	2.53	0.71
	3	2.45	0.86
Brass flakes	1	3.01	2.70
	2	3.01	2.83
	3	3.01	2.33
Graphite flakes	1	2.99	2.55
	2	2.96	1.79
	3	3.01	2.12
Carbon black	1	2.91	1.59
	2	2.75	2.48
	3	2.88	2.04
MgO nanorods	1	1.04	0.20
	2	1.34	0.81
TiO_2 nanorods	1	2.87	2.60
	2	2.78	3.18
	3	2.23	1.93

Table C.13. Volume extinction coefficients of the particles.

Particle	Rep	Volume extinction coefficent, m^2/cc		
		3-5 µm	8-12 µm	Overall
NanoActive® MgO plus	1	0.32	0.10	0.15
	2	0.30	0.09	0.14
	3	0.36	0.10	0.16
NanoActive® MgO	1	0.49	0.09	0.18
	2	0.46	0.07	0.16
	3	0.47	0.07	0.16
NanoActive® TiO_2	1	1.06	0.22	0.42
	2	0.69	0.14	0.27
	3	0.89	0.18	0.35
$NaHCO_3$	1	1.14	0.97	1.01
	2	0.90	0.76	0.80
	3	1.13	0.94	0.99
ISO fine test dust	1	0.89	0.95	0.94
	2	0.86	0.90	0.90
	3	0.86	0.88	0.88
Brass flakes	1	1.35	1.52	1.48
	2	1.25	1.39	1.36
	3	1.91	2.15	2.09
Graphite flakes	1	0.63	0.70	0.69
	2	0.82	0.88	0.86
	3	0.79	0.88	0.85
Carbon black	1	0.49	0.47	0.48
	2	0.38	0.28	0.31
	3	0.37	0.34	0.35
MgO nanorods	1	0.07	0.08	0.08
	2	0.09	0.03	0.05
TiO_2 nanorods	1	0.63	0.12	0.24
	2	0.63	0.17	0.28
	3	0.79	0.18	0.32

Table C.14. Number and mass concentrations, geometric mean diameters (GMD), and geometric standard deviations (GSD) of the particles measured with APS at time 2 min after dispersion.

Particle	Rep	Number concentration, #/cm^3	Mass concentration, mg/m^3	GMD, µm	GSD
NanoActive® MgO plus	1	115000	1240	8.26	1.66
	2	110000	1550	8.59	1.60
	3	146000	1570	8.10	1.70
NanoActive® MgO	1	418000	541	5.38	2.50
	2	399000	330	4.40	2.73
	3	393000	399	4.79	2.59
NanoActive® TiO_2	1	230000	454	4.50	1.84
	2	205000	473	4.46	1.83
	3	254000	990	5.66	1.85
$NaHCO_3$	1	211000	1590	5.96	1.74
	2	231000	1620	5.96	1.77
	3	262000	2120	5.74	1.71
ISO fine test dust	1	157000	381	3.33	1.87
	2	140000	361	3.46	1.87
	3	114000	467	4.40	1.88
Brass flakes	1	53200	107	3.24	1.69
	2	49600	89	2.95	1.62
	3	71400	225	3.51	1.59
Graphite flakes	1	373000	1580	4.01	1.98
	2	103000	370	3.47	1.86
	3	95100	481	4.13	1.91
Carbon black	1	260000	452	6.84	2.06
	2	526000	551	8.27	2.27
	3	276000	560	7.29	2.01
MgO nanorods	1	27300	115	4.74	1.84
	2	84200	180	6.17	1.87
TiO_2 nanorods	1	111000	135	3.91	1.89
	2	51100	338	5.21	1.7

Data for Chapter 5

Table C.15. Charge-to-mass ratios of the particles.

Particle	Rep	Charge-to-mass ratio, mC/kg	
		Background	Teflon® tribocharger
NanoActive® MgO plus	1	0.01	0.22
	2	0.02	0.31
	3	0.03	0.23
NanoActive® MgO	1	0.07	0.76
	2	0.03	0.84
	3	0.05	0.97
NanoActive® TiO_2	1	-0.26	0.86
	2	-0.36	0.89
	3	-0.29	0.96
$NaHCO_3$	1	0.03	0.22
	2	0.02	0.27
	3	0.02	0.23
ISO fine test dust	1	0.15	0.88
	2	0.20	0.93
	3	0.24	0.75
Nylon powder	1	1.43	0.82
	2	1.13	0.72
	3	1.32	0.80

Data for Chapter 6

Table C.16. Mass concentrations of hollow glass spheres (predicted and measured with filter samplers).

Distance from injection point, m	Mass concentration, mg/m^3					
	Predicted (coarse mesh)	Predicted (fine mesh)	Predicted (very fine mesh)	Measured		
				R1	R2	R3
0.6	348	386	290	135	431	172
1.8	136	96	156	79	129	44
3.0	91	45	111	15	10	30

Table C.17. Mass concentrations of NanoActive® MgO plus (predicted and measured with filter samplers).

Distance from injection point, m	Mass concentration, mg/m^3			
	Predicted (coarse mesh)	Measured		
		R1	R2	R3
0.6	216	302	54	103
1.8	135	556	834	124
3.0	37	284	1005	832

Table C.18. Number concentrations of hollow glass spheres (predicted and measured with APS® spectrometer).

Time after dispersion, s	Number concentration, #/cm^3					
	Predicted			Measured		
	(0.4m x 0.4m x 0.4m)	(0.3m x 0.3m x 0.4m)	(0.2 m x 0.2m x 0.4m)	R1	R2	R3
60	199,841	64,175	71,546	16,800	11,000	14,800
120	598,385	289,075	182,117	2,810	2,060	1,900
180	526,839	173,445	234,151	5,870	2,350	2,110
240	331,713	196,571	312,201	2,310	1,870	3,140
300	351,226	115,630	26,017	1,600	2,970	3,370
360	188,621	23,126	52,033	2,470	4,180	2,550
420	331,713	127,193	182,117	3,130	4,850	3,750
480	188,621	46,252	104,067	6,700	4,890	4,700
540	260,167	92,504	130,084	6,620	4,320	4,490
600	240,655	69,378	52,033	6,320	3,850	4,510

Table C.19. Number concentrations of NanoActive® MgO plus (predicted and measured with APS® spectrometer).

Time after dispersion, s	Number concentration, #/cm^3					
	Predicted			Measured		
	(0.4m x 0.4m x 0.4m)	(0.3m x 0.3 m x 0.4m)	(0.2 m x 0.2m x 0.4m)	R1	R2	R3
60	644,576	336,877	190,985	21,200	20,900	25,500
120	531,178	190,985	190,985	7,710	7,630	6,980
180	483,432	159,155	95,493	4,560	7,140	7,930
240	483,432	201,596	167,112	4,580	6,440	8,290
300	346,161	53,052	119,366	4,890	6,910	8,230
360	376,003	159,155	143,239	4,800	6,410	8,320
420	483,432	169,765	143,239	4,640	6,350	7,890
480	358,098	116,713	47,746	4,440	6,300	7,700
540	298,415	137,934	143,239	3,670	6,160	7,610
600	370,034	190,985	119,366	4,030	5,820	7,250